DEVELOPMENT AND VALIDATION OF A 'SURFACE-BASED' GEOMETRICAL ACOUSTIC FORMULATION WITHIN A GALERKIN BOUNDARY ELEMENT FRAMEWORK

BY

AMAL EMTHYAS

SUPERVISED BY

DR. JONATHAN A. HARGREAVES

THIS THESIS IS PRESENTED FOR THE DEGREE OF MASTER OF SCIENCE BY RESEARCH

SCHOOL OF SCIENCE, ENGINEERING AND ENVIRONMENT

UNIVERSITY OF SALFORD

SEPTEMBER 2022

ABSTRACT

As sound propagates within a room, it experiences high-order reflection, diffraction, and scattering. This causes the reflection density to increase over time, such that the sound field becomes diffuse and chaotic. Under these conditions, there is little benefit in running a computationally costly full wave solver – if it is even feasible – so methods based on Geometrical models of acoustic propagation prevail. Raytracing is currently the de-facto method for this late-time, high-frequency regime in room acoustic modelling. It samples the propagating distributions of acoustic intensity by launching a set of rays and individually tracing their trajectories. This is computationally efficient when only specular reflections are present, but accurate inclusion of scattering or diffraction requires 'ray-splitting' to be introduced, causing an exponential increase in computational cost with reflection order, crippling the algorithm. Hence only crude Monte Carlo implantations of these processes are tractable with Raytracing.

An emerging solution for modelling late-reflections is "Surface-Based" Geometrical Acoustics. These formulations map a distribution of rays arriving at a boundary onto a pre-defined 'approximation space' of basis functions spanning position and angle, so the sound field is represented by a vector of boundary coefficients. Re-radiation of subsequent reflections is thus reduced to a matrix multiplication, with the steady-state solvable via a Neumann series. As rays only propagate one reflection order before being collected, the multiple 'child' rays produced that would be produced by scattering or diffraction of a 'parent' ray at the boundary are absorbed into the 'approximation' space at each reflection order. This maintains a fixed number of degrees of freedom and a linear computational cost with reflection order. This thesis presents a Surface-Based Geometrical Acoustic formulation cast in a Galerkin Boundary Element framework.

This thesis presents and implements the formulation in two dimensions and validates it against an Image Source Model for a rectangular room. The Galerkin Boundary Element scheme expediates comparison of different approximation schemes and their effect on convergence and accuracy can be easily studied. Examination of the resulting power distributions on the boundary for early reflections show power being smudged over a range of reflection angles, indicating approximation in the scheme. But this is perceptually appropriate for late-time diffuse fields as individual reflections will no longer be distinguishable, and late time energy decay rates are shown to be correct. Receiver responses for early reflections show very good agreement also, so long as angular resolution is set sufficiently high. The formulation

is shown to converge with the number of angular degrees of freedom as well as smaller element sizes. The results show a high degree of accuracy and identical convergence trends when using continuous orthogonal polynomials, such as Legendre, Chebyshev or Lobatto, as angular basis. In contrast, other functions, such as continuous piecewise-linear, or discontinuous Piecewise-constant, exhibit a significant degree of approximation for higher interpolation orders due to their discontinuous or non-smooth nature. Solutions in Geometrical Acoustics can be discontinuous. The ultimate ambition in formulating the model presented in this thesis is to include diffraction, and solutions when it is included will be continuous. This capability still remains as work for the future, but the choices made in this thesis were informed by that end goal.

ACKNOWLEDGEMENTS

I am greatly indebted to my supervisor, Dr. Jonathan A. Hargreaves who co-developed the formulation presented in this thesis and helped design the code base. His unconditional and continuous support, patience and mentoring have been invaluable during the course of the project.

CONTENTS

List of Abbreviations

Acronym	Expansion/Meaning	Section
FEM	Finite Element Method	1.1
BEM	Boundary Element Method	1.1
GA	Geometrical Acoustics	1.1
PDE	Partial Differential Equation	1.1
ISM	Image Source Method	1.1
SB-GA	“Surface-based” Geometrical Acoustics	1.2
DOF	Degree/Degrees of Freedom	1.2
PWC	Piecewise-Constant	1.2
PWL	Piecewise-Linear	1.2
PWQ	Piecewise-Quadratic	1.2
EBEM	Energy Boundary Element Method	1.3
IS	Image Source/Sources	2.2.1
EI-BEM	Energy-Intensity Boundary Element Method	2.3.1
RARE	Room Acoustic Rendering Equation	2.3.2
ART	Acoustics Radiance Transfer	2.3.2
BIE	Boundary Integral Equation	2.3.2
DEA	Dynamical Energy Analysis	2.3.3
SEA	Statistical Energy Analysis	2.3.3
GQ	Gaussian Quadrature	4.4
GLQ	Gauss-Legendre Quadrature	4.4
FP	Frobenius-Perron	4.4

1 INTRODUCTION

1.1 MOTIVATION

Numerical prediction methods allow implementation, analysis and comparison of different concepts, formulations, and designs without the need to build physical models and/or undertake any measurements. They have had a significant impact on scientific progress and innovation in a wide range of disciplines, including acoustics [1]. The scope of such models within various sub-disciplines in acoustics stretches from refining room acoustics for critical listening and performance spaces to examining transducer and diffuser designs.

In room acoustics, the need to model the entire audible frequency range spanning several octaves with respect to (w.r.t.) dimensions of a typical space imposes the need to operate different classes of prediction models to compute the solution efficiently and accurately in different bandwidths [2]. For modelling low frequencies in room acoustic applications where wave effects dictate important perceptual cues, 'numerically-exact' wave solvers such as Finite Element Method (FEM) or Boundary Element Method (BEM) are most efficient and accurate. But the high-frequency regime remains challenging for these algorithms as their computational workload rises rapidly as a function of frequency [3]. These methods typically discretise space and/or bounding surfaces using elements and model the interactions between them. Geometrical Acoustic (GA) algorithms are most commonly used for modelling high frequencies for room acoustics. Algorithms in this category postulate sound to travel

geometrically in homogenous media, i.e., in straight lines in the form of rays or particles, ignoring all wave effects [4]. This assumption is valid at high frequencies, where the wavelength is short when compared to the room dimensions [1].

The sound field excited by a source in a room transitions to a highly diffuse state soon after early reflections. This is illustrated in Figure 1.1 with the increase in reflection density around the 20 ms mark after sparse early reflections. This process is accelerated if substantial boundary scattering is present. The high reflection density at late-time nullifies the need to model and track individual reflection paths, albeit imposing the necessity to include scattering and diffraction to construct a representative sound field. While wave solvers include effects like diffraction and scattering as a part of how they mathematically solve the underlying Partial Differential Equation (PDE), which describe the acoustic wave propagation in a solution domain, GA methods were inherited from computer graphics and do not inherently model scattering or diffraction within their mechanism; these processes have to independently included with GA where required [5].

Figure 1.1 Impulse response of a room [6]

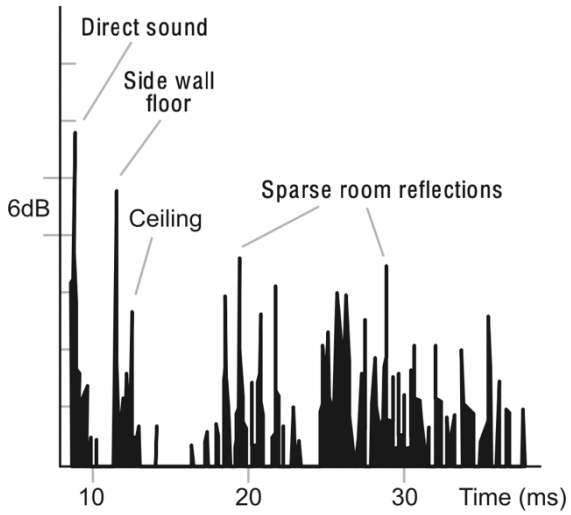

Reflection-path-based GA methods such as classical Raytracing or Image Source Method (ISM) perform best following their basic principle, modelling a single ray incident at a boundary to produce a single reflected ray, without any ray splitting. When additional rays are produced at each reflection order, usually as a consequence of scattering or diffraction, the number of rays grows with reflection order. This leads to exponential cost scaling with reflection order, which is extremely limiting. Hence, only very crude, low-resolution methods of scattering or diffraction are used in conjunction with these GA models. This limits their

ability in maintaining a good balance of accuracy to computational cost in constructing late-time sound fields for room acoustics.

1.2 'SURFACE-BASED' GEOMETRICAL ACOUSTICS

An emerging solution to model late reflections for room acoustics is what Savioja and Svensson [7] term 'Surface-based' Geometrical Acoustics (SB-GA). In contrast to reflection-path-based GA models such as Raytracing, which track individual reflections over many reflection orders, SB-GA algorithms discretise acoustic power flow on a boundary mesh. Similarities with mesh-based wave solvers are evident, particularly with how BEM models low frequencies. SB-GA is thus seen as a hybrid of both BEM and GA approaches, following the GA postulates while computing the solution utilising an element-based mesh.

The core of the SB-GA formulation is the discretisation scheme or 'approximation space'. This is pre-defined and comprises the product of spatial and angular 'basis' or 'shape' functions that are used to interpolate the solution on the boundary. This framework reduces the boundary solution to a vector of coefficients, and modelling reflections between boundaries is simplified to a matrix multiplication. This allows the number degrees of freedom (DOF) of the system to be kept constant – independent of reflection order – and hence maintains a linear computational cost with reflection order. This is true even if scattering is present, so effectively circumvents the issue faced by reflection-path-based GA models in efficiently addressing ray-spitting.

SB-GA algorithms date back to the seventies when Kuttruff proposed Acoustic Radiosity [8]. This models idealised diffuse reflections and ignores their directionality [9]. More sophisticated algorithms under this category, which model and parametrise reflection direction, have since been independently developed by three different research groups. A group at Duke University have presented their model named "Energy-Intensity Boundary Element Method" (EI-BEM) [10] which was further refined in [11]. Another group based in Helsinki have developed an "Acoustic Radiance Transfer" model from the Room Acoustic Rendering Equation [12], and further focused it towards room acoustics in [13]. A third group from Nottingham have developed a Boundary Element version of their "Dynamical Energy Analysis" (DEA) [14] model in [15] and [16]. This group has also recently published a direction preserving version of such a formulation based on a Petrov-Galerkin BEM scheme [17].

Once the choices in dimensionality, interpolation and mathematical notation are considered, the different formulations can be considered to be equivalent. The review of these formulations in the next chapter and the new SB-GA formulation presented in this thesis aim to make this equivalence clearer.

The term 'approximation space' used in the formulation alludes towards the presence of approximation in these methods. Collection and reflection of energy at surfaces always results in an approximation in both space and time, with the geometrical accuracy of exact reflection paths being degraded [7]. Repeatedly discretising higher order reflections in an SB-GA framework will not result in a solution similar to tracking individual rays, but that is not the aim – it is the spatial distribution of rays that describes acoustic intensity, and not individual rays that capture this information. From a theoretical standpoint, this is an important reason why classical Raytracing models employ receivers with some volume or area to average over, so cannot be 'point-like'. Following this hypothesis, tracing individual rays to a very high number of reflection orders forms one sample within a distribution. The explicit path travelled by a ray over many reflection orders is not important computationally [7]. Hence there is no advantage in using a computationally expensive wave solver to construct late-time sound fields, since energy-based algorithms providing an ensemble average of all responses are cheaper and sufficient [18]. This is perceptually appropriate for human listeners too, because the energy envelope is of primary importance at this time interval. SB-GA models are hence well suited to model the late-time interval in room acoustic responses. SB-GA exploits this relationship to simplify the algorithm and provide memory and computational benefits, with the degree of approximation being controllable. Also, once the boundary solution is computed for a specific number of reflection orders, receiver responses can be quickly recomputed as an additional stage independent of the boundary solution. This simplifies the process for multiple listening positions [9].

1.3 A NEW 'SURFACE-BASED' GEOMETRICAL ACOUSTIC FORMULATION

This thesis presents a new energy-based SB-GA formulation within a Galerkin BEM framework. It is referred to as Energy Boundary Element Method (EBEM) for the remainder of this thesis. It is to be noted that EBEM is not related to the Energy Finite Element Method (EFEM) based on the heat equation. As the name suggests, EBEM utilizes a Galerkin BEM

framework to map incoming energy onto the boundary. A novel aspect of this formulation is that it discretises incoming and outgoing energy separately, similar to recent formulations in high-frequency BEM [19]. The incoming and outgoing energy or power distributions are discretised with a weighted sum of basis functions in both space and direction. The Galerkin BEM framework computes the coefficients for these incoming or outgoing distributions by first computing a vector of 'projections'. This requires a second pair of integrals to be evaluated, involving a pair of 'testing' functions. Matching basis and testing functions will yield a 'Bubnov-Galerkin' method while different basis and testing functions results in a 'Petrov-Galerkin' method. The former will minimise the mean squared error in the same approximation or testing space as the solution and the latter minimises the mean squared error in some other space. Our EBEM is formulated with a 'Bubnov-Galerkin' scheme for simplicity and symmetry in basis, and synergy with high-frequency BEM in [19].

The coefficients of the desired distribution are subsequently found from the projections by solving a matrix equation involving a 'mass matrix', which is the identity matrix of the approximation and testing spaces. It is termed the mass matrix due to its similarity in definition with the mass matrix in FEM. This may appear to be an additional step, but: i) it is computationally cheap to solve because the mass matrix is usually sparse, and ii) it is this that provides the flexibility necessary to switch testing and basis functions at will, so allows easy comparison between other published schemes.

Hence, the Galerkin BEM framework expediates comparison of basis and test functions to analyse their effect on accuracy, convergence, and the properties of the boundary solution. The numerical implementation of EBEM is set up such that the factors required to compensate for these are moved outside the main solution part of the code, where they would have to be hard-coded, into a matrix multiplication.

Directional point source and receivers are also included. These are modelled with Fourier series in angle of arbitrary order. Stacking the Fourier coefficients into vectors means that all wave propagation operators can be described by matrix multiplications in EBEM. This is identical to the structure observed in a published framework for 'auralizing' BEM solutions including directional sources and receivers [20].

There have been suggestions that SB-GA may be computationally expensive even for a 'perceptual' algorithm, but these observations do not consider the crucial computational cost scaling with reflection order [9]. The numerical set up of the problem carries the majority of

the computational effort and EBEM is structured and implemented so that the problem set-up is performed at the pre-solution stage, easing numerical effort at the solution stage. The computationally intensive boundary-to-boundary interaction matrix is derived independent of the source position matching the structure in BEM [20], allowing source position and its characteristics to be readily changed. Angle dependent absorption is also implemented without any assumptions on incident sound direction.

The mathematical notation and structure of EBEM emphasises synergy with high-frequency BEM as noted in this section and can be considered as a possible route towards a mesh-based unified full auditory bandwidth algorithm for room acoustics [21].

1.4 THESIS OUTLINE

Chapter 2 presents and reviews the literature pertinent to this research. Relevant classical reflection-path-based GA models are discussed first, after which the majority of the chapter focusses on SB-GA methods. Formulations presented independently by three different research groups are reviewed.

Chapter 3 introduces relevant background theory and describes the theoretical framework for the EBEM formulation. All acoustic propagation processes are described, and the boundary integrals are derived. The Galerkin BEM framework is then presented, followed by the final algorithm structure.

Chapter 4 introduces a validation model and provides justification for the choice of algorithm used for validating EBEM The methodology for numerically implementing and validating the developed EBEM model is developed, and the numerical quadrature rules used for evaluating EBEM integrals are detailed.

Chapter 5 presents the results of the validation study and **Chapter 6** discusses these results. The discussion focuses on the accuracy and convergence, as well as approximation introduced in the solution as a result of the various angular basis schemes studied.

Chapter 7 draws conclusions from the thesis and its results and presents avenues to further develop the EBEM formulation.

2 LITERATURE REVIEW

This chapter reviews the literature relevant to EBEM. The first part of the chapter reviews classical GA methods with the focus of this chapter falling on SB-GA methods which follows. The state-of-art SB-GA formulations independently developed by different research groups are discussed, reviewed, and compared.

2.1 GEOMETRICAL ACOUSTICS

Geometrical Acoustics (GA) is an umbrella category for several algorithms which simplify the laws of acoustical propagation and follow the postulate of *geometrical* propagation of sound in straight lines in homogenous media. This ray or particle assumption of propagation is as an idealisation of the plane wave [4]. GA models inherently ignore the wavelength and wave properties of sound including its transmission effects. These assumptions are only valid at high frequencies where the propagating wavelength is small when compared to the dimensions of the room, the boundaries and all of its details. The geometric propagation assumption fails at low frequencies where wave effects are significant and important to include. They are also inaccurate in smaller rooms, where a low modal density extends up to high frequencies. But its conceptual simplicity and the ease with which it constructs practical sound field makes GA an attractive option for computerised modelling of room acoustics and it has dominated the field for decades.

The earliest noted use of ray-based acoustics was by Sabine in the 1900s to investigate sound propagation paths using Schlieren photography [27]. This was the first step towards considering a ray-based approach to modelling sound and laid the foundation for computerised Raytracing [7]. The development towards a fully workable model for room acoustics required a few intermediate steps, notably computing mean free path lengths using a ray-based approach [22] and the subsequent determination of decay functions for 2D rectangular rooms [23]. During the same period, methods following similar assumptions were developed in the fields of computer graphics, optics and underwater acoustics aimed at solving different problems. The seminal paper describing use of Raytracing in computer graphics [24] was published the same year as Krokstad *et al* proposed the first 3D room acoustic model, capable of handling multiple receivers [25]. But this formulation was still limited to a qualitative investigations of reflection angles and early echograms. Overlap in research methodology and the clear use of ray-based propagation was evident in both papers, although these were developed independently [7]. The term 'auralisation' was coined by Kleiner and Dalenbäck in [26], defining the process of rendering the sound field in rooms from numerical models. The basic principles of such systems were outlined earlier by Schroeder in [27] within the context of concert hall acoustics. Limited by the computational power available at that time, GA was deemed to be the only practical approach to room acoustic and concert hall modelling. Full room models did not become practically tractable until the eighties, which were then used as a quantitative tool for modelling room acoustics in 1/1 octave frequency bands. With advancements in computing power over the decades, the use of computer modelling for room acoustics has become increasingly popular and instigated similar research in other fields like computer gaming to render realistic real-time audio [7].

Deterministic GA models such as ISM are commonly used to model high frequency early reflections which are sparse in time. But ISM's computational cost scales exponentially with reflection order, which limits it to modelling low order early reflections. For modelling late-time in room acoustic responses, when the sound field is very diffuse and chaotic, it is appropriate to operate a computationally cheaper model as only the energy decay envelope is important perceptually, and individual reflections are indistinguishable. Stochastic GA models such as classical Raytracing are typically used for this purpose.

Wave effects like scattering and diffraction can be important to include in room models, but are not naturally included in GA. GA models such as Raytracing maintains its linear computation cost with reflection order when no ray splitting is modelled i.e., one ray arriving

at a boundary results in one ray being reflected. When these diffraction or scattering are included as an additional process with Raytracing, they produce additional rays at each reflection order due to ray splitting which cripples Raytracing with an exponential computational cost with reflection order. This is shown in Figure 2.1. Moreover, only very low fidelity Monte Carlo models of boundary scattering and diffraction can be included with Raytracing without losing its attractive linear computational cost with reflection order.

Figure 2.1 Raytracing (a) with no ray-splitting (b) with ray-splitting due to scattering and diffraction

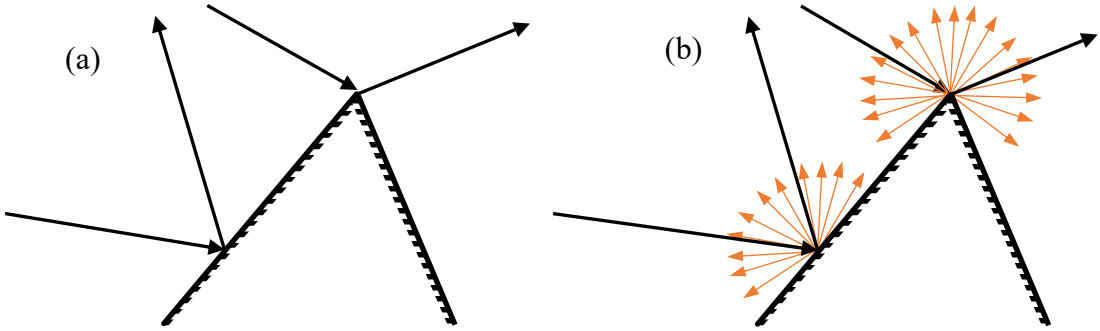

GA models can be generalised into two categories: Reflection-path-based models and "Surface-Based" models. The rest of this section focuses on reflection-path-based models pertinent to this thesis. SB-GA models are discussed and reviewed in Section 2.3.

2.1.1 Image Source Method

ISM constructs a solution from simple omnidirectional sound sources that individually satisfy the PDE that describes the acoustic propagation in the solution domain. The basic building block of ISM is the Image Source solution, applied to a sound source in a room to produce an explicit expression for a wave reflected at a boundary. ISM is very effective for smooth boundaries but is constrained at higher reflection orders limited by its exponential computational cost scaling with reflection order.

Figure 2.2 Construction of a first order image source by the image source solution. A is the source in the room, A' is the image source, and B is the receiver in the room [4]

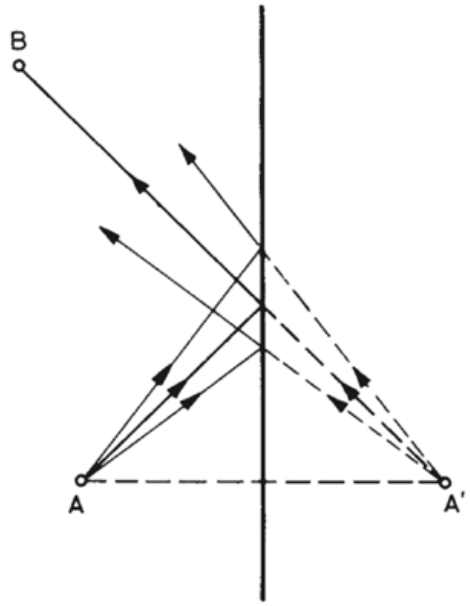

The ISM mechanism reflects all sources in a room against all the room boundaries, producing a set of Image sources (IS). These are subsequently reflected against all the boundaries in the respective rooms to produce the next set of ISs. This process is repeated for a required number of reflection orders – all permutations of the boundaries must be considered for reflection. If reflections are modelled to be purely specular, the sound paths – rays – can be backtracked from receiver to the source. A difference between this and classical Raytracing is that this is a single ray path direct from a source to a point receiver, not a distribution. Because of this, energy spreading with distance must be directly computed, since there is no ray-spreading present to include it implicitly.

Assuming all the ISs radiate the same signal at the same initial time as the original source in the room, the contribution from each IS to the receiver in the room replicates the contribution from one reflection path from the source to the receiver in the room. The power density can now be computed by summing the contributions of all valid ISs. The construction of ISM with reflection order is similar to the methodology for Raytracing; an IS solution of n^{th} order corresponding to a ray hitting n walls [1].

Figure 2.3 A rectangular room (solid line) with the original source (o), first order image sources (*), second order image sources (o) and third order image sources (triangle) in their respective image rooms (dashed lines) [7]

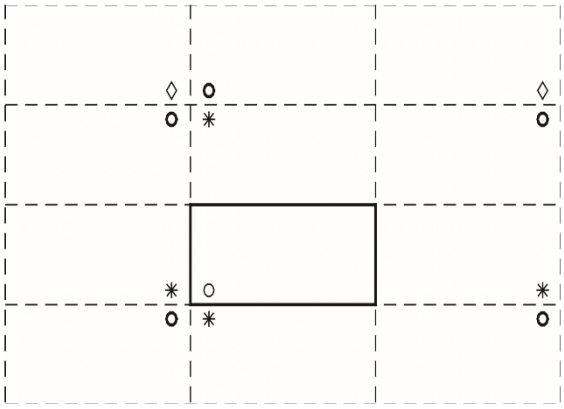

Early research leading to ISM for room acoustics began with investigations into canonical problems, such as an infinite wedge and later extended to shoebox rooms, by Cremer [28] and later by Mintzer [29]. The first computerised ISM model was proposed by Gibbs and Jones to compute sound power levels in a rectangular room [30], like the one shown in Figure 2.3.

Simplicity of ISM is its main advantage but it is normally limited to low order early reflections as the number of IS rises exponentially with reflection order. Generalising for a room with N edges, the number of IS generated for the K^{th} order reflection is:

$$\sum_{k=1}^{K} N(N-1)^{k-1} \qquad \textbf{2.1}$$

In the case of a rectangular room like the one shown in Figure 2.3, certain IS positions overlap and are degenerate, making the valid number of IS used for a specific reflection order significantly less than predicted by eq. 2.1. But in an arbitrary-shaped room, eq. 2.1 holds.

Strictly speaking, the IS solution is exact only for spherical incidence and cuboid geometries with boundary impedance of either -1 or $+1$, meaning perfectly rigid or pressure-release boundary conditions respectively. For non-rigid boundary conditions, the approximation can be good so long as the angle of incidence for rays at the boundary are small and away from grazing incidence [1]. Deviating from a convex geometry with the corners having opening angles which are not rational multiples of π, the total field is no longer the sum of the direct

sound and the sound fields from all the ISs. In this more general case, diffraction must be included to obtain accurate results. This must be added as an additional process [31].

When extending ISM to arbitrary geometries, additional checks are required in addition to recursively applying the IS solution. The relevance of each IS w.r.t. to each receiver position must be checked. Figure 2.4 shows these "audible" image sources for first and second order reflection orders. These audibility computations can be optimised by using a beam-tracing algorithm which pre-computes visibility of each IS and stores it as a beam tree [1].

Figure 2.4 Image source audibility test for first and second order reflections. S is the source in the room, R and R' are the receiver positions in the room, S_1 and S_2 are first order image sources and S_{12} and S_{21} are second order image sources [1].

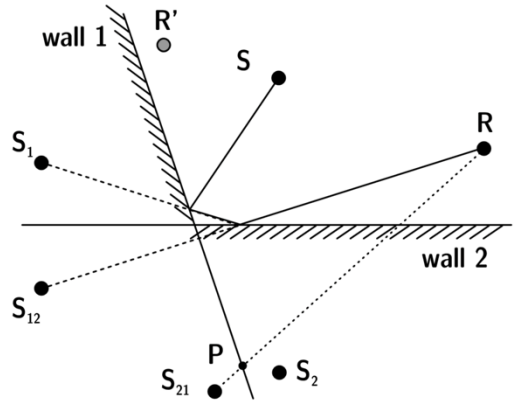

2.1.2 Classical Raytracing

Raytracing models acoustic propagation in a room by emitting a distribution of particles or rays from a source simultaneously in all directions, then reflecting these against boundaries and tracking valid reflection paths from the source to the boundary. Emission from the source can either be with a pre-determined distribution or via a Monte Carlo process. The following figure shows such a valid ray path from source to receiver.

Figure 2.5 Tracing a ray from a source to receiver and a time histogram of the number of detected rays (represented by dots) at each time step [1]

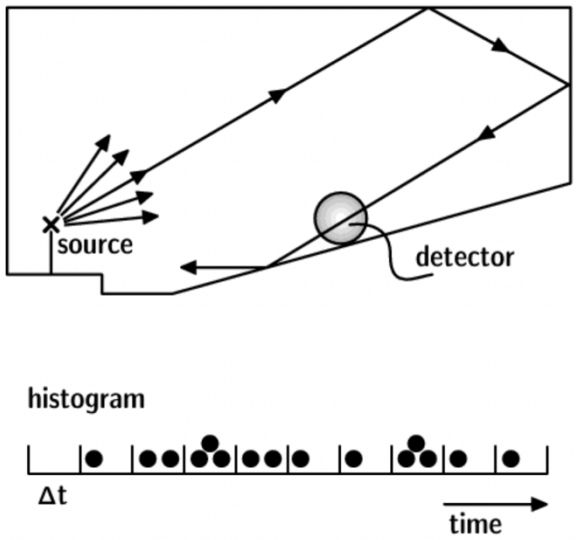

The first instance of computerised Raytracing was implemented to calculate mean free paths in rectangular rooms [22], but the first paper on computing time-energy responses for 3D geometry was proposed by Krokstad *et al* [25] a decade later. These algorithms model reflections as purely specular. Later, Kuttruff extended the methodology to implement diffuse reflections in 1971 [25]. Heinz then extended the model to include diffuse rays in shadow regions, termed 'diffuse rain' [32]. This addition computes the visibility of all diffuse 'child' rays to the receiver accounting for the angle of reflection and solid angle covered by the receiver, also allowing point receivers [7].

A critical parameter dictating accuracy of Raytracing models is the number of rays modelled for a particular study, in addition to the approximation due to the omission of wave effects. As only a finite number is rays are possible to be modelled realistically, the solution will be approximate. Raytracing models accommodate boundary absorption and ray termination in two ways:

1. Attenuating the energy carried by a ray upon reflection by a factor determined by the boundary material properties. For instance, the energy carried by a ray can be attenuated by multiplying the incident energy by a factor of $(1 - \alpha)$, where α is the boundary absorption coefficient. The obvious advantage of this method is the ability to use frequency dependent absorption. Rays are then terminated when either:
    a. A maximum ray travelling distance (or time) is reached, or
    b. The energy carried by the ray reaches a minimum threshold.

2. The ‘annihilation’ approach where a probabilistic condition of a ray getting terminated on incidence at a boundary is imposed. This probability term is dependent on the boundary material properties. Highly absorbing boundaries lead to rays to more rays getting annihilated when compared to more reflective surfaces.

Both these methodologies yield identical results in the limit of large ray numbers, but differences exist in computation time and efficiency. The annihilation is superficially more efficient because the number of rays reduces with reflection order. But it is also less accurate because it does not allow absorption factors in frequency bands and because termination of rays leaves a smaller statistical basis for higher reflection orders [1].

An important drawback of the Raytracing formulation is the inability to include point receivers. As implied above, Raytracing does not terminate rays when they come in contact with receivers – they pass though unobstructed. Only the energy carried by the ray and the time since source radiation is computed and logged. Ideally, detectors would be point-like, but the probability of a ray hitting a point is infinitely small. Hence this imposes the need for volumetric or surface receivers. This present issues such as [7]:

a. Detection of the same reflection paths multiple times, and/or
b. Detecting paths which are invalid for the specific receiver position.

Raytracing maintains a linear computational cost with reflection order. This is dependent on using a boundary reflectance model that includes no ray splitting – it must give one ray out for every one ray in. To representatively model the late-time part of room impulse responses, the algorithm must handle scattering and diffraction effectively, since this governs the transition to a diffuse field and is important for realism [33]. Similar to ISM, Raytracing does not naturally include either of these processes in its framework, so they must be separately included where required. Various techniques have been proposed to include diffuse reflections; majority of them work on either of these principles:

a. On reflection there is a chance of the ray being reflected specularly or randomly based on the scattering coefficient.
b. Producing several “child” rays from each “parent” ray when it is reflected at boundary surface.

Figure 2.6 Methods of including scattering with Raytracing (a) Non-specular ray redirection method (b) Producing additional 'child' rays at each reflection order in addition to the specular reflection

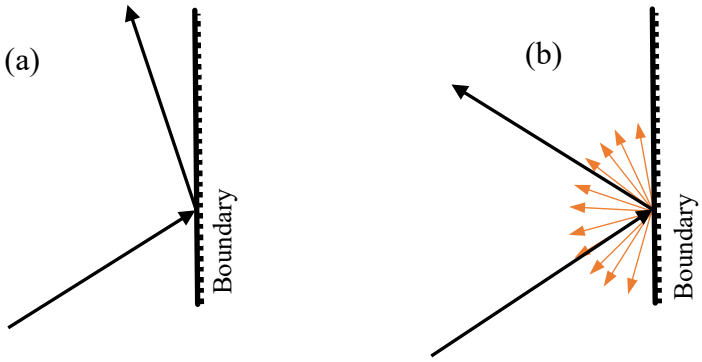

Principal (a) is computationally efficient as no additional rays are produced at each reflection. The scattering distribution is captured on average over many reflection instances (rays and reflection orders) via a Monte Carlo process.

Principal (b) is more accurate since it captures the scattering or diffraction distribution at each reflection, but it leads to ray splitting, and therefore an exponentially increasing number of rays with reflection order. It can, however, be useful in modelling outdoor scenes, where the rate of loss of rays (into the sky) counteracts the production of extra rays by ray splitting, and the relative importance of each reflection justifies the extra computational cost. But in rooms the rays are trapped, and the computational cost is prohibitive. Recent work based on pre-computed edge-to-edge visibility graphs to accelerate computation with these additional diffracted rays – but this was only applied to 'direct' diffraction and the algorithm retains the prohibitive exponential computational cost with reflection order [34].

2.2 "Surface-Based" Geometrical Acoustics

An emerging solution to address the issues faced by Raytracing when modelling late reflections is "Surface-based" GA. These models use room boundaries as surfaces for intermediate storage of acoustic energy. A limitation is that collecting and discretising energy at boundaries leads to an approximation and the geometrical accuracy of exact ray like paths degraded [7]. But this is not inappropriate for late-time, where the highly diffuse and chaotic sound field means that individual reflections cannot be distinguished anyway.

SB-GA interpolates the solution with a pre-defined 'approximation space'. Spatially this is based on elements in a boundary mesh and the interpolation (or 'basis') functions can be those

used in standard FEM or BEM; discontinuous piecewise-constant (PWC) or continuous piecewise-linear (PWL) are simple low-order choices. For interpolation w.r.t. reflection angle, many DOF are required to capture the angular distribution on the boundary. This could either be as a high order family of PWC functions arranged over non-overlapping angular ranges or continuous orthogonal polynomials such as Legendre, Chebyshev or Lobatto – in order to capture the dependency on angle that arises for early reflections. SB-GA thus operates similarly to how BEM models low frequencies, except that it discretises power flow and also considers propagation angle.

A crucial feature of SB-GA is its ability to maintain a linear computational cost with reflection order. This feature holds even if ray splitting processes like scattering or diffraction occur at each reflection order [35]. Rays arriving on the boundary from different directions can contribute to the same energy 'block'. The 'child' rays produced are absorbed into the approximation space. Reflections are simplified to matrix multiplications and the DOF remains constant, maintaining a linear computational cost.

Authors of Raytracing models acknowledge that it is the spatial distribution of rays – not individual rays – that represent acoustic intensity. This is why point receivers cannot be used. It is tempting to think that the paths of individual rays are important – as concerned Pohl and Stephenson [35] – but this is not the case at high reflection orders, as a chaotic sound field is present at this stage and fine details of individual ray directions are not perceptually important to human listeners. What the Raytracing algorithm is propagating is a sampling of a probability distribution, the latter being which is what actually represents acoustic intensity in the model. This is of even greater importance when including boundary scattering as the increase in reflection density makes individual reflections irrelevant. SB-GA exploits this principle to simplify the algorithm and ease computational effort.

Another important advantage is the simplification of computing receiver responses. These can be quicky recomputed, or computed together for multiple receiver positions, once the boundary solution has been computed [9]. This article also suggests that SB-GA might be computationally expensive but does not discuss the crucial computational cost scaling trends explained above. Efficient problem set up is of utmost importance.

The earliest algorithm in this category is the Radiosity method proposed by Kuttruff in the 1970s [8]. An important distinction between Radiosity and reflection-path-based-GA is the assumption of ideally diffuse reflections, thus it ignores the directionality of sound arriving at

the boundaries. All reflections are assumed to scatter by Lambert's law. The results from a Radiosity model are useful for late reflections which tend to be diffuse in practice.

More recently, sophisticated SB-GA models with parametrise reflection directions have emerged. Such models have been independently developed by three different research groups. These are presented in the following sections.

2.2.1 The Duke Group

Franzoni, Bliss and Rouse formulated a boundary element method based on energy/intensity variables in 2001 [10]. The basic building blocks of the algorithm are infinitesimally small uncorrelated broadband sound sources. A continuous distribution of these infinitesimally small sources is used to model the boundary, and the radiations from these sources are used replicate the sound field in a room. The assumption of these sources being uncorrelated holds so long as the simulated wavelengths are short, compared to the room dimensions, and the boundary absorption being not too large. The plane wave assumption is abandoned here and replaced with this distribution of sources for modelling spreading waves from the boundary.

For a broadband sound field, the sources modeling the boundary will be correlated to some degree, over a short distance, typically less than one wavelength from the boundary. This local correlation between adjacent sources introduces a directivity effect for each boundary source. The source power and directivity coefficients for each of the boundary sources are computed in an iterative manner, modelling diffuse reflection first, followed by specular reflections. The directivity was limited to first order with three terms in the Fourier series expansion in angle in full space applied to a half-space. Rouse and Franzoni presented an improvement to the EI-BEM formulation in 2005 [11] to allow unlimited terms in the Fourier series expansion completely applied over the half space. This series expansion no longer limited to three terms. The non-orthogonality issue with [10] arising from using a standard Fourier series in the range from 0 to π, which results in the different orders (harmonics) of the series being non-orthogonal over this range, is solved. The source power and receiver coefficients can now be determined directly in a non-iterative manner.

Figure 2.7 A rectangular room with an internal source and boundary replaced by a distribution of sources [10]

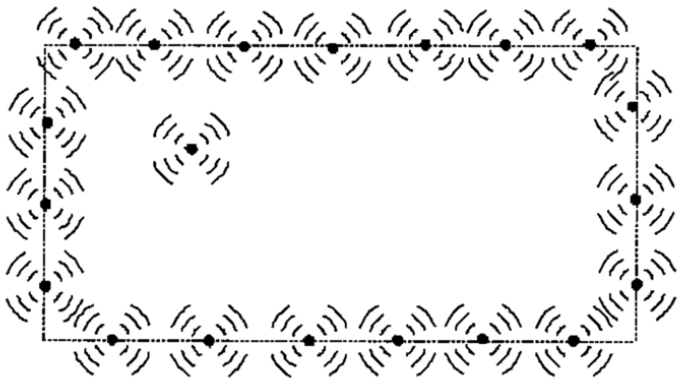

The theoretical development of time-averaged governing equations in energy density and intensity were recast to develop EI-BEM as:

$$\vec{\nabla} \cdot \vec{I} = 0 \qquad \textbf{2.2}$$

and

$$\frac{1}{2}\,\rho_0 \left\langle \vec{u}(\vec{\nabla}.\vec{u}) - (\vec{u}.\vec{\nabla})\vec{u} \right\rangle + \vec{\nabla}E = 0 \qquad \textbf{2.3}$$

Where:

$\vec{I}$ is the time averaged sound intensity

ρ_0 is the density of air

$\vec{u}$ is the velocity vector

E is the time averaged energy density

The time averaged velocity term $\langle u(\nabla.u) - (u.\nabla)u\rangle$ is identically zero for a 1D sound field and remains zero for higher dimensions if the waves are assumed to be uncorrelated, broadband, random incidence plane waves. To have a non-zero time-averaged velocity term and to model spatial variation of source pressure, the plane wave assumption was abandoned in favour of uncorrelated sources used to model spherical waves from the boundary. This assumption also allows adding source pressure in the interior of the room in a mean-square sense at distances outside the limits of the correlation layer close to the boundary. The similarity

with the Equivalent Source Method [4], although a high frequency version, is evident from Figure 2.7.

Once the normal velocity at the boundary is computed, the sound pressure reflected from the boundary can be computed as the integral of a Green's function over the boundary. The Green's function is a 2D free-field monopole here. To compute the total reflected mean-square pressure, the pressure contribution from the entire boundary for a specific frequency at a specific angle of incidence is obtained and integrated over all angular and frequency values. This was then used to obtain the equations to describe mean-square pressure and intensity radiated by each source on the boundary as:

$$\bar{p}_G^2 = \frac{\rho_0 c W}{2\pi r} D(\phi) \qquad \textbf{2.4}$$

and

$$\mathbf{I}_G = \frac{W}{2\pi r} D(\phi)\mathbf{e}_\phi \qquad \textbf{2.5}$$

Where:

W is the source power

D is the directivity function

r is the distance from the source to point of evaluation (in m)

ϕ is the angle measure w.r.t. surface normal

These equations include the spreading term used in computing receiver responses. As each of these sources on the boundary radiate in all directions, into and away from the interior of the room, the 'reflected' power generated into the room from a source will be half of the source power W. The directivity was derived by studying the acoustic intensity at a surface computed in two different ways:

1. Summing uncorrelated waves reflected at the boundary.
2. Replacing the boundary with uncorrelated sources and summing contributions from each source.

This is illustrated in Figure 2.7. The directivity function $D(\phi)$ was constrained with the following equation to conserve energy:

$$\int_{-\pi}^{\pi} D(\phi)\, d\phi = 2\pi \qquad \textbf{2.6}$$

Comparing the normal intensity incident at the surface from both methods mentioned above, the product of intensity reflection coefficient R_I which is the ratio of intensity of reflected wave relative to the incident, and the magnitude of incident intensity can be expanded utilizing a Fourier series in angle as:

$$R_I(\theta)\ \frac{P_{inc}^2(\theta)}{\rho_0 c} = \sum_{n=0}^{\infty} [A_n \cos n\theta + B_n \sin n\theta] \qquad \textbf{2.7}$$

This equation discretises outgoing sound. This equation is modified in [11] to include a factor of 2 in the sine and cosine arguments to improve convergence. This factor of 2 means that the discretisation in only in a semi-circle, or a halfspace of directions. The modified equation is presented below. This is a more realistic model of practical angle dependent sound fields. Both versions for this equation in [10] and [11] are appropriate, but the latter exhibits faster convergence.

$$R_I(\theta)\ \frac{P_{inc}^2(\theta)}{\rho_0 c} = \sum_{n=0}^{\infty} [A_n \cos 2n\theta + B_n \sin 2n\theta] \qquad \textbf{2.8}$$

Also, now the Fourier series terms are orthogonal over a half interval and the coefficients can be found directly without solving a matrix equation. Although eq. 2.8 assumes periodicity of the angular distribution at $\theta = \pm 90°$. A better choice is to use a Cosine series or Legendre polynomials like the Nottingham group and EBEM do, as this would avoid the issue with periodicity encountered in this version of the formulation.

Figure 2.8 Incident and reflected pressure waves at a point (x,y) on a surface and a boundary point corresponding to a source [11]

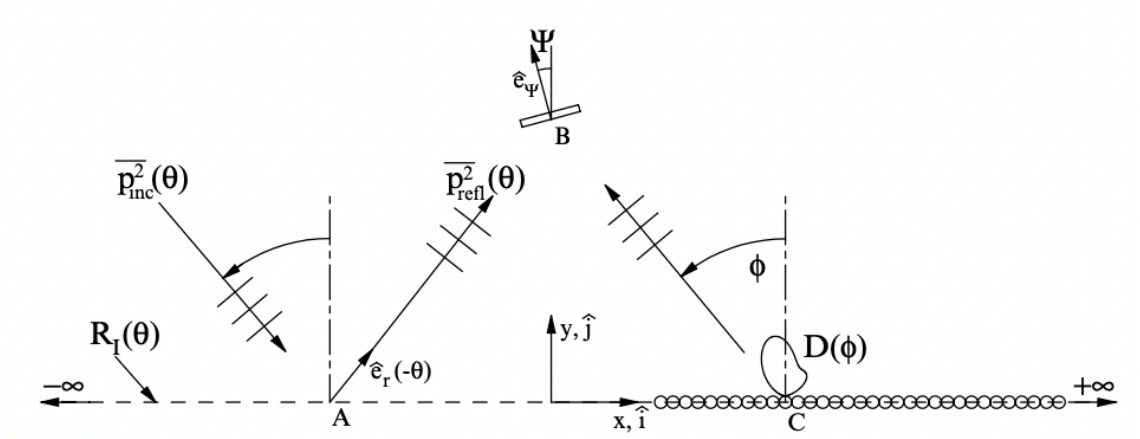

The source radiation can now be represented by a Fourier series expansion of product of the intensity reflection coefficient and the magnitude of time and the time-averaged incident intensity as:

$$\frac{\rho_0 cW}{2\pi} = \cos\phi \sum_{n=0}^{\infty} [A_n \cos 2n\phi + B_n \sin 2n\phi] \qquad \textbf{2.9}$$

The Fourier series coefficients are computed from the normal and tangential intensity components on an evaluation node on the boundary. The boundary integral equation is derived relating variation of source power on the boundary to the acoustic power of these uncorrelated sources. Consider a 2D enclosure with the boundary described by the surface S shown in Figure 2.9. The enclosure boundary is replaced by a continuous distribution of energy/intensity sources of strength dW/dS (power per unit length) and directivity $D(\theta_1)$ which can vary for each individual boundary source. A source at r_1 produces an intensity at a boundary point $\mathbf{r}_s$ given by:

$$\mathbf{dI}(\mathbf{r}_s) = \frac{(dW/dS)(\mathbf{r}_1)D(\theta_1)}{2\pi|\mathbf{r}_s - \mathbf{r}_i|} \cdot \frac{(\mathbf{r}_s - \mathbf{r}_i)}{|\mathbf{r}_s - \mathbf{r}_i|} \mathrm{dS} \qquad \textbf{2.10}$$

Figure 2.9 An enclosure with a boundary described by a continuous distribution of uncorrelated sources [10]

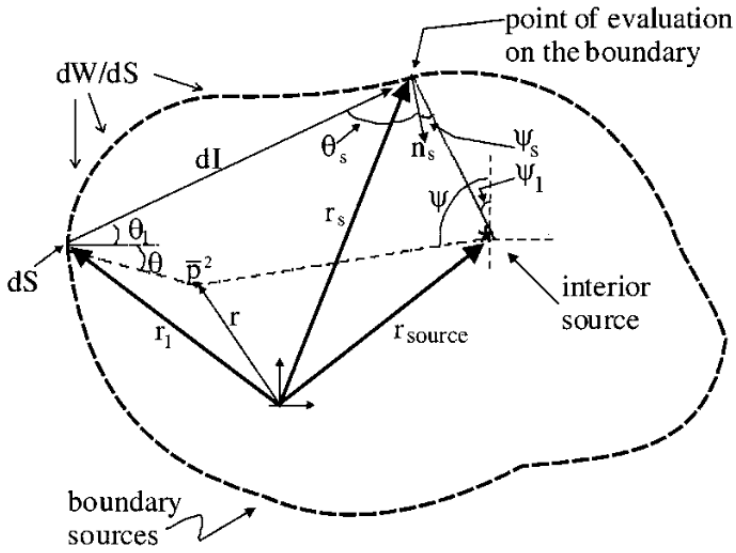

Here $D(\theta_1)$ is the directivity of the boundary source in the direction of the evaluation points and dS is the incremental surface area. The total incident energy at the point of evaluation on the boundary is obtained by an integral over all incident intensities that contribute at that point:

$$\mathbf{I}(\mathbf{r}_s) = \oint_s d\,\mathbf{I}(\mathbf{r}_s) \qquad \textbf{2.11}$$

Boundary effects such as angle dependent absorption are included as a function of the directional reflection coefficient $R_I(\theta_S)$ and the normal component of intensity. The normal component of reflected intensity is given by:

$$\mathbf{n}_s.\,\mathbf{I}_R(\mathbf{r}_s) = \oint_S R_I(\theta_S)\,\mathbf{n}_s\,.\,d\mathbf{I}(\mathbf{r}_s) \qquad \textbf{2.12}$$

Where $\mathbf{n}_s(\mathbf{r}_s)$ is the unit normal into the enclosure from the boundary at point $\mathbf{r}_s$. The incremental intensity emitted from the point located at $\mathbf{r}_s$ is equal to $(dW/dS)(\mathbf{r}_s)$.

The incoming intensity vectors interact with the boundary to include effects like absorption to obtain the reflected intensity. Applying conservation of energy at point $\mathbf{r}_s$ leads to the boundary condition integral equation:

$$\frac{dW}{dS}(\mathbf{r}_s) = R_I(\psi_S)\mathbf{n}_s(\mathbf{r}_s).\mathbf{I}_{\text{source}}(\mathbf{r}_s) + \oint_S R_I(\theta_s)\mathbf{n}_s(\mathbf{r}_s)\,.\,\mathrm{d}\mathbf{I}(\mathbf{r}_s) \qquad \textbf{2.13}$$

The quantities in this equation are defined in Figure 2.9. In this approach, each boundary element is assumed to have constant strength, dW/dS, equivalent to the piecewise-constant discretisation we will employ. The discretized version of the above boundary condition equation is applied by a collocation approach at the midpoint of each boundary element, resulting in a system of equations to solve for the source strengths. This is different to the Galerkin scheme employed by EBEM. The collocation scheme is less accurate and typically converges slower. This is because it minimises error only at the collocation point. In contrast, Galerkin schemes minimise Root Mean Squared error over the entire element. But collocation schemes are computationally cheaper since there is only one boundary integral to be evaluated and not two.

To calculate the mean square pressure at a point $\mathbf{r}$ in the interior, the contribution from all boundary infinitesimal sources and the interior sources in a room are summed:

$$\overline{p^2}(\mathbf{r}) = \oint_S \rho_0 c \frac{dW}{dS}(\mathbf{r}_1)\frac{D(\theta)}{2\pi|\mathbf{r}-\mathbf{r}_1|}dS + \sum_{\substack{\text{interior}\\ \text{sources}}} \rho_0 c\, W(r_s)\frac{D_s(\psi)}{2\pi|\mathbf{r}-\mathbf{r}_{\text{source}}|} \qquad \textbf{2.14}$$

A system of equations was formulated assuming Lambertian directivity to obtain boundary source powers. An iterative algorithm using the previously computed source power values solves the equations to obtain source powers and directivity terms for subsequent reflections.

The improved EI-BEM model [11] uses eq. 2.13 as the starting point and the values of the coefficients are found by exploiting the orthogonality of the trigonometric functions. The boundary is now discretised by a Fourier series in half-space and the system now being orthogonal. The Fourier coefficients for each element in the mesh are now related to all other elements and energy radiated by interior sources in the room. This leads to solving a system of equations to obtain the unknown Fourier coefficients for each element. Directivity functions for two elements in an EI-BEM model are compared for the iterative and direct EI-BEM models below.

Figure 2.10 Comparison of directivity functions with iterative and direct approaches to EI-BEM [11]

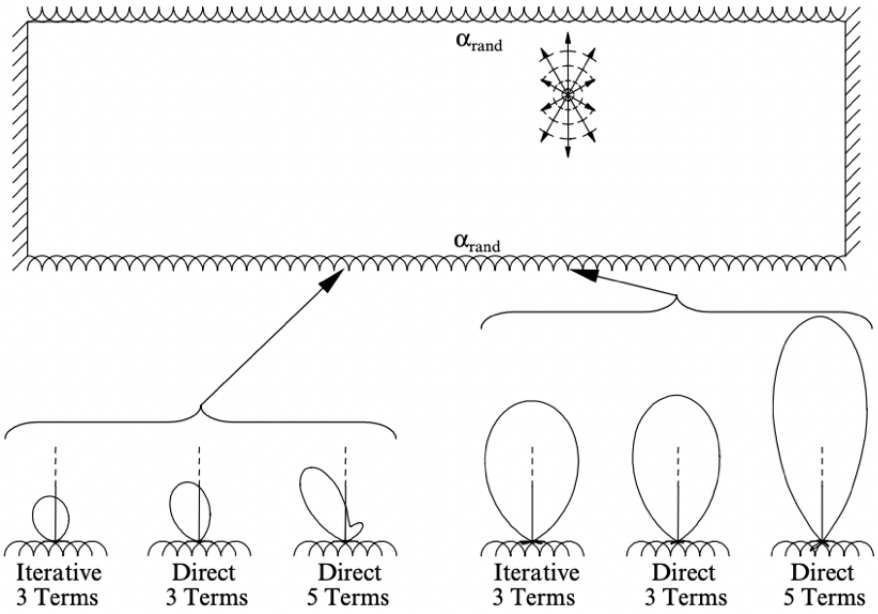

The direct solution achieves better accuracy compared the iterative method, which computes the magnitude of the Fourier series terms approximately. The ability to use more terms in the Fourier series expansion for the directivity function leads to improvement in their resolution. Specular reflections are modelled more accurately with these higher order harmonics and the reflections tend to being less diffuse.

The off-axis source is seen to exhibit different directivities with different amplitudes for three terms for iterative and direct EI-BEM. The on-axis source with five terms in its Fourier series which was selected as the truncation limit for practical application in [11] shows higher amplitudes, hence the received power in the interior is associated with fewer number of elements, radiating higher amplitudes.

Although this formulation is limited by the number elements in the boundary mesh and the number of Fourier series coefficients for each element, the improved direct EI-BEM model is able to accurately model higher order specular reflections.

After a 14 year gap, the Duke group revisited their EI-BEM formulation in 2019 [36] Here the aim was to verify the method against an exact solution for a cuboid room, which is also derived in the paper. The verification was repeated with one and two dipole sources in the room. The wave equation was solved in the test room by dividing it into in two unequal cuboid spaces separated by the horizontal plane containing the dipole source(s). The dipole null line

was aligned parallel to the absorptive walls to prevent fluttering and 1D modes caused by the parallel rigid boundaries. The results show good agreement with the exact solution other than at the centre line between the two dipoles. This issue is due to the interior sources being spatially uncorrelated, and is a correctable limitation in the code implementation – it is not a fundamental limitation with the iterative EI-BEM. This does not occur in space immediately adjacent to the source where correlation effects are strongest. The direct model does not overshoot the solution near the source like the iterative results do and exhibits excellent agreement with the exact solution.

2.2.2 The Helsinki Group

Siltanen *et al* proposed the Room Acoustic Rendering Equation (RARE) in 2007 as a framework to describe several GA algorithms within the limits of local reaction [12]. Within this paper they also propose the Acoustic Radiance Transfer (ART) algorithm, which extends the Radiosity method [37] with the ability to model directional reflections in addition to diffuse ones following Lamberts law [38]. This is seen a step towards more realistic reflection models, while retaining the benefits of element-based techniques. As with Duke's EI-BEM, the acoustic quantity modeled in ART is energy and phase information is neglected.

RARE assumes the geometry $\mathcal{G}$ is represented as surface elements or patches, and the formulation recursively calculates the outgoing time dependent acoustic energy l at a surface point $\mathbf{x}'$ at an angle Ω:

$$l(\mathbf{x}', \Omega) = l_0(\mathbf{x}', \Omega) + \int_{\mathcal{G}} R(\mathbf{x}, \mathbf{x}', \Omega) l(\mathbf{x}, \Gamma) dx \qquad \textbf{2.15}$$

Where $l(\mathbf{x}', \Omega)$ is the time-dependent outgoing radiance from a surface point $\mathbf{x}'$ in the direction Ω. It is written as a sum of two terms:

1. the radiance emitted by the surface itself, $l_0(\mathbf{x}', \Omega)$
2. the radiance from all other surfaces in the enclosure via the surface point $\mathbf{x}$

The latter term is written as an integral over the whole geometry $\mathcal{G}$. The radiance from a surface point, $\mathbf{x}$ towards the point $\mathbf{x}'$ is $l(\mathbf{x}, \Gamma)$, where Γ is the direction of radiance from $\mathbf{x}$ to $\mathbf{x}'$. Since only a fraction of the radiance leaving point $\mathbf{x}$ will be incident on $\mathbf{x}'$, the radiance is multiplied by the reflection kernel R:

$$R(\mathbf{x}, \mathbf{x}', \Omega) = V(\mathbf{x}, \mathbf{x}')\rho(\mathbf{x}', \Theta, \Gamma)g(\mathbf{x}, \mathbf{x}') \quad \textbf{2.16}$$

The visibility function $V(\mathbf{x}, \mathbf{x}')$ extends applicability to non-convex room geometries. It yields a value of 1 if the line from $\mathbf{x}$ to $\mathbf{x}'$ is unobstructed, and 0 otherwise.

$\rho(\mathbf{x}', \Theta, \Omega)$ is the Bidirectional Reflectance Distribution Function (BRDF) which gives the ratio of incoming and outgoing energy as a function of incoming (Θ) and outgoing angle (Ω), for a given frequency. It describes the fraction of radiance incident at point $\mathbf{x}'$ which is reflected in the angle Ω. BRDFs describe the material of the surface and they are used to model different types of reflections within the RARE.

Figure 2.11 A Bidirectional Reflectance Density Function (BRDF) represents the directional distribution of energy reflected for one incident angle [12]

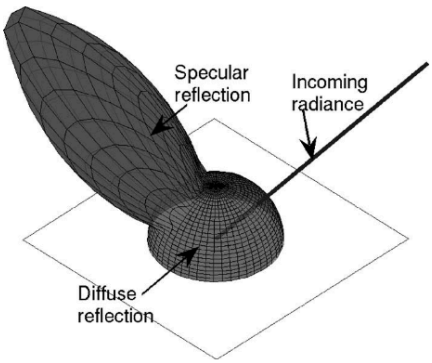

$g(\mathbf{x}, \mathbf{x}')$ is the geometry term considering propagation delay, air absorption and the form factor, which is defined by the relative orientation of the two surfaces.

Figure 2.12 Calculating the geometry term between two points x and x' [39]

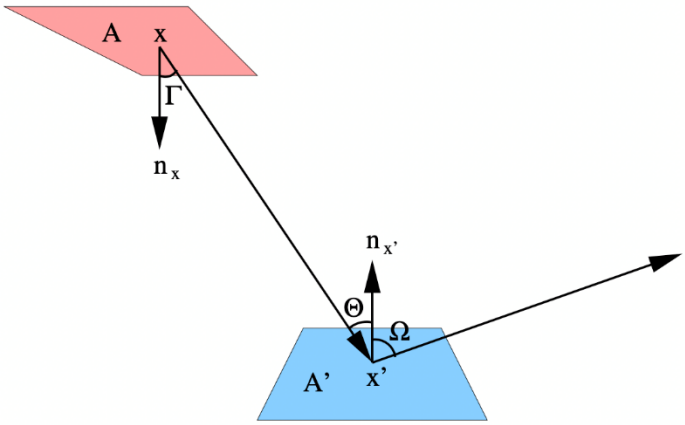

Surface normal at the points $\mathbf{x}$ and $\mathbf{x}'$ are $\mathbf{n}_{\mathrm{x}}$ and $\mathbf{n}_{\mathrm{x}'}$ respectively. The cosine of the incident angle at point $\mathbf{x}'$ gives:

$$\mathbf{n}_{\mathrm{x}'} \cdot \frac{(\mathbf{x}-\mathbf{x}')}{|\mathbf{x}-\mathbf{x}'|} \qquad \textbf{2.17}$$

and the cosine of the outgoing angle at point $\mathbf{x}$ equals:

$$\mathbf{n}_{\mathrm{x}} \cdot \frac{(\mathbf{x}'-\mathbf{x})}{|\mathbf{x}'-\mathbf{x}|} \qquad \textbf{2.18}$$

The form factor between small elements represented by points $\mathbf{x}$ and $\mathbf{x}'$ is defined by their relative angles Θ and Γ and by their mutual separation.:

$$F(\mathbf{x},\mathbf{x}') = \frac{\cos(\Theta)\cos(\Gamma)}{|\mathbf{x}-\mathbf{x}'|^2} \qquad \textbf{2.19}$$

These factors, along with the propagation operator $S_{|\mathbf{x}-\mathbf{x}'|}$ and the quadratic fall off, formulate the geometry term:

$$g(\mathbf{x},\mathbf{x}') = \left[\mathbf{n}_{\mathrm{x}} \cdot \frac{(\mathbf{x}'-\mathbf{x})}{|\mathbf{x}'-\mathbf{x}|}\right]\left[\mathbf{n}_{\mathrm{x}'} \cdot \frac{(\mathbf{x}-\mathbf{x}')}{|\mathbf{x}-\mathbf{x}'|}\right]\frac{S_{|\mathrm{x}-\mathrm{x}'|}}{|\mathbf{x}-\mathbf{x}'|^2} \qquad \textbf{2.20}$$

Where the propagation operator, $\hat{S}_r$ represents the propagation effects on sound radiation over a distance r. For a linear, absorptive propagation medium, it is defined as:

$$\hat{S}_r I(t) = \mathrm{e}^{-\alpha r} S_r I(t) = \mathrm{e}^{-\alpha r} I\left(t - \frac{r}{c}\right) \qquad \textbf{2.21}$$

Where c is the speed of sound in air and α is the absorption coefficient of air in Nepers per metre. Since the outgoing time dependent radiance at any point is a combination of the reflected time-dependent radiance and the emitted time dependent radiance, the acoustic radiance propagation in an enclosure can be written in the form of a RARE presented in eq. 2.15.

The radiosity method is derived from the RARE by using the following diffuse reflectance function in place of the BRDF $\rho(\mathbf{x}', \Theta, \Omega)$ in eq. 2.16 [12]:

$$\rho_{diff}(x) = \beta(x)/\pi \qquad \textbf{2.22}$$

Where β is the reflectivity coefficient of the material at a point x. This simplifies the RARE by omitting the directional dependence.

Discretizing the geometry into patches transforms the RARE into a matrix-based formulation which can be run marching on in reflection order. The ART algorithm is solved with a time-iterative approach with the following steps which follow a progressive radiance transfer model influenced by the progressive Radiosity solution. This is also illustrated in Figure 2.13.

1. The energy radiated by the source into the room is distributed among the boundary elements. In this case, the differential-to-finite-area form factor is accurate if the sources are assumed to be point-like. Sound source directivity can be taken into account at this stage by weighting the outgoing energy flow according to the sound source directivity pattern
2. The energy is further exchanged between elements always choosing the element with the highest unpropagated energy and distributing that energy to all other visible elements
3. Propagation time and energy responses are computed and stored for each outgoing direction for all elements
4. Steps 2 and 3 are repeated until the reflected energy at boundaries fall below a set threshold
5. Multiple receiver responses can now be computed without repeating any of the previous steps

Figure 2.13 Progressive ART solution (a) Before initial energy shooting (b) After initial shooting (c) Element with highest energy transfers it to other elements (d) The previous step is repeated for the new element with the highest energy (e) After a few reflection orders (f) Solution convergence and receiver response [13]

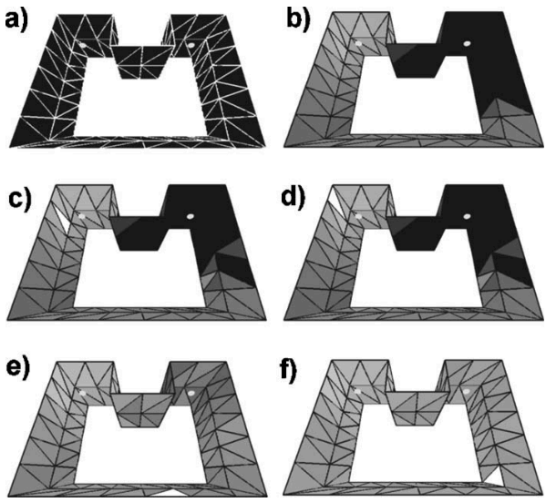

The Neumann series solution to the room acoustic rendering equation can be written as:

$$L_{n+1}(\mathbf{x}', \Omega) = \oint_{\mathcal{G}} R(\mathbf{x}, \mathbf{x}', \Omega) L_n(\mathbf{x}, \Gamma) d\mathbf{x}$$

$$L(\mathbf{x}', \Omega) = \sum_{n=0}^{\infty} L_n(\mathbf{x}', \Omega) \qquad \textbf{2.23}$$

This is a reflection-iterative (marching on in reflection order) solution to the room acoustic rendering equation. With the surface of the geometry divided into N elements, the Neumann series terms are presented as a sum of integrals over the elements:

$$L_{n+1}(\mathbf{x}', \Omega) = \sum_{i=0}^{N} \int_{A_i} R(\mathbf{x}, \mathbf{x}', \Omega) L_n(\mathbf{x}, \Gamma) d\mathbf{x} \qquad \textbf{2.24}$$

The LHS of the equation is then replaced by the average reflected radiance:

$$L_{n,j}(\Omega) = \frac{1}{A_j} \int_{A_j} L_n(\mathbf{x}', \Gamma) d\mathbf{x}' \qquad \textbf{2.25}$$

This is equivalent to solving the scheme in a Galerkin framework with PWC spatial testing functions. Applying the same PWC basis functions to spatial discretisation of $L_n(\mathbf{x}, \Gamma)$ yields an approximation where the radiation is assumed invariant over an element:

$$L_{n+1,j}(\Omega) = \frac{1}{A_j}\sum_{i=1}^{N}\int_{A_j}\int_{A_i} R(\mathbf{x}, \mathbf{x}', \Omega)L_{n,i}(-\Omega)d\mathbf{x}d\mathbf{x}' \qquad \textbf{2.26}$$

Here $\mathbf{x}'$ is on element i and $\mathbf{x}$ is on element j. The direction is discretized into directional segments over which radiation is assumed constant; a PWC discretisation in solid angle:

$$L_{n,k,j} = \frac{1}{\int_{\phi_k} d\phi}\int_{\phi_k} L_{n,j}\, d\Omega \qquad \textbf{2.27}$$

Here ϕ_k is the solid angle covered by the directional segment k. Then, an approximation where the radiation does not change over direction is given by:

$$L_{n+1,k,j} = \frac{1}{A_j \int_{\phi_k} d\phi}\sum_{i=1}^{n}\int_{\phi_k}\int_{A_j}\int_{A_i} R(\mathbf{x}, \mathbf{x}', \Omega_\mathrm{e})L_{n,i,\Gamma_i(-\Omega_e)}d\mathbf{x}\, d\mathbf{x}'\, d\Omega_\mathrm{e} \qquad \textbf{2.28}$$

Writing the reflection kernel in its discretized form,

$$R_{i,j,k} = \frac{\int_{\phi_k}\int_{A_j}\int_{A_i} R(\mathbf{x}, \mathbf{x}', \Omega_\mathrm{e})d\mathbf{x}\, d\mathbf{x}'\, d\Omega_\mathrm{e}}{A_j \int_{\phi_k} d\phi} \qquad \textbf{2.29}$$

Now, eq. 2.28 can be written as:

$$L_{n+1,k,j} = \sum_{i=1}^{\infty}\sum_{l\in\Psi} R_{i,j,k}L_{n,i,l} \qquad \textbf{2.30}$$

Where the indices l are a set of directional segments produced by the Γ_i operator over boundary integrals. The iterative solution is now given by:

$$L_{j,k} = L_{0,j,k} + \sum_{n=0}^{\infty} \sum_{i=1}^{N} \sum_{l \in \Psi} R_{i,j,k} L_{n,i,l} \qquad \textbf{2.31}$$

$L_{0,j,k}$ computes the radiance propagation from the source directly to the elements. Propagation is advanced in a time iterative manner before the transferred radiance falls below a set threshold. Now, $L_{j,k}$ can be computed directly, propagating energy from all elements to the receiver.

Comparing this formulation to the one that will be proposed in the following chapter, a similar structure emerges, albeit one that has PWC interpolation and testing functions hard coded into it. Notably, the denominator terms in eq. 2.28 and eq. 2.29 analytically calculate the mass matrix equivalent in space and angle, in 3D. This is possibly because the orthogonality of the PWC basis functions over the mesh make the mass matrix diagonal. This operator is PWC over elements and since the integration is a linear operator, boundary integrals are reduced to sum of constant values over boundary segments where the integrand is constant.

The group also proposed a frequency domain version if ART, that computed solutions based on a time-harmonic assumption. Siltanen, Lokki and Savioja also provide [40] alternative frameworks for parallel implementation of ART suited for the frequency domain formulation. The improvement in computational speed was found to be proportional to the number of parallel threads used. Siltanen and Loki [39] further proposed modifications to RARE so that it can include diffraction. A paper outlining an approach for embedding the Biot-Tolstoy model of diffraction in ART was presented by the group in [39], but results for a full implementation were not included.

2.2.3 The Nottingham Group

Dynamical Energy Analysis (DEA) was proposed by Tanner [14] in 2009. It is capable of computing flow of wave energy distributions in complex built-up structures. DEA interpolates between Statistical Energy Analysis (SEA) and Raytracing to compute mechanical or acoustic energy densities for high frequencies. It does this by expressing the ray dynamics in terms of linear boundary operators, which are in turn represented as a collection of basis functions on a boundary. SEA represents the solution in each subsystem of the structure as a scalar value

representing the mean ray density while DEA includes dynamical correlations and represents the solution as a vector – considering direction.

The number of boundary functions considered dictates the directional resolution of the dynamics. The maximum number of basis functions needed to reach convergence is expected to be small, making DEA more efficient than Raytracing, especially in the small damping regime. Some of the inefficiencies inherent in the common Raytracing formulations are circumvented by using limited geometric ray information in a DEA model. Benefiting from the SEA ansatz and by retaining information on the underpinning ray dynamics as necessary, DEA successfully extends the range of applicability of standard SEA, providing quantitative error bounds for SEA analyses. DEA models a classical Hamiltonian system describing ray trajectories in phase-space $X = (\mathbf{r}, \mathbf{p})$ where $\mathbf{r}$ is the position co-ordinate and $\mathbf{p}$ is the direction vector, which they refer to as 'momentum'. Phase space densities are propagated along ray trajectories using the Frobenius-Perron (FP) operator $\mathcal{L}^{\tau}$. This linear operator describes how an energy density f varies over time τ along the solution ray trajectories of a dynamical system defined by a vector field $\mathbf{V}$ as:

$$\dot{X} = \mathbf{V}(X) \tag{2.32}$$

The solution of this equation defines solution ray trajectories in phase-space of the form:

$$X(\tau) = \varphi^{\tau}(X(0)) \tag{2.33}$$

Where φ^{τ} is the associated continuous time flow map. This map encapsulates the Raytracing process. It describes how a ray leaving a certain point on the boundary in a certain direction arrives at another point on the boundary with a specific direction. Phase-space energy densities are propagated though a domain using the FP operator given by:

$$\mathcal{L}^{\tau}[f](X) = \int \delta(X - \varphi^{\tau}(Y)) f(Y, 0) dY \tag{2.34}$$

Replacing φ^{τ} with a discrete boundary map $\varphi_{i,j}$ – i.e., by introducing a discretisation scheme for ray position and angle distributions on the boundary – modifies the FP operator to a local boundary integral operator B_j. DEA uses a modified version of the FP operator where the flow is replaced by a boundary to boundary discrete map, as opposed to continuous time-dependent

flow. This operator maps the energy density flow from the phase-space on a boundary Γ_j to a different boundary Γ_i as:

$$B_j[f](X_i) = \int e^{-\mu_j D(X_i,Y_i)} w_{i,j}(Y_j)\delta\left(X_i - \varphi_{i,j}(Y_j)\right) f(Y_j) dY_j \qquad \textbf{2.35}$$

The weighting term $w_{i,j}$ is used to model angle dependent boundary absorption. The stationary steady-state boundary density can be obtained with a Neumann series:

$$\rho = \sum_{n=0}^{\infty} B^n[\rho_0] = (I - B)^{-1}[\rho_0] \qquad \textbf{2.36}$$

Where n is the number of iterations and ρ_0 is the initial boundary density.

Chappell and Tanner developed a boundary element formulation for DEA [15]. This BIE formulation involved solving the Liouville equation using the FP operator. The linear wave equation and the Liouville equation are linked using the Eikonal equation. The formulation is developed with time dependence and then the steady state solution is derived. A numerical solution was obtained with Legendre polynomials as basis in phase-space and spatially discretized on a boundary element mesh. Boundary properties are set by eq. 19 in [15] and specular reflections modelled with Snell's law of reflection from optics.

The paper cites Raytracing as more cumbersome when computing a steady state solution as each reflection from the boundary has to be accounted for. But phase space densities can be obtained from the FP operator if propagation phase is ignored. This is similar to Raytracing algorithms. The BIE formulation in this paper aims to overcome these limitations by developing an algorithm to efficiently compute the solutions of the stationary Liouville equation. This is obtained by rewriting the Raytracing equation as a BIE. This realized with a boundary mapping technique mapping ray densities from a point source onto the boundary and then formulating a FP operator for the boundary mapping scheme.

Recently, this group proposed a DEA method based on a Petrov-Galerkin Scheme [17]. This formulation discretises direction with a set of Dirac delta functions as basis. The finite set of directions at the boundary is assumed as a subset of a global set and the directional information is retained when solving energy density propagating through multi-domains. Energy density can then be described with a ray propagation with the same global direction in different

domains. This emphasises similarities with volumetric mesh methods such as FEM. This formulation was verified against ISM. This method is similar to the "ray direction quantisation" process discussed by Pohl [41].

This group has also developed a formulation operating on a volumetric mesh similar to FEM where the entire domain along with the boundaries are meshed [42]. This is a unique feature of the Nottingham group's approach and opens up exciting opportunities in modelling problems in structure-borne and inhomogeneous media. As the formulation is restricted to tetrahedral elements which are always convex by nature allows in-depth analysis on integration efficiency and accuracy that cannot be replicated by a boundary to boundary scheme due to shadowing by other sections of the boundary.

2.3 CONCLUSIONS

EBEM has been formulated so that it adopts attractive features from the SB-GA models discussed in this chapter. The SB-GA models in this chapter discretise only the incoming or outgoing energy and included a mechanism to relate the incoming and reflected outgoing energies. EBEM on the other hand discretises incoming and outgoing energy separately. This is similar to high frequency BEM [19] and EBEM aims to emphasise its synergy with SB-GA.

The Galerkin framework adopted for mapping power onto the boundaries in EBEM expediates the comparison of different basis and testing functions. This is different to the collocation scheme by the Duke Group [10]. EBEM is implemented so that the factors required to compensate for these are moved outside the main solution part of the code, where they would have to be hard-coded, into a matrix multiplication. Stacking the Fourier coefficients describing directional sources and receivers into vectors means that all wave propagation operators can be described by matrix multiplications in EBEM.

3 THEORY & FORMULATION

This chapter describes the theoretical framework for the EBEM formulation. First the assumed model of acoustic power propagation is presented. This is followed by the boundary integral representations for various propagation and mapping processes required to operate the EBEM algorithm, with structure for solving the discretised form of the EBEM model presented at the end of the chapter.

3.1 FUNDAMENTALS OF ROOM ACOUSTICS

Room Acoustics models study how sound is propagated and reflected within an enclosed space and how it is perceived by a listener in the space. The basic equations are presented, along with source, propagation and boundary interaction processes are discussed.

3.1.1 Basic equations

The Acoustic wave equation is a PDE derived from the mass conservation and inertia laws in a fluid media. It is stated as:

$$\Delta p = \frac{1}{c^2} \cdot \frac{\partial^2 p}{\partial t^2} \qquad \textbf{3.1}$$

Where c is the speed of sound in metres per second and Δp is the Laplace operator in Cartesian co-ordinates, given in three dimensions by:

$$\Delta p = \frac{\partial^2 p}{\partial x^2} + \frac{\partial^2 p}{\partial y^2} + \frac{\partial^2 p}{\partial z^2} \quad \textbf{3.2}$$

3.1.2 Propagation of sound

Mathematically, the sound propagation in an enclosed space is described using the wave equation. However, this PDE can only be solved analytically in certain idealised cases [43] and we hence require all existing and applied formulations to model sound fields in enclosed spaces. Sound propagation in air can be described by Huygen's principle which establishes that a wave front progresses in a certain space if each of the points on the wave front radiates spherical waves themselves. These individual waves sum up to the total wave front at an advanced time.

3.1.3 Boundary reflection and absorption

In homogenous media such as air, sound waves travel unobstructed in all possible directions from a source until the wavefronts are obstructed with a change in medium density. This arises at the boundaries of rooms where the boundary density is far greater than density of air. On incidence at the boundary, if the surface is perfectly smooth, the ray is reflected specularly, with the incident and reflection angles w.r.t. to the surface normal being equal.

Depending on the boundary material properties, only a portion of energy incident on the boundary is reflected back into the room. The residual fraction not reflected back into the room is absorbed or transmitted at the boundary, the former resulting from internal acoustic energy dissipation processes. Reflection processes produce a change in energy amplitude as well as propagation phase, if considered.

On incidence on the boundary, it is assumed that the absorbed or transmitted fraction has no effect on the reflected wave or the sound field in the room. As such, the amplitude of the reflected wave is reduced by a factor R which is the reflection coefficient. By examining pressure and velocity of the incident wave, we can define the boundary surface impedance Z_B in terms of R:

$$Z_B = \rho_0 c \frac{1+R}{1-R} \quad \textbf{3.3}$$

Where ρ_0 is the density of air in kg/m^3. This equation leads to a relationship between R and normalised impedance of the boundary $\varsigma = Z_B/\rho_0 c$:

$$R = \frac{\varsigma - 1}{\varsigma + 1} \quad \textbf{3.4}$$

For realistic situations, R is bounded by $-1 < R < 1$ so that energy is always conserved or absorbed at boundaries and never increased. Considering a spatial degree in eq. 3.4, R for oblique incidence and in terms of normalised boundary admittance $Y_n = 1/\varsigma$ is defined by:

$$R_\theta = \frac{\cos\theta - Y_n}{\cos\theta + Y_n} \quad \textbf{3.5}$$

The angle dependent reflection factor computed with a normalised boundary admittance $Y_n = Y/\rho_0 c_0$. The Absorption coefficient α relates the intensity of incident and reflected waves rather than amplitude. Intensity of a sound wave in air is given by:

$$I = \frac{p^2}{\rho_0 c} \quad \textbf{3.6}$$

For pressure p. Sound intensity has units of power density and is proportional to squared pressure amplitude. Intensity is a vector and points in the direction of power flow. Therefore, intensity of the reflected wave will be attenuated by a factor of $|R|^2$, giving the following equation for the angle-based absorption coefficient:

$$\alpha_\theta = 1 - |R_\theta|^2 \quad \textbf{3.7}$$

This will have a value of 0 for rigid non-absorbent boundaries.

In acoustics, the medium of transmission is air, which attenuates sound energy propagating through it. The degree of attenuation depends on several factors including wave frequency, temperature, humidity, and atmospheric pressure. But in rooms the effect of this is typically quite small, hence in this thesis air absorption is ignored for simplicity.

3.1.4 Diffuse reflections

Ideal specular reflections following Snell's law are valid only for infinite smooth plane surfaces. For real surfaces which are finite and irregular, sound is scattered on incidence. The effect of the *smoothness* of a boundary surface on the impeding wave is a function of incident wavelength. If the dimensional variations of the boundary are small compared to incident wavelength, they are specularly reflected. This results in low frequencies with large wavelengths being specularly reflected from most surfaces. When surface irregularities are of similar order of magnitude as the wavelength, the incident wave, irrespective of incident direction, is reflected/scattered in all directions – called diffuse reflection. This is illustrated in Figure 3.1. At the highest frequencies, where wavelength is small compared to boundary features, redirection can occur.

Figure 3.1 Frequency ranges for scattering from a periodic surface of repeat distance a, and roughness depth h [44]

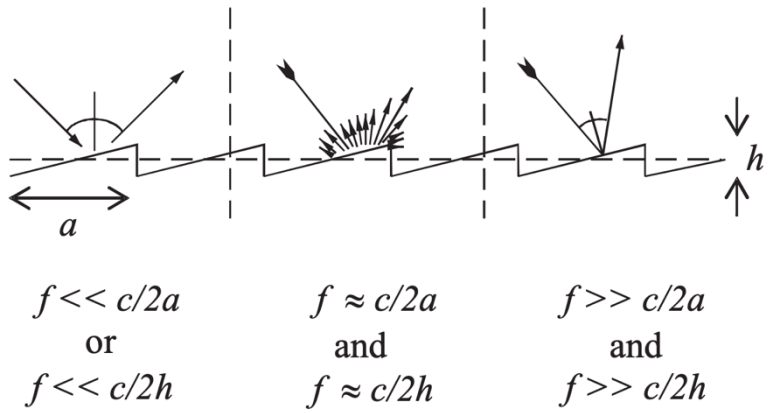

3.1.5 Sources of sound

A sound field, in an enclosed space or otherwise can be excited by different kinds of sound sources. This section presents typical acoustic sources pertinent to derivation of a source model for EBEM discussed later in this chapter.

3.1.5.1 Point sources

Typical situations in room acoustics comprise of sound sources which are directional, such as vocal speakers or musical instruments or loudspeakers. These sources possess some volume, but computational modelling applications, they can be generalised to point sources [20].

Often it might be assumed that sources are omnidirectional, that is, lacking any directional characteristics. This assumption leads to the sound power being constant over the surface of a sphere centred on the point source. The magnitude of the sound intensity will then also be constant over the surface of the sphere and, since the total sound power is represented by the intensity over the entire surface area of the sphere, it follows that intensity will point outward in the direction of increasing r and have magnitude:

$$I = \frac{W}{4\pi r^2} \qquad \textbf{3.8}$$

Here W is the sound power of the point source in Watts.

Figure 3.2 Wavefront from a point source

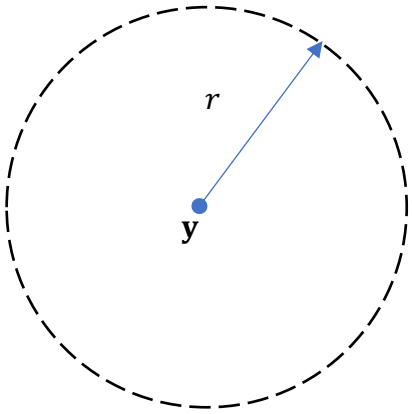

3.1.5.2 Line sources

A line source is essentially a distribution of an infinite number of point sources on an imaginary line. This thesis limits the study to sources that are coherent and identically valued. The radial power radiated by a line source and the intensity will be constant on the lateral surface of a cylindrical surface as shown:

Figure 3.3 Wavefront from a line source

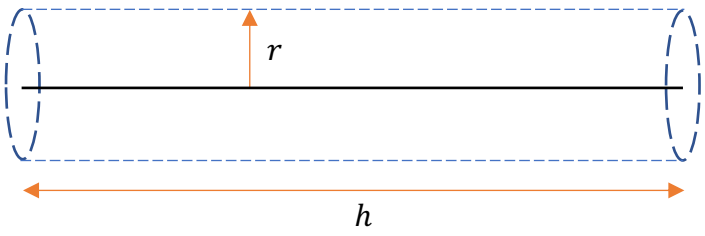

Intensity over the surface of the cylinder gives the total outputted sound power P, defined as:

$$P = \frac{W}{2\pi rh} \quad \textbf{3.9}$$

P has units of Watts per metre squared. For infinitely long line sources, we define sound power per unit length W':

$$I = \frac{W'}{2\pi r} \quad \textbf{3.10}$$

To reduce the complexity of EBEM, the scope of development in this thesis is restricted to 2D. We only consider a 2D cross section of a 3D geometry, invariant in the third dimension. Now, infinitely long line sources in 3D can be assumed to be point sources in 2D as shown in Figure 3.4.

Figure 3.4 Simplification of an (a) infinitely long line source in 3D to a (b) point source in 2D

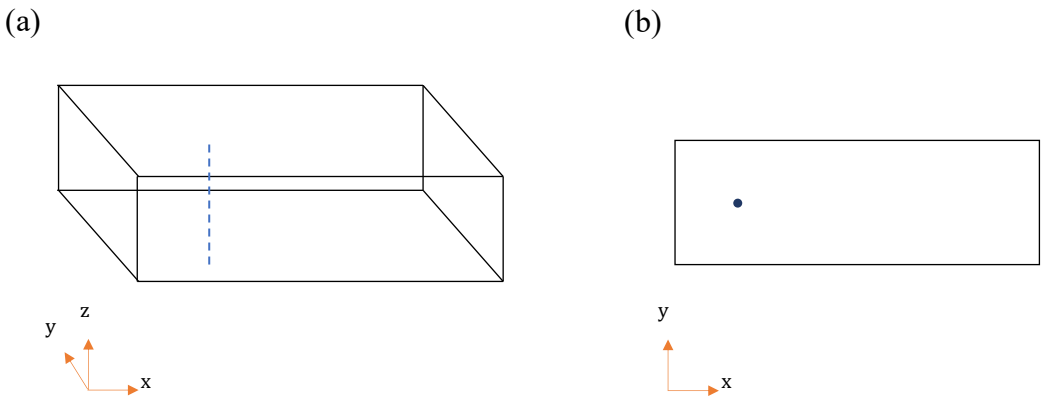

3.1.6 Energy response

An impulse response of a room is its time domain response to an idealised Dirac delta input. It describes the temporal distribution of reflections in a room. This characterises all propagation paths from a source to a receiver in a room, direct and reflected. Each response at a receiver point will vary for each frequency simulated and we obtain a similar energy response when

propagation phase is ignored. Direct sound from the source to the receiver, i.e., on the shortest path from the source to the receiver, will register the first detection, followed by sparse early reflections and late-time diffuse sound field with high reflection density. These weaker reflections at late-time merge together into what is subjectively perceived as reverberation.

Figure 3.5 Schematic of an energy response of a room: x-axis represents time and y-axis represents its energy level w.r.t direct sound at t=0 [4]

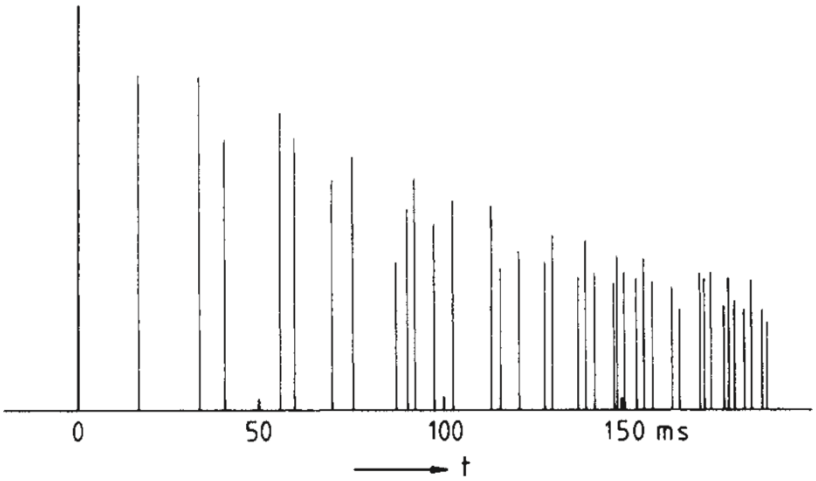

The energy provides a wealth of information on the acoustic qualities of the space under investigation, including computation of objective parameters and decay of energy in the room. Early reflections will differ significantly with source and/or receiver positions in a room. These are of outmost perceptual importance as they provide auditory cues describing size of the space for source localisation [38]. At late-time, the sound field is said to be diffuse, with the energy arriving at the receiver rapidly from a multitude of directions – and the direction or arrival will be irrelevant. Such sound fields are considered perceptually constant in a domain under study. These diffuse sound field components will decay exponentially with time, resulting in a reverberation tail.

3.2 ASSUMED MODEL OF ACOUSTIC PROPAGATION

EBEM is formulated as an energy-based method initially developed in 2D in this chapter. The Duke Group similarly discretise power density as well for their EIBEM model [10] discussed in Chapter 2. Acoustic propagation for EBEM is modelled with by a particle tracing problem. Particles travelling geometrically i.e., in straight lines are termed rays. Each individual particle will have position $\mathbf{x}$ and propagation direction $\hat{\mathbf{k}}$. The power distribution

$w(\mathbf{x}, \hat{\mathbf{k}})$ of these particles is hence a function of both position and direction. This would mean that we are working strictly in the high-frequency regime.

The second important assumption we make is to ignore propagation phase. Consideration is given to only energy and power when computing the solution, albeit including the direction of propagation. This assumption aligns with the classical Raytracing formulation and is justified by the chaotic nature of the sound field in the late-time interval in room acoustics [45]. Lack of phase information also means that interference effects cannot be modelled – this is typical of GA methods used for modelling high frequency room acoustics. We also ignore air absorption for simplicity, as already stated.

3.2.1 Angular conventions

As we are developing the EBEM formulation in 2D, position at a point $\mathbf{x}$ will vary in two dimensions and the direction vector $\hat{\mathbf{k}}$ can take a value in the range $0° \leq \hat{\mathbf{k}} \leq 360°$. Hence, $\hat{\mathbf{k}}$ can be defined as:

$$\hat{\mathbf{k}} = [\cos\theta \quad \sin\theta] \tag{3.11}$$

On the boundary, which is one dimensional (a line) when working in 2D, position $\mathbf{x}$ can be parametrised in terms of the distance from a reference point. $\mathbf{x}$ is therefore a function of only boundary position. This will be a scalar with units of metres. Incoming and outgoing directions of rays on the boundary are constrained within a $180°$ range as shown in Figure 3.6:

Figure 3.6 Geometry to illustrate incoming and outgoing directions on the boundary constrained to a 180° range

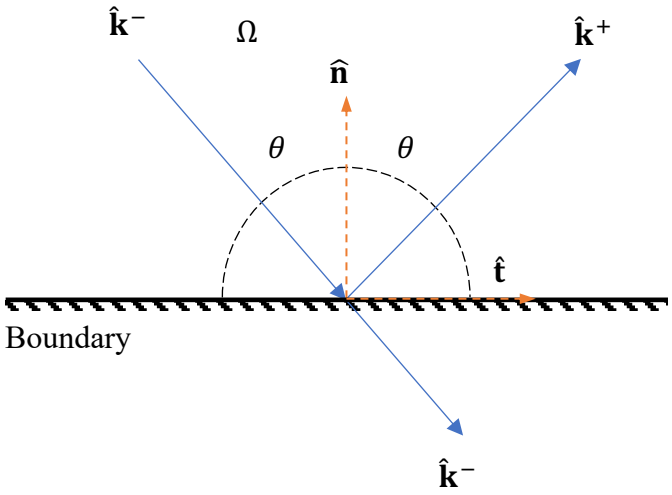

In EBEM, we distinguish between these incoming and outgoing directions denoted by $\hat{\mathbf{k}}^-$ and $\hat{\mathbf{k}}^+$ respectively. We specify the orientation of the boundary at a point $\mathbf{x}$ by its normal $\hat{\mathbf{n}}$ and tangent vectors $\hat{\mathbf{t}}$, which are perpendicular to each other. $\hat{\mathbf{n}}$ is taken to point into the solution domain Ω. For incoming directions, $\hat{\mathbf{n}} \cdot \hat{\mathbf{k}} < 0$ and for outgoing directions, the relation is $\hat{\mathbf{n}} \cdot \hat{\mathbf{k}} > 0$.

The next step is to devise a scheme to parametrise these directions on the boundary. This can be achieved in in two different ways:

1) Using an angle θ defined in the boundary-local co-ordinate system defined by the normal and tangential vectors. This is shown in Figure 3.7 below. The incoming and outgoing directions in terms of are θ defined as:

$$\hat{\mathbf{k}}^+(\theta) = \hat{\mathbf{t}}_n \sin\theta + \hat{\mathbf{n}}_n \cos\theta$$
$$\hat{\mathbf{k}}^-(\theta) = \hat{\mathbf{t}}_n \sin\theta - \hat{\mathbf{n}}_n \cos\theta \qquad \textbf{3.12}$$

2) Using a dimensionless boundary tangential co-ordinate χ defined by $\chi = \sin\theta$. This is similar to how the Nottingham Group [15] define their incoming and outgoing directions, albeit encapsulated within their 'momentum' parameter. Incoming and outgoing directions in this case are defined as:

$$\hat{\mathbf{k}}^+(\chi) = \hat{\mathbf{t}}_n \chi + \hat{\mathbf{n}}_n \sqrt{1-\chi^2} \qquad \textbf{3.13}$$

$$\hat{\mathbf{k}}^{-}(\chi) = \hat{\mathbf{t}}_n \chi - \hat{\mathbf{n}}_n \sqrt{1-\chi^2}$$

These two methods of parametrising direction on the boundary are shown in Figure 3.7 below:

Figure 3.7 Illustrating incoming and outgoing ray directions on the boundary

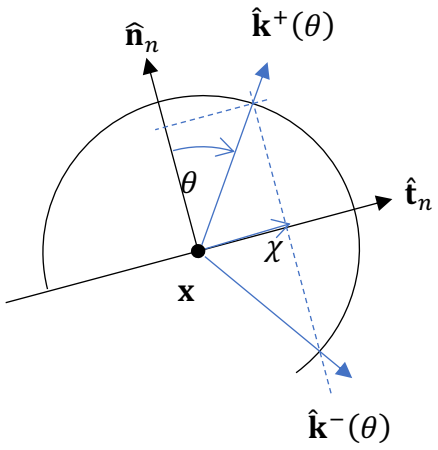

To convert between integrals w.r.t. θ and χ, the following relationship can be exploited:

$$\int_{-\pi/2}^{\pi/2} \ldots \frac{d\chi}{d\theta} d\theta \equiv \int_{-1}^{1} \ldots \, d\chi \qquad \textbf{3.14}$$

Where $\frac{d\chi}{d\theta}$ is the Jacobian. As $\chi = \sin\theta$, we get:

$$\frac{d\chi}{d\theta} = \cos\theta = \sqrt{1-\chi^2} \qquad \textbf{3.15}$$

θ and χ will be used interchangeably used this thesis based on their definitions in this chapter. θ is usually used to check if propagation or reflection angles match and χ is used for evaluating angular integrals numerically. $\hat{\mathbf{k}}$ is used to ease the various definitions by avoiding the requirement to align local co-ordinates.

3.3 ALGORITHM STRUCTURE

The EBEM algorithm structure is presented in this section. The various integral terms used in this section will be derived in following sections in this chapter. The discretised version of the EBEM algorithm is solved as follows:

1) First the directional power from the source $\mathbf{w}_\mathrm{s}$ is mapped onto the boundary as an incoming power distribution $w^-(\mathbf{x}, \hat{\mathbf{k}}^-)$, represented by $\mathbf{w}_0^-$.
2) This distribution is reflected at the boundary to produce an outgoing power distribution $w^+(\mathbf{x}, \hat{\mathbf{k}}^+)$, represented by $\mathbf{w}_0^+$.
3) This outgoing power distribution arrives at a different part on the boundary and is again mapped as an incoming power distribution $w^-(\mathbf{x}, \hat{\mathbf{k}}^-)$, represented by $\mathbf{w}_1^-$
4) The next step in the algorithm can be implemented in two ways:
    a. Steps 2 and 3 are repeated up to the specified number of reflection orders to simulate boundary reflections. All the $\mathbf{w}_i^-$ are summed with respect to reflection order i to obtain the boundary distributions
    b. The total steady-state power distribution can me computed using a Neumann series.
5) Power distribution at the receivers is computed, represented by $\mathbf{w}_\mathrm{r}$. This is sum of the direct power from sources in the domain (represented by their $\mathbf{w}_\mathrm{s}$) and power arriving from the boundary (represented by $\sum_i \mathbf{w}_i^+$).

Each mapping is represented by a matrix multiplication. The algorithm described above can be summarised as:

$$\mathbf{w}_i^- = \begin{cases} \mathbf{M}^{-1}\mathbf{T}_\mathrm{sb}\mathbf{w}_\mathrm{s} & \text{for } i = 0 \\ \mathbf{M}^{-1}\mathbf{T}_\mathrm{bb}\mathbf{w}_{i-1}^+ & \text{for } i > 0 \end{cases}, \quad \mathbf{w}_i^+ = \mathbf{M}^{-1}\mathbf{R}\mathbf{w}_i^-. \tag{3.16}$$

Where:

$\mathbf{T}_\mathrm{sb}$ is the matrix describing source-to-boundary propagation

$\mathbf{T}_\mathrm{bb}$ is the matrix describing boundary-to-boundary propagation

M is the mass (or identity) matrix

R is the Reflectance matrix describing boundary absorption and scattering

Total power distribution at a receiver is given by:

$$\mathbf{w}_r = \mathbf{T}_{sr}\mathbf{w}_s + \mathbf{T}_{br}\sum_i \mathbf{w}_i^+ \qquad 3.17$$

Where:

$\mathbf{T}_{sr}$ is the source-to-receiver propagation matrix

$\mathbf{T}_{br}$ is the boundary-to-receiver propagation matrix

The form in eq. 3.17 amounts to solution by marching on in reflection order. Although standard BEM algorithms are not usually solved in this way, the BEM formulation in eq. 32 and 41 in [19] uses it, and the time-domain version of BEM is often solved in a similar way [48].

3.4 POWER INCIDENT FROM A POINT SOURCE

The first step in developing a complete acoustic transmission path for the EBEM formulation will be to define a source model. This would be used along with the solution domain enclosed by the boundary, and a receiver placed in said domain to completely model the acoustic transmission in a room. This section defines a point source and its physical description. Consider power radiating from a point source located at $\mathbf{y_0}$ in the solution domain as shown in Figure 3.8:

Figure 3.8 Illustration of power radiating from a point source located at $\mathbf{y_0}$ and measurement of the source angle $\theta_s$with respect to a reception point x. $\widehat{\mathbf{R}}$ is the unit ray vector in the direction of propagation from $\mathbf{y_0}$ to x

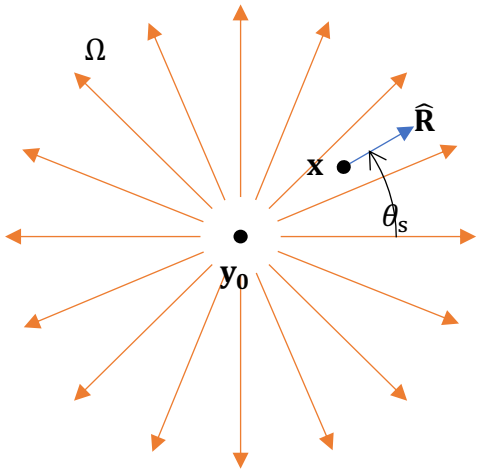

The source injects power W into the domain. As a 2D point source is equivalent to a cylindrical line source in 3D as explained in Section 3.1.5, the units of W is Watts per metre. Real line sources in 2D will have nearfield effects which are ignored as one of the starting assumptions when deriving the EBEM formulation in the high frequency regime. At a point $\mathbf{x}$, which can be an arbitrary point in the domain or on the boundary, the received power density accounting for cylindrical spreading of power is given by:

$$W_{\mathrm{x}} = \frac{W}{2\pi R} \qquad \textbf{3.18}$$

Where:

$\mathbf{R}$ is the ray vector from $\mathbf{y_0}$ to $\mathbf{x}$ defined as $\mathbf{R} = \mathbf{y_0} - \mathbf{x}$

R is the length of the ray from $\mathbf{y_0}$ to $\mathbf{x}$ in metres, computed as $R = |\mathbf{R}|$

The units of the power density received at $\mathbf{x}$ is Watts per metre^2 where the metre^2 area term is tangential to the wavefront propagating from the source. The intensity received at this point will be the power density multiplied by the unit propagation direction vector $\widehat{\mathbf{R}} = \mathbf{R}/R$ and is hence defined as:

$$\mathbf{I}_{\mathrm{x}} = \widehat{\mathbf{R}} \frac{W}{2\pi R} \qquad \textbf{3.19}$$

3.4.1 Source directionality

Standardised metrics to analyse room acoustic conditions have traditionally been derived from measurements with omnidirectional loudspeakers. This has since been adopted with computer simulations for room acoustics to derive similar objective parameters from room acoustic simulation outputs. But typical sources in a room such as vocal speakers or musical instruments or even commonly used loudspeakers have directivity characteristics and are rarely omnidirectional. Furthermore, for the purpose of auralisation of real sources, inclusion of directional properties of sources is important [7].

One of the features of the EBEM formulation presented in this thesis is its ability to include directional sources. If we consider the point source to be directional and the power injected into the domain varies with angle θ_{s}, power injected by the source into the room is replaced by a directivity function $W_{\mathrm{s}}(\theta_{\mathrm{s}})$ whose integral from 0 to 2π w.r.t. θ_{s} equals W:

$$\int_0^{2\pi} W_s(\theta_s) d\theta_s = W \tag{3.20}$$

Note that θ_s is defined in the global sense relative to the Cartesian axes because the source lies in the domain and not on the boundary. $W_s(\theta_s)$ has units of Watts per metre per radian. For an omnidirectional source, the following equation is obtained:

$$W_s(\theta_s) = \frac{W}{2\pi} \tag{3.21}$$

The equation for power density received at **x** is now:

$$W_{\mathbf{x}} = \frac{W_s(\theta_s)}{R} \tag{3.22}$$

The 2π term is removed from this equation because of the units of $W_s(\theta_s)$. Received intensity at **x** is:

$$\mathbf{I} = \hat{\mathbf{R}} \frac{W_s(\theta_s)}{R} \tag{3.23}$$

The directional power distribution $w(\mathbf{x}, \hat{\mathbf{k}}) \equiv w(\mathbf{x}, \theta_r)$ is the acoustic quantity being propagated, and this needs to be formulated in terms of the power incident from a point source. At a receiver point, w has units of Watts per metre^2 per radian, with the "per radian" term is with respect to the receiver angle θ_r. The rays emanating from such a point source will be perfectly directional, and can be represented using a Kronecker delta function in angle $\delta(\theta_s - \theta_r)$ defined as:

$$\delta(\theta_s - \theta_r) = \begin{cases} 1, & \text{if } \theta_s = \theta_r \\ 0, & \text{otherwise} \end{cases} \tag{3.24}$$

Now the directional power distribution at **x** is given by:

$$w(\mathbf{x}, \hat{\mathbf{k}}) = w(\mathbf{x}, \theta_r) = \frac{W_s(\theta_s)}{R} \delta(\theta_s - \theta_r) = \frac{W_s(\theta_s)}{R} \delta\left(\cos^{-1}(\hat{\mathbf{k}} \cdot \hat{\mathbf{R}})\right) \tag{3.25}$$

The total power incident at a receiver irrespective of the arrival direction is given by:

$$W_{\mathrm{r}}(\mathbf{x}) = \oint w(\mathbf{x}, \hat{\mathbf{k}}) d\hat{\mathbf{k}} \equiv \int_0^{2\pi} \frac{W_{\mathrm{s}}(\theta_{\mathrm{s}})}{R} \delta(\theta_{\mathrm{s}} - \theta_{\mathrm{r}}) d\theta_{\mathrm{r}} = \frac{W_{\mathrm{s}}(\theta_{\mathrm{s}})}{R} \qquad \textbf{3.26}$$

W_{r} is the spatial power density with units of Watts per metre^2. Here the sifting property of the delta function is exploited to remove the integral. The delta function 'sifts' the direction $\hat{\mathbf{k}}$ for which $\theta_{\mathrm{s}} = \theta_{\mathrm{r}}$ which is equal to $\widehat{\mathbf{R}}$**.** This is a mathematical way of describing Raytracing and is shown in Figure 3.9:

Figure 3.9 The delta function adds a condition where direction $\hat{\mathbf{k}}$ has to be equal to $\widehat{\mathbf{R}}$

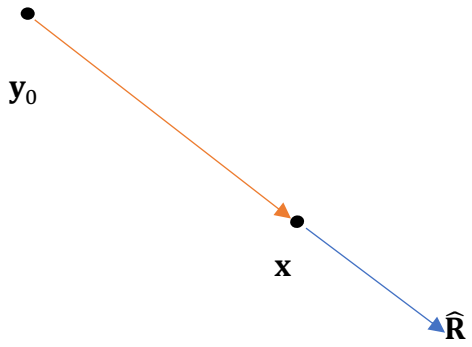

The received intensity at $\mathbf{x}$ can be computed with a similar integral:

$$\mathbf{I}(\mathbf{x}) = \oint w(\mathbf{x}, \hat{\mathbf{k}}) \hat{\mathbf{k}}\, d\hat{\mathbf{k}} \equiv \int_0^{2\pi} \frac{W_{\mathrm{s}}(\theta_{\mathrm{s}})}{R} \delta(\theta_{\mathrm{s}} - \theta_{\mathrm{r}})\, \hat{\mathbf{k}}(\theta_{\mathrm{r}}) d\theta_{\mathrm{r}} = \frac{W_{\mathrm{s}}(\theta_{\mathrm{s}})}{R} \widehat{\mathbf{R}} \qquad \textbf{3.27}$$

3.5 SOURCE TO BOUNDARY MAPPING

This section describes the process of mapping the directional power distribution radiating from a point source in the domain to an equivalent incoming power distribution based in the boundary co-ordinate system. The source radiates rays in all directions as explained previously and the boundary can accept rays arriving from the domain in any direction, but only the ones that align in both receiver position and angle are geometrically valid. This is the orange ray in Figure 3.10 and this aligned ray into the boundary (shown in blue in the same figure). This imposes an equivalence between θ_{s} and $\theta_{\mathbf{x}}$.

Figure 3.10 Geometry illustrating source to boundary mapping

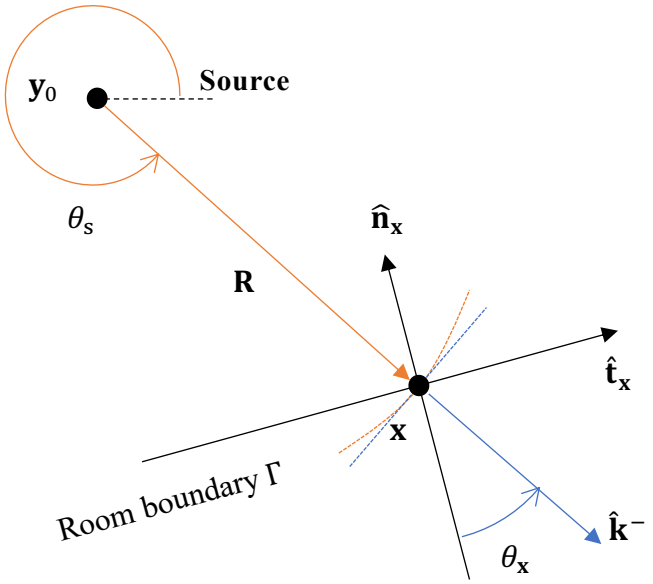

This is not immediately straightforward to mathematically state as θ_s is defined w.r.t. the global Cartesian x-axes and is defined θ_x w.r.t. the normal vector on the boundary. But this issue with comparison of definitions based on different reference directions is avoided by requiring that $\cos^{-1}(\hat{\mathbf{k}}^- \cdot \hat{\mathbf{R}}) = 0$, which is satisfied with the condition $\hat{\mathbf{k}}^- = \hat{\mathbf{R}}$. Hence, a boundary distribution with an angular term $\delta(\cos^{-1}(\hat{\mathbf{k}}^- \cdot \hat{\mathbf{R}}))$ will sift out a ray direction (blue arrow) matching the arrival direction from a point source in the domain (orange arrow). The incoming power distribution at the boundary is given by:

$$w^-(\mathbf{x}, \hat{\mathbf{k}}^-) = \frac{W_s(\theta_s)}{R} \delta(\cos^{-1}(\hat{\mathbf{k}}^- \cdot \hat{\mathbf{R}})) V(\mathbf{x}, \mathbf{y}_0) \qquad \textbf{3.28}$$

In addition to ensuring only geometrically valid ray are considered, two additional checks must be performed on the sifted ray:

1. A ray "visibility" check to ensure the ray path from the source to a boundary point is not occluded. A valid ray path with no obstructions will give such a term a value of 1, and 0 if the path is invalid or obstructed by another part of the boundary.
2. A ray "validity" check to ensure the ray arrives on the boundary from the enclosed interior domain and not the exterior side. This can be imposed with the condition $\hat{\mathbf{n}} \cdot \hat{\mathbf{R}} < 0$.

Both these checks are encapsulated into a single function $V(\mathbf{x}, \mathbf{y}_0)$ which takes the value 1 if the ray path is valid and unobstructed, and 0 otherwise. However, this is always 1 in a convex domain such as the rectangular room modelled in this study. Hence this function is not considered in detail in this thesis, since all the case studies chosen are convex.

3.6 INTERACTION WITH BOUNDARY MATERIAL

Before considering the outgoing power distribution reflected from the boundary back into the domain, interaction of the incoming distribution with the boundary material must be considered. A ray arriving at the interface of two media can be affected in various ways. When a ray is incident on the boundary, rays into both the interior and exterior domains exist. We assume that the exterior medium is locally reacting, so no rays from the exterior medium re-enter the interior domain. The local reaction model has been widely used in GA models and performs well in conjunction with GA models even when modelling porous absorbers which would deviate from a local reaction material.

The mapping between the incoming and outgoing distributions, $w^-(\mathbf{x}, \hat{\mathbf{k}}^-)$ and $w^+(\mathbf{x}, \hat{\mathbf{k}}^+)$ can be completely arbitrary if scattering is present – any location $\mathbf{x}$ and incoming direction $\hat{\mathbf{k}}^-$ in a distribution w^- could in principle influence any location $\mathbf{x}$ and outgoing direction $\hat{\mathbf{k}}^+$ in a distribution w^+. For locally reacting boundaries, the two locations $\mathbf{x}$ are the same boundary point and the relationship becomes a Bi-directional Reflectance Density Function (BRDF) denoted by $R(\mathbf{x}, \chi^+, \chi^-)$ and used as:

$$w^+(\mathbf{x}, \chi^+) = \int_{-1}^{+1} R(\mathbf{x}, \chi^+, \chi^-) w^-(\mathbf{x}, \chi^-) d\chi^- \qquad \textbf{3.29}$$

3.7 RE-RADIATION FROM BOUNDARY

Section 3.6 described how the power distribution incident at a point $\mathbf{y}$ on the boundary interacts with the boundary material before producing an outgoing power distribution back into the domain. Now this distribution has to be mapped as either:

1. The distribution $w^-(\mathbf{x}, \hat{\mathbf{k}})$ at a receiver located at point $\mathbf{x}$ in the domain, or
2. The incoming distribution $w^-(\mathbf{x}, \hat{\mathbf{k}}^-)$ at a point $\mathbf{x}$ at another part of the boundary

Figure 3.11 shows the geometry for evaluating these interactions. The orange ray depicts such an interaction from $\mathbf{y}$ to a point $\mathbf{x}$ both in the domain as well as another part of the boundary.

Figure 3.11 Geometry for evaluating boundary to boundary interactions

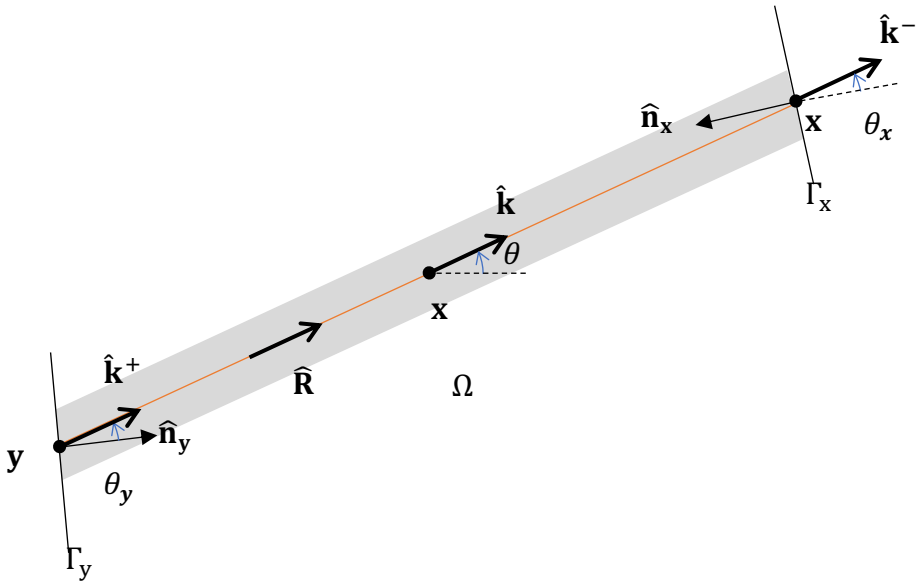

The direction vectors at both these points align with the orange ray as shown, and therefore we have:

$$\hat{\mathbf{k}} = \hat{\mathbf{k}}^+ = \hat{\mathbf{k}}^- = \hat{\mathbf{R}} \qquad \textbf{3.30}$$

But how this direction vector is parametrised as an angle varies:

- For at $\mathbf{y} \in \Gamma_y$ the angle $\theta_\mathbf{y}$ is relative to the normal vector $\hat{\mathbf{n}}_\mathbf{y}$ at $\mathbf{y}$
- For $\mathbf{x} \in \Omega$ the angle θ is relative to the global Cartesian x-axis
- For $\mathbf{x} \in \Gamma_\mathbf{x}$ the angle $\theta_\mathbf{x}$ is relative to the inverted normal vector $-\hat{\mathbf{n}}_\mathbf{x}$ at $\mathbf{x}$.

In all three cases, the units of w are Watts per metre squared per radian, where the "per metre squared" is taken in the plane perpendicular to the direction of propagation. The re-radiation statement will be developed for a domain receiver $w(\mathbf{x}, \hat{\mathbf{k}})$ but will also apply to a boundary point $w^-(\mathbf{x}, \hat{\mathbf{k}}^-)$.

All points on the boundary $\Gamma_\mathbf{y}$ could potentially radiate to a point $\mathbf{x} \in \Omega$, and the power density received will be the summation of their contributions. Because of this, an integral over

boundary position is present. The boundary can radiate in any angle too, hence there is also an integral over $\theta_{\mathbf{y}}$. $w(\mathbf{x}, \hat{\mathbf{k}})$ is therefore given by:

$$w(\mathbf{x}, \hat{\mathbf{k}}) = \int_{\Gamma} \int_{-\frac{\pi}{2}}^{\frac{\pi}{2}} \frac{w^{+}(\mathbf{y}, \hat{\mathbf{k}}^{+})}{R} \delta\left(\cos^{-1}(\hat{\mathbf{k}} \cdot \widehat{\mathbf{R}})\right) \delta\left(\cos^{-1}(\hat{\mathbf{k}}^{+} \cdot \widehat{\mathbf{R}})\right) \times V(\mathbf{x}, \mathbf{y}) \cos\theta_{\mathbf{y}} \, d\theta_{\mathbf{y}} d\Gamma_{\mathbf{y}} \qquad \textbf{3.31}$$

In this equation, $\mathbf{x}$ and $\hat{\mathbf{k}}$ are arguments. Hence, it can no-longer assumed that $\hat{\mathbf{k}}$ is aligned with $\widehat{\mathbf{R}}$, but it remains true that the ray arriving from $\mathbf{y}$ points in direction $\widehat{\mathbf{R}}$. The term $\delta\left(\cos^{-1}(\hat{\mathbf{k}} \cdot \widehat{\mathbf{R}})\right)$ in the integrand ensures this geometric validity. Similarly, $\hat{\mathbf{k}}^{+}$ is a function of the integration variable $\theta_{\mathbf{y}}$, but the geometric model of acoustic propagation means that only radiation from the boundary in the direction $\hat{\mathbf{k}}^{+} = \widehat{\mathbf{R}}$ contributes. The term $\delta\left(\cos^{-1}(\hat{\mathbf{k}}^{+} \cdot \widehat{\mathbf{R}})\right)$ ensures this.

The $1/R$ arises due to spherical spreading from the boundary sources. It converts the 'per radian' of $w^{+}(\mathbf{y}, \hat{\mathbf{k}}^{+})$ at $\mathbf{y}$ into a 'per metre' tangential to the wavefront at $\mathbf{x}$. One of the 'per metre' of $w^{+}(\mathbf{y}, \hat{\mathbf{k}}^{+})$ at $\mathbf{y}$ will be integrated out by the spatial integral over $\Gamma_{\mathbf{y}}$. But the 'per metre' of $w^{+}(\mathbf{y}, \hat{\mathbf{k}}^{+})$ is in the plane perpendicular to the direction of propagation, whereas the integral is w.r.t. boundary length. The $\cos\theta_{\mathbf{y}}$ term compensates for this. The second delta function can be exploited to analytically evaluate the integral w.r.t $\theta_{\mathbf{y}}$ via the sifting property:

$$\boldsymbol{w}(\mathbf{x}, \hat{\mathbf{k}}) = \int_{\boldsymbol{\Gamma}} \frac{\boldsymbol{w}^{+}(\mathbf{y}, \widehat{\mathbf{R}})}{R} \delta\left(\cos^{-1}(\hat{\mathbf{k}} \cdot \widehat{\mathbf{R}})\right) V(\mathbf{x}, \mathbf{y}) \cos\theta_{\mathbf{y}} \, d\Gamma_{\mathbf{y}} \qquad \textbf{3.32}$$

This is the directional energy distribution at a point receiver. $\cos\theta_{\mathbf{y}} = \hat{\mathbf{n}}_{\mathbf{y}} \cdot \widehat{\mathbf{R}}$ can be substituted into this for ease of numerical evaluation. $V(\mathbf{x}, \mathbf{y})$ is the visibility function, which again can only be non-zero if the ray path is un-occluded. But now it must also to check if the ray leaves the front-side of $\Gamma_{\mathbf{y}}$. Visibility checks from boundary to receiver require only that $\hat{\mathbf{n}}_{\mathbf{y}} \cdot \widehat{\mathbf{R}} > 0$, whereas those for boundary-to-boundary mappings require that $\hat{\mathbf{n}}_{\mathbf{y}} \cdot \widehat{\mathbf{R}} > 0$ and $\hat{\mathbf{n}}_{\mathbf{x}} \cdot \widehat{\mathbf{R}} < 0$.

Eq. 3.32 is equivalent to the FP operator that the Nottingham group uses as a starting point in their formulations. The only significant difference is that the Nottingham group's formulation [15] integrates and later sifts in 'momentum' (equivalent to χ), whereas EBEM integrates w.r.t $\theta_{\mathbf{y}}$ (instead of $\chi_{\mathbf{y}}$), and sift in $\theta_{\mathbf{y}}$ and $\theta_{\mathbf{x}}$.

3.8 DISCRETISATION

3.8.1 Geometry and mesh

The 2D acoustic domain is enclosed by a boundary Γ which is made of a closed loop of N connected line elements indexed by Γ_n such that:

$$\Gamma = \bigcup_{n=0}^{N+1} \Gamma_n \tag{3.33}$$

The length of the n^{th} line element with its start and end vertices at $\mathbf{v}_n$ and $\mathbf{v}_{n+1}$ is computed as:

$$l_n = |\mathbf{v}_{n+1} - \mathbf{v}_n| \tag{3.34}$$

The position on each line element is parametrised by a dimensionless positional parameter ξ. This parameter can take a value between 0 and 1:

$$\mathbf{x}(n, \xi) = (1 - \xi)\mathbf{v}_n + \xi\mathbf{v}_{n+1} \tag{3.35}$$

The position around the entire boundary is parametrised with a different dimensionless parameter μ in the range $0 \leq \mu \leq N$ by taking $n = \lfloor \mu \rfloor$ and $\xi = \mu - n$ and then using eq. 3.35, so we have:

$$\mathbf{x}(\mu) = (1 + \lfloor \mu \rfloor - \mu)\mathbf{v}_{\lfloor \mu \rfloor} + (\mu - \lfloor \mu \rfloor)\mathbf{v}_{\lfloor \mu \rfloor + 1} \tag{3.36}$$

The unit tangent vector $\hat{\mathbf{t}}_n$ on the n^{th} element is constant and equal to:

$$\hat{\mathbf{t}}_n = [\mathbf{v}_{n+1} - \mathbf{v}_n]/l_n \tag{3.37}$$

The unit normal vector $\hat{\mathbf{n}}_n$ on the n^{th} element is constant and points perpendicular to $\hat{\mathbf{t}}_n$ into Ω, hence:

$$\hat{\mathbf{t}}(\mu) = \hat{\mathbf{t}}_{\lfloor \mu \rfloor}$$
$$\hat{\mathbf{n}}(\mu) = \hat{\mathbf{n}}_{\lfloor \mu \rfloor} \quad \textbf{3.38}$$

3.8.2 Discretisation on the boundary

The EBEM algorithm discretises incoming and outgoing power at the boundary separately. Acoustic absorption is emulated with a 'Reflectance' matrix discussed later in this chapter. The discretised sound power will be the product of spatial and angular interpolation (or 'basis') functions, b_n and a_q respectively.

$$w^{\pm}\left(\mathbf{x}(\mu), \hat{\mathbf{k}}^{\pm}(\chi)\right) = \sum_{n=0}^{N}\sum_{q=0}^{Q} \mathbf{w}^{\pm}[nQ+q]\, b_n(\mu) a_q(\chi) \quad \textbf{3.39}$$

Here $\mathbf{x} \in \Gamma$ and $\mathbf{w}^{\pm}$ is a vector of coefficients, where the two sets of indices n and q have been collapsed into a single index $nQ + q$. $b_n(\mu)$ is a spatial interpolation function. $a_q(\chi)$ is an angular interpolation function

3.8.3 Spatial basis functions

Discontinuous piecewise-constant (PWC) was chosen as the spatial basis function used in the EBEM codebase due its simplicity and precedent from other works.

For PWC, the DOF will be associated with elements. Due to their discontinuous nature, the spatial solution on the boundary becomes discontinuous. The equation for PWC functions is:

$$b_n(\mu) = \begin{cases} 1 & n \le \mu \le n+1 \equiv \mathbf{x} \in \Gamma_n \\ 0 & \text{otherwise} \end{cases} \quad \textbf{3.40}$$

3.8.4 Angular basis functions

The angular basis functions discretise $w\left(\mathbf{x}, \hat{\mathbf{k}}(\chi)\right)$ over the range $-1 \le \chi \le 1$. The codebase for the EBEM algorithm was developed so that the angular basis functions can be changed readily and the associated variation in solution accuracy can be easily studied. The choices of angular basis functions implemented within the EBEM codebase are discontinuous piecewise-constant, continuous piecewise linear, and continuous orthogonal polynomials.

3.8.4.1 Discontinuous Piecewise-Constant (PWC)

When interpolating angle, PWC functions have $Q+1$ nodes (as constant basis functions require a single interpolation node for each angular subdivision) located at $\chi_q = 2q/Q - 1$, where the index q ranges from 0 to Q. Equation for these functions are:

$$a_q(\chi) = \begin{cases} 1 & \chi_q \leq \chi \leq \chi_{q+1} \\ 0 & \text{otherwise} \end{cases} \qquad \textbf{3.41}$$

This choice is compact in angle, which will later be seen to make the boundary-to-boundary interaction matrix sparse. The functions are also orthogonal, which makes the mass matrix diagonal.

Figure 3.12 Discontinuous PWC basis in angle

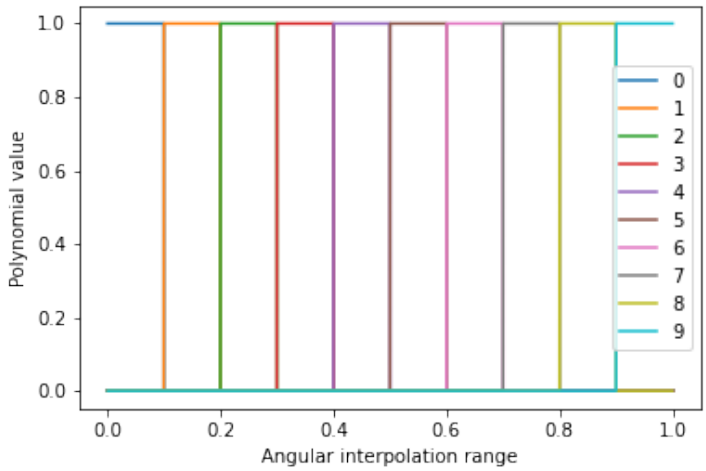

3.8.4.2 Continuous Piecewise Linear (PWL)

Using PWL for interpolating angle requires Q nodes (as linear basis functions require two interpolation nodes for each angular subdivision) placed at $\chi_q = 2q/(Q-1) - 1$, where the index q ranges from 0 to Q. Equation for these functions are:

$$a_q(\chi) = \begin{cases} \dfrac{\chi - \chi_{q-1}}{\chi_q - \chi_{q-1}} & \chi_{q-1} \leq \chi \leq \chi_q \\ \dfrac{\chi_{q+1} - \chi}{\chi_{q+1} - \chi_q} & \chi_q \leq \chi \leq \chi_{q+1} \\ 0 & \text{otherwise} \end{cases} \qquad \textbf{3.42}$$

This choice has the benefit of making the solution in the domain continuous while retaining the 'compact in angle' property that makes the boundary-to-boundary interaction matrix sparse, but it makes the discretisation scheme non-orthogonal meaning the mass matrix – which must be inverted – will contain non-zero off-diagonal elements.

Figure 3.13 Continuous PWL basis in angle

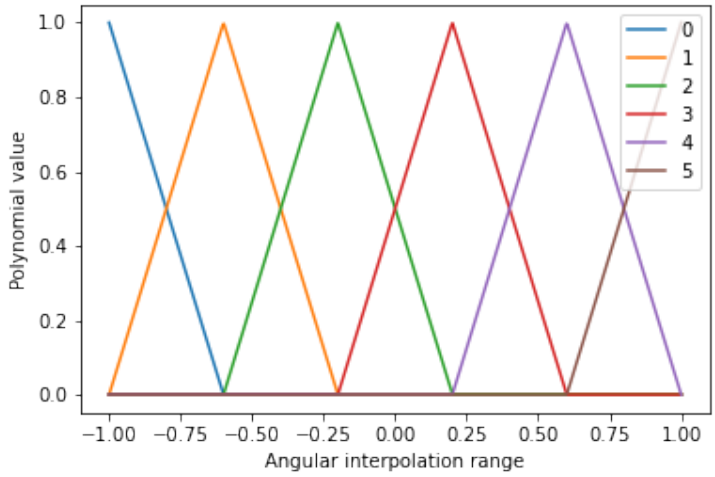

3.8.4.3 Continuous Orthogonal Polynomials

Orthogonal polynomials such as Legendre, Chebyshev or Lobatto as χ as their argument. Legendre polynomials have the property that [46]:

$$\int_{-1}^{1} P_m(\chi)P_n(\chi)d\chi = \frac{2}{2n+1}\delta_{mn} \qquad 3.43$$

Figure 3.14 Legendre polynomials of order 0 through 5

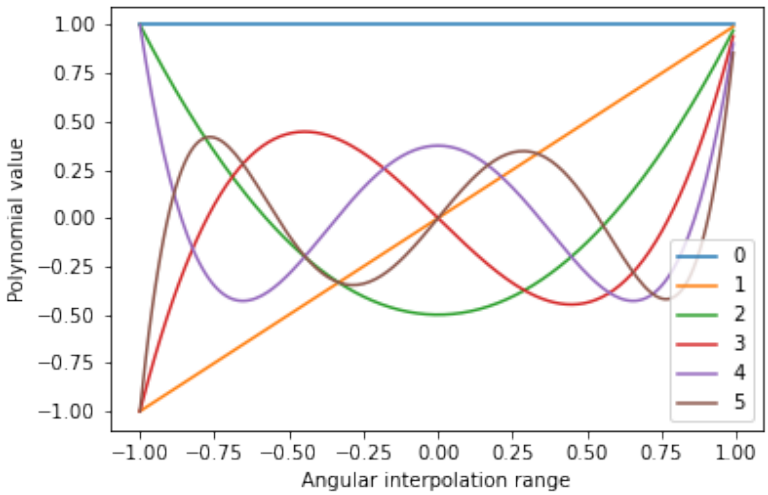

Chebyshev polynomials map to cosine modes in angle. They have the property that:

$$\int_{-1}^{1} \frac{T_m(\chi)T_n(\chi)}{\sqrt{1-\chi^2}} d\chi = \begin{cases} 0 & \text{if } n \neq m \\ \pi & \text{if } n = m = 0. \\ \pi/2 & \text{if } n = m \neq 0 \end{cases} \quad \textbf{3.44}$$

Figure 3.15 Chebyshev polynomials of order 0 through 5

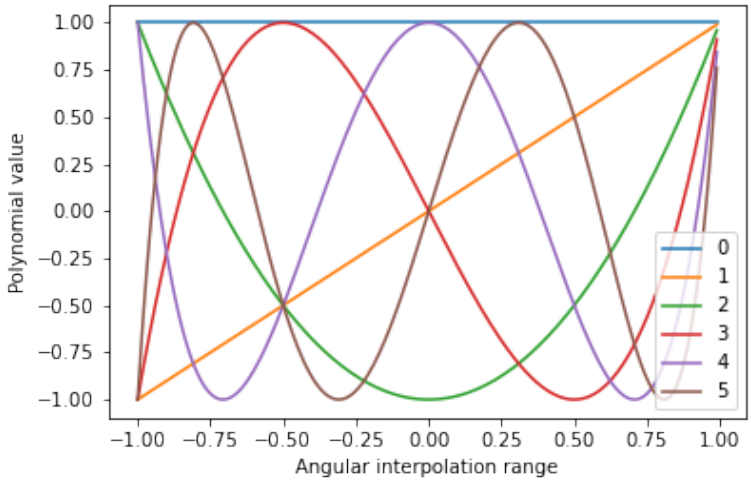

Another choice is Lobatto polynomials which are linear combinations of Legendre polynomials. A primary benefit of using Lobatto polynomials is their hierarchical nature [47]. They are defined as:

$$l_0(\chi) = \frac{1-\chi}{2}$$

$$l_1(\chi) = \frac{\chi+1}{2} \quad \textbf{3.45}$$

$$l_q(\chi) = \sqrt{\frac{2q-1}{2}} \int_{-1}^{\chi} L_{q-1}(s)ds$$

This is for $-1 \leq \chi \leq 1$. Here, L_q is the Legendre polynomial of order $q \geq 2$.

Figure 3.16 Lobatto polynomials of order 0 through 5

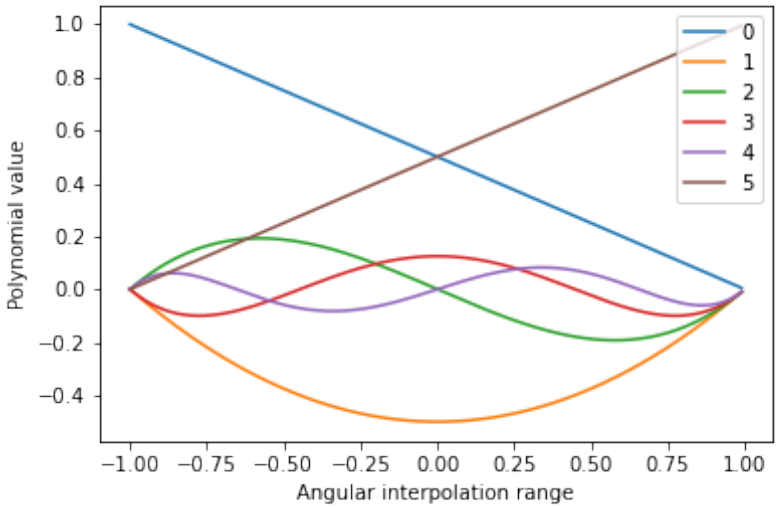

An advantage of using continuous orthogonal polynomials is that they make the solution within the domain continuous. Additionally, the orthogonality of the Legendre polynomials means the mass-matrix will be diagonal when using them. Notably, this is not the case with Chebyshev polynomials because the integrals in its mass matrix do not include the denominator term required for orthogonality. The Nottingham group report that Chebyshev polynomials outperform Legendre. Also, Chebyshev polynomials are related to the Fourier series, so it should perform similar to the Duke group's EI-BEM formulation. A disadvantage is that they all support the full range $-1 \leq \chi \leq 1$ leading to a boundary-to-boundary interaction matrix that is dense. Although using the natural inner product in the case of Chebyshev polynomials would have resulted in a diagonal mass matrix, a potential disadvantage is that the weighting term in eq. 3.44 becomes infinite at either ends of the range of χ, i.e. at 1 or -1. Hence this was not considered as a possible choice to be used as angular basis.

3.8.5 Source directivity

This section provides a mathematical description of the directional source discussed in Section 3.4.1. To model directional characteristics, a Fourier series in angle θ_s is utilised. A Fourier series can represent any angular distribution as a (possibly infinite) sum of sines and cosines. The source directivity function $W_s(\theta_s)$ can be written in this form as:

$$W_s(\theta_s) = \sum_{q=0}^{Q_s} a_q \cos q\theta_s + \sum_{q=1}^{Q_s} b_q \sin q\theta_s \qquad \textbf{3.46}$$

Where:

Q_S is the source directivity order

a_q are the Fourier series cosine coefficients (provided by a user)

b_q are the Fourier series sine coefficients (provided by a user)

For an omnidirectional source, $Q_\mathrm{S} = 0$ and $a_0 = W/2\pi$ where W is the total source power in Watts per metre.

If a directional distribution W_s is pre-defined (eg. from measurement), a_q and b_q can be found from standard Fourier encoding equations:

$$W_\mathrm{s} \approx \sum_{q=0}^{Q_\mathrm{S}} a_p \cos q\theta_\mathrm{s} + \sum_{q=1}^{Q_\mathrm{S}} b_p \sin q\theta_\mathrm{s} \qquad \textbf{3.47}$$

The Fourier series is a natural choice to interpolate cyclic data versus angle in the range 0 to 2π. Moreover, they are the angular part of a Fourier Bessel series, and this can be used to describe high-order sources that are solutions to the 2D Helmholtz equation. Hence, this choice is attractive because it is consistent with low frequency approaches. In contrast, angular ranges on the boundary are half this range. Using a Fourier series in direction would have resulted in a non-orthogonality issue encountered in [10]. By multiplying of the angular argument by 2, the orthogonality is recovered but enforces a non-physical periodicity between the ends of the angular range. Ends of the angular range having different intensities may result in unwanted Gibbs artefacts.

3.8.6 Receiver discretisation

Similar to the directional point source, the directional power density incident at a point receiver is discretised with a Fourier series in receiving angle θ_r. Using similar Fourier series representations for source and receiver directivity allows easy analysis and plotting of different parts of the algorithm and makes reciprocity clearer to see. The received power arriving at a receiver $w(\mathbf{x}, \hat{\mathbf{k}})$ is described as:

$$w\left(\mathbf{x}, \hat{\mathbf{k}}(\theta_\mathrm{r})\right) \approx \sum_{p=0}^{P_\mathrm{r}} a_p \cos p\theta_\mathrm{r} + \sum_{p=1}^{P_\mathrm{r}} b_p \sin p\theta_\mathrm{r} \qquad \textbf{3.48}$$

Where:

P_r is the receiver order

a_p and b_p are the output data computed from $w\left(\mathbf{x}, \hat{\mathbf{k}}(\theta_\mathrm{r})\right)$, which is a result from other parts of the algorithm. Once it is found it is mapped onto the representation in eq. 3.48. a_p and b_p are stacked into a single vector of length $2P_\mathrm{r} + 1$ for easier data handling.

By exploiting the standard equations for finding the coefficients for a Fourier series, we get:

$$\mathbf{w}_\mathrm{r}[p] = \begin{cases} a_p = \dfrac{1}{(1+\delta_p)\pi}\displaystyle\int_0^{2\pi} w\left(\mathbf{x}, \hat{\mathbf{k}}(\theta_\mathrm{r})\right)\cos(p\theta_\mathrm{r})\, d\theta_\mathrm{r} & \text{if } p \le P \\ b_{p-P} = \dfrac{1}{\pi}\displaystyle\int_0^{2\pi} w\left(\mathbf{x}, \hat{\mathbf{k}}(\theta_\mathrm{r})\right)\sin((p-P)\theta_\mathrm{r})\, d\theta_\mathrm{r} & \text{if } p > P \end{cases} \quad \textbf{3.49}$$

Where δ_p is the Kronecker delta, which equals 1 when $p = 0$, and 0 otherwise. The total power arriving at the receiver irrespective of direction is:

$$W_\mathrm{r}(\mathbf{x}) = \oint w(\mathbf{x}, \hat{\mathbf{k}}) d\hat{\mathbf{k}} \equiv \int_0^{2\pi}\left[\sum_{p=0}^{P_\mathrm{r}} a_p \cos(p\theta_\mathrm{r}) + \sum_{p=1}^{P_\mathrm{r}} b_p \sin(p\theta_\mathrm{r})\right] d\theta_\mathrm{r} \quad \textbf{3.50}$$
$$= 2\pi a_0$$

Intensity at the receiver can now be computed as:

$$\mathbf{I}(\mathbf{x}) = \oint w(\mathbf{x}, \hat{\mathbf{k}})\hat{\mathbf{k}}\, d\hat{\mathbf{k}} \equiv \int_0^{2\pi} w\left(\mathbf{x}, \hat{\mathbf{k}}(\theta_\mathrm{r})\right)[\hat{\mathbf{x}}\cos\theta_\mathrm{r} + \hat{\mathbf{y}}\sin\theta_\mathrm{r}] d\theta_\mathrm{r}$$
$$= \hat{\mathbf{x}}\int_0^{2\pi} w\left(\mathbf{x}, \hat{\mathbf{k}}(\theta_\mathrm{r})\right)\cos\theta_\mathrm{r}\, d\theta_\mathrm{r} + \hat{\mathbf{y}}\int_0^{2\pi} w\left(\mathbf{x}, \hat{\mathbf{k}}(\theta_\mathrm{r})\right)\sin\theta_\mathrm{r}\, d\theta_\mathrm{r} \quad \textbf{3.51}$$
$$= \pi a_1 \hat{\mathbf{x}} + \pi b_1 \hat{\mathbf{y}}$$

Directional receiver information in this format can be used in post processing in various models of spatial audio reproduction technology [7]. This mirrors the framework used in [20] for auralisation of BEM and is equivalent to 2D Ambisonics.

3.9 GALERKIN BOUNDARY ELEMENT METHOD

A Galerkin BEM scheme is used to map power arriving at the boundary onto the discretisation scheme. The discretisation scheme allows the energy distribution on the boundary to be represented by a finite set of coefficients. These coefficients are computed for incident or re-reflected sound by the 'testing' integral.

Galerkin BEM minimises the projection of the error in the solution of this in the chosen 'space' of testing functions. It performs an inner product between the incoming energy distribution and a set of 'testing' functions. These allow choice in how error in the solution is minimised. Choosing them to match the basis functions results in a 'Bubnov-Galerkin' method which minimises mean-squared error in the same approximation space as the solution. Choosing different testing and basis functions results in a 'Petrov-Galerkin' method which minimises mean-squared error in some other space. For example, if Lagrange functions are used as basis functions and Dirac delta functions as testing functions, the Galerkin BEM reduces to a collocation type scheme. The Nottingham group recently opted to do the latter [49], using delta functions as basis in angle (so a finite set of angles instead of a distribution) and PWC testing functions. This produces an effect very similar to the 'ray direction quantisation' technique [35]. The main benefit is that ray transport directions can be preserved when transmitting through boundaries of sub-domains, although eliminating the need for numerical integration is also beneficial.

For the EBEM presented herein, a Bubnov-Galerkin scheme was chosen for its simplicity, symmetry and similarity with the energy interpretation in [50].

A feature of Galerkin BEM is that it does not compute the coefficients of eq. 3.39 directly. Instead, it computes a vector of 'projections', from which the coefficients can be found by solving a matrix equation. The matrix involved in this equation is commonly known as the 'mass matrix', due to its similarity with the mass matrix in FEM. Consider the double-layer potential $\mathcal{D}$ used in standard acoustics BEM:

$$\mathcal{D}\{\phi\}(\mathbf{x}) = \iint_{\Gamma_y} \frac{\partial G}{\partial n_y}(\mathbf{x},\mathbf{y})\phi(\mathbf{y})d\Gamma_y \qquad \textbf{3.52}$$

Where $G(\mathbf{x},\mathbf{y})$ is the free space Green's function. The boundary source distribution $\phi(\mathbf{y})$ resides on the boundary Γ_y and are evaluated at all $\boldsymbol{x}$. In practice, $\phi(\mathbf{y})$ is written in discretised form as:

$$\phi(\mathbf{y}) = \sum_{j=0}^{J} \boldsymbol{\phi}_J \phi_J(\mathbf{y}) \tag{3.53}$$

$\boldsymbol{\phi}$ is a vector of coefficients and $\phi_j(\mathbf{y})$ is a family of basis functions on a mesh spanning Γ_y. Substituting eq. 3.53 into the equation for $\mathcal{D}$ leads to $\mathcal{D}\{\phi\}(\boldsymbol{x}) = \mathbf{d}^{\boldsymbol{T}}\boldsymbol{\phi}$ where:

$$\mathbf{d}_J = \iint_{\Gamma_\mathbf{y}} \frac{\partial G}{\partial n_y}(\mathbf{x},\mathbf{y})\phi_J(\boldsymbol{y})d\Gamma_y \tag{3.54}$$

Here $\mathbf{d}$ is the discretised version of $\mathcal{D}$ evaluated at $\mathbf{x}$.

The aim, however, is often to map $\mathcal{D}\{\phi\}(\mathbf{x})$ onto another set of basis functions, so it can also be represented in a discretised form, now with coefficients $\boldsymbol{\chi}$. Consider a third space, usually termed *dual-to-range* in BEM literature [51]. This space comprises of a set of 'testing' functions $\psi_i(\mathbf{x})$. Now, $\boldsymbol{\chi}$ can be found by solving the equation:

$$\mathbf{M}\boldsymbol{\chi} = \mathbf{D}\boldsymbol{\phi} \tag{3.55}$$

Where:

$$\mathbf{D}_{i,j} = \iint_{\Gamma_\mathbf{x}} \iint_{\Gamma_\mathbf{y}} \psi_i(\mathbf{x}) \frac{\partial G}{\partial n_\mathbf{y}}(\mathbf{x},\mathbf{y})\phi_j(\mathbf{y})d\Gamma_\mathbf{y}\, d\Gamma_\mathbf{x}, \tag{3.56}$$

And,

$$\mathbf{M}_{i,j} = \iint_{\Gamma_\mathbf{x}} \psi_i(\mathbf{x})\chi_j(\mathbf{x})d\Gamma_\mathbf{x}. \tag{3.57}$$

This framework minimises the $\mathcal{L}_2$ norm of the equation to be solved in the space of the testing functions. **D** computes the projections of $\mathcal{D}\{\phi\}(\mathbf{x})$ onto the testing functions $\psi_i(\mathbf{x})$. The

mass matrix undoes any overlap or non-biorthogonality between $\psi_i(\mathbf{x})$ and $\chi_i(\mathbf{x})$. This amounts to solving $\boldsymbol{\chi} = \mathbf{M}^{-1}\mathbf{D}\boldsymbol{\phi}$.

3.9.1 Projection operator and Mass matrix

The mapping of some arriving field $w(\mathbf{x}, \hat{\mathbf{k}}^-)$, as is computed by eq. 3.28 for power from a source and eq. 3.32 for sound from the boundary on the previous reflection order, is performed by an inner product integral in boundary position $\mathbf{x}$ and angle $\theta_\mathbf{x}$. This computes a vector $\mathbf{p}^-$ termed the 'projections':

$$\begin{aligned}\mathbf{p}^-[mP+p] &= \int_\Gamma \int_{-\frac{\pi}{2}}^{\frac{\pi}{2}} w(\mathbf{x}, \hat{\mathbf{k}}^-) b'_m(\mathbf{x}) a'_p(\hat{\mathbf{k}}^-) \cos\theta_\mathbf{x}\, d\theta_\mathbf{x} d\Gamma_\mathbf{x} \\ &= \int_\Gamma \int_{-1}^{1} w(\mathbf{x}, \hat{\mathbf{k}}^-) b'_m(\mathbf{x}) a'_p(\hat{\mathbf{k}}^-) d\chi_\mathbf{x} d\Gamma_\mathbf{x}\end{aligned} \quad \textbf{3.58}$$

In eq. 3.58, $\hat{\mathbf{k}}^-$ is a function of $\theta_\mathbf{x}$ in the first integral according to eq. 3.12 and of $\chi_\mathbf{x}$ in the second according to eq. 3.13. The $\cos\theta_\mathbf{x}$ arises by the same logic that $\cos\theta_\mathbf{y}$ arose in eq. 3.31. $w(\mathbf{x}, \hat{\mathbf{k}}^-)$ is a power density that includes a 'per metre' that is perpendicular to the direction of propagation $\hat{\mathbf{k}}^-$, but the integral is w.r.t. boundary length. The $\cos\theta_\mathbf{x}$ term compensates for this. In the second integral the identity in eq. 3.14 has been exploited.

To build a matrix that maps these projections back to the coefficients $\mathbf{w}^-$, eq. 3.39 is substituted into eq. 3.58. Unpacking all the combinations of m, n, p and q into a matrix $\mathbf{M}$ gives:

$$\begin{aligned}\mathbf{M}[mP+p, nQ+q] &= \int_\Gamma \int_{-\frac{\pi}{2}}^{\frac{\pi}{2}} b'_m(\mathbf{x}) b_n(\mathbf{x}) a'_p(\hat{\mathbf{k}}^-) a_q(\hat{\mathbf{k}}^-) \cos\theta_\mathbf{x}\, d\theta_\mathbf{x} d\Gamma_\mathbf{x} \\ &= \int_\Gamma \int_{-1}^{1} b'_m(\mathbf{x}) b_n(\mathbf{x}) a'_p(\hat{\mathbf{k}}^-) a_q(\hat{\mathbf{k}}^-) d\chi_\mathbf{x} d\Gamma_\mathbf{x}\end{aligned} \quad \textbf{3.59}$$

This matrix shows the overlap between the basis function combinations in the discretisation scheme. It is termed the 'mass matrix' because its form matches the FEM mass matrix. Orthogonal discretisation schemes (orthogonal polynomials or PWC will give diagonal matrices. Non-orthogonal schemes, such as continuous PWL will also have some off-diagonal entries.

From the above we have $\mathbf{p}^- = \mathbf{M}\mathbf{w}^-$. It follows that $\mathbf{w}^- = \mathbf{M}^{-1}\mathbf{p}^-$. Multiplying by the inverse of $\mathbf{M}$ therefore unpicks the non-orthogonality in the discretisation scheme. It also performs a normalising role. This is equivalent to the normalisation that Siltanen *et al* [12] hard coded in eq. 2.28 and 2.29 . Inclusion of $\mathbf{M}$ allows EBEM to change basis functions without modification to the algorithm.

Note that the notation on the left-hand sides of eq. 3.58 and eq. 3.59 assume that P and Q are the same for all boundary elements. But this is just a notation convenience. Allowing different elements to have different P and Q (so P_n and Q_n) would be possible using a standard matrix assembly process.

Note also that the 'testing' functions $b'_m(\mathbf{x})$ and $a'_p(\hat{\mathbf{k}}^-)$ are likely to be the same as the basis functions used for discretisation of $w^{\pm}(\mathbf{x}, \hat{\mathbf{k}}^{\pm})$ in eq. 3.39, which would make $\mathbf{M}$ symmetrical. But this is not essential. They could be drawn from different family of basis functions if preferred.

For a flat element (or elements) with constant normal vector eq. 3.59 can be separated into the product of two integrals, making the mass matrix block diagonal

$$\mathbf{M}[mP+p, nQ+q] = \int_{\Gamma} b'_m(\mathbf{x}) b_n(\mathbf{x}) d\Gamma_{\mathbf{x}} \times \int_{-1}^{1} a'_p(\hat{\mathbf{k}}^-) a_q(\hat{\mathbf{k}}^-) d\chi_{\mathbf{x}} \qquad \mathbf{3.60}$$

3.9.2 Source to boundary mapping

The w in eq. 3.58 is replaced by w^- from eq. 3.28 to give the following projection:

$$\mathbf{p}_0^-[mP+p] = \int_{\Gamma} \int_{-\frac{\pi}{2}}^{\frac{\pi}{2}} \frac{W_s(\theta_s)}{R} \delta\left(\cos^{-1}(\hat{\mathbf{k}}^- \cdot \hat{\mathbf{R}})\right) \times V(\mathbf{x}, \mathbf{y}_0) b'_m(\mathbf{x}) a'_p(\hat{\mathbf{k}}^-) \cos\theta_{\mathbf{x}} \, d\theta_{\mathbf{x}} d\Gamma_{\mathbf{x}} \qquad \mathbf{3.61}$$

The sifting property of the delta function can be exploited since it only gives a non-zero value for $\hat{\mathbf{k}}^- = \hat{\mathbf{R}}$. This removes the integral over angle. Figure 3.10 shows that $\cos\theta_{\mathbf{x}} = -\hat{\mathbf{n}}_{\mathbf{x}} \cdot \hat{\mathbf{k}}^- = -\hat{\mathbf{n}}_{\mathbf{x}} \cdot \hat{\mathbf{R}}$, hence:

$$\mathbf{p}_0^-[mP+p] = -\int_{\Gamma} \frac{W_s(\theta_s)}{R} V(\mathbf{x}, \mathbf{y}_0) b'_m(\mathbf{x}) a'_p(\hat{\mathbf{R}}) \hat{\mathbf{n}}_{\mathbf{x}} \cdot \hat{\mathbf{R}} d\Gamma_{\mathbf{x}} \qquad \mathbf{3.62}$$

If $\chi_{\mathbf{x}}$ is required to evaluate a'_p then it can be found by $\chi_{\mathbf{x}} = -\hat{\mathbf{t}}_{\mathbf{x}} \cdot \hat{\mathbf{k}}^- = -\hat{\mathbf{t}}_{\mathbf{x}} \cdot \widehat{\mathbf{R}}$. θ_{s} can be found from $\widehat{\mathbf{R}}$ by $\theta_{\mathrm{s}} = \mathrm{atan2}\left(\widehat{\mathbf{R}}_y, \widehat{\mathbf{R}}_x\right)$. The incident wave boundary weights $\mathbf{w}_0^-$ can be found by $\mathbf{w}_0^- = \mathbf{M}^{-1}\mathbf{p}_0^-$. The discretised statement for source directivity in eq. 3.46 is substituted here, allowing $\mathbf{p}_0^-$ (and therefore $\mathbf{w}_0^-$) to be found by $\mathbf{p}_0^- = \mathbf{T}_{\mathrm{sb}}\mathbf{w}_{\mathbf{s}}$, and the mutual orthogonality of sine and cosine integrals was exploited to get:

$$\mathbf{T}_{\mathrm{sb}}[mP + p, q] = \begin{cases} -\int_{\Gamma} \frac{\cos(q\theta_{\mathrm{s}})}{R} V(\mathbf{x}, \mathbf{y}_0) b'_m(\mathbf{x}) a'_p\left(\widehat{\mathbf{R}}\right) \widehat{\mathbf{n}}_{\mathbf{x}} \cdot \widehat{\mathbf{R}} d\Gamma_{\mathbf{x}} & \text{if } q \leq Q \\ -\int_{\Gamma} \frac{\sin((q-Q)\theta_{\mathrm{s}})}{R} V(\mathbf{x}, \mathbf{y}_0) b'_m(\mathbf{x}) a'_p\left(\widehat{\mathbf{R}}\right) \widehat{\mathbf{n}}_{\mathbf{x}} \cdot \widehat{\mathbf{R}} d\Gamma_{\mathbf{x}} & \text{if } q > Q \end{cases} \quad \textbf{3.63}$$

3.9.3 Reflection operator

This section presents a representation of the reflection operation in eq. 3.29 as a matrix multiplication. Substituting eq. 3.39 into eq. 3.29 and then substituting $w^+(\mathbf{x}, \chi^+)$ for $w\left(\mathbf{x}, \hat{\mathbf{k}}^-\right)$ in eq. 3.58, and unpacking all the combinations, gives:

$$\mathbf{R}[mP + p, nQ + q] = \int_{\Gamma} \int_{-1}^{1} b'_m(\mathbf{x}) a'_p(\hat{\mathbf{k}}^+) \int_{-1}^{1} R(\mathbf{x}, \chi^+, \chi^-)\, b_n(\mathbf{x}) a_q(\hat{\mathbf{k}}^-) d\chi^- d\chi^+ d\Gamma_{\mathbf{x}} \quad \textbf{3.64}$$

For a flat element with constant normal vector, and where R is constant over an element, this can be separated into the product of two integrals:

$$\mathbf{R}[mP + p, nQ + q] = \int_{\Gamma} b'_m(\mathbf{x}) b_n(\mathbf{x}) d\Gamma_{\mathbf{x}} \times \int_{-1}^{1} a'_p(\hat{\mathbf{k}}^+) \int_{-1}^{1} R(\mathbf{x}, \chi^+, \chi^-)\, a_q(\hat{\mathbf{k}}^-) d\chi^- d\chi^+ \quad \textbf{3.65}$$

The outgoing wave boundary weights $\mathbf{w}_i^+$ can be found by $\mathbf{w}_i^+ = \mathbf{M}^{-1}\mathbf{R}\mathbf{w}_i^-$. If a boundary is specularly reflecting with no absorption, then $R(\mathbf{x}, \chi^+, \chi^-) = \delta(\chi^+ - \chi^-)$. In this case $\mathbf{R} = \mathbf{M}$ and $\mathbf{w}_i^+ = \mathbf{w}_i^-$.

3.9.4 Boundary to boundary mapping

This section aims to represent the propagation operation in eq. 3.32 from boundary to boundary as a matrix multiplication. Eq. 3.32 is substituted into eq. 3.58 and eq. 3.39 is used for the radiating directional power density $w^{+}(\mathbf{y}, \widehat{\mathbf{R}})$. Unpacking all the combinations of m, n, p and q into a matrix $\mathbf{T_{bb}}$ gives:

$$\begin{aligned}\mathbf{T_{bb}}[mP+p, nQ+q] \\ = -\int_{\Gamma}\int_{-\frac{\pi}{2}}^{\frac{\pi}{2}}\int_{\Gamma}\frac{1}{R}\delta\left(\cos^{-1}\left(\hat{\mathbf{k}}\cdot\widehat{\mathbf{R}}\right)\right)b'_m(\mathbf{x})b_n(\mathbf{y})a'_p\left(\hat{\mathbf{k}}^{-}\right)a_q\left(\widehat{\mathbf{R}}\right) \\ \times \cos\theta_{\mathbf{x}}\cos\theta_{\mathbf{y}}\, d\Gamma_{\mathbf{y}} d\theta_{\mathbf{x}} d\Gamma_{\mathbf{x}}\end{aligned} \quad \textbf{3.66}$$

The sifting property of the delta function can be exploited to eliminate the integral over $\theta_{\mathbf{x}}$, setting $\hat{\mathbf{k}}^{-} = \widehat{\mathbf{R}}$

$$\begin{aligned}\mathbf{T_{bb}}[mP+p, nQ+q] \\ = \int_{\Gamma}\int_{\Gamma}\frac{1}{R}b'_m(\mathbf{x})b_n(\mathbf{y})a'_p\left(\widehat{\mathbf{R}}\right)a_q\left(\widehat{\mathbf{R}}\right)\cos\theta_{\mathbf{x}}\cos\theta_{\mathbf{y}}\, d\Gamma_{\mathbf{y}} d\Gamma_{\mathbf{x}} \\ = -\int_{\Gamma}\int_{\Gamma}\frac{1}{R}b'_m(\mathbf{x})b_n(\mathbf{y})a'_p(\widehat{\mathbf{R}})a_q(\widehat{\mathbf{R}})\hat{\mathbf{n}}_{\mathbf{y}}\cdot\widehat{\mathbf{R}}\hat{\mathbf{n}}_{\mathbf{x}}\cdot\ \widehat{\mathbf{R}} d\Gamma_{\mathbf{y}} d\Gamma_{\mathbf{x}}\end{aligned} \quad \textbf{3.67}$$

In eq. 3.67, $\cos\theta_{\mathbf{x}} = -\hat{\mathbf{n}}_{\mathbf{x}}\cdot\ \widehat{\mathbf{R}}$ and $\cos\theta_{\mathbf{y}} = \hat{\mathbf{n}}_{\mathbf{y}}\cdot\ \widehat{\mathbf{R}}$ have been substituted. This produces a boundary-to-boundary propagation operator $\mathbf{T_{bb}}$ involving two spatial integrals. The presence of the $\cos\theta_{\mathbf{x}}$ and $\cos\theta_{\mathbf{y}}$ terms means that all entries in $\mathbf{T_{bb}}$ for any pair of elements that are co-planar. The Nottingham group observe that the integrand of $\mathbf{T_{bb}}$ can be singular for adjacent elements that are not co-planar i.e., two on opposite sides of a corner in the geometry. [16] uses the Telles transform to address this. It is to be noted that the $1/R$ singularity in the boundary-to-boundary interaction process affecting adjacent but non-coplanar elements was regularised using the Sato transform [52]. A Sato transform of order $\sigma \geq 2$ is given by:

$$\xi(\gamma) = \bar{\xi} - \frac{\bar{\xi}}{2^{\sigma-1}}\left(1-\bar{\xi}\gamma\right)^{\sigma} \quad \textbf{3.68}$$

Where γ are the original integration points, and ξ are the remapped integration points obtained using any Gaussian Quadrature rule. The location of the singularity $\bar{\xi}$ must be at $+1$ or -1 as this transform is valid only for endpoint singularities.

3.10 MAPPING OF POWER AT RECEIVER

In this section, the objective is to find the values of the set of coefficients a_p and b_p required to represent the directional energy arriving at receivers according to eq. 3.48. This is done by substituting statements for $w(\mathbf{x}, \hat{\mathbf{k}})$ from Section 3.4 and Section 3.7 into eq. 3.49.

3.10.1 Source to receiver mapping

In this section, the representation for directional power distribution arriving directly from a source in eq. 3.25 is combined with the discretisation of $W_\mathrm{s}(\theta_\mathrm{s})$ in eq. 3.46 and substituted into eq. 3.49. Unpacking of all combinations p and q gives a contribution $\mathbf{T}_{\mathrm{s,r}}\mathbf{w}_\mathrm{s}$ to $\mathbf{w}_\mathrm{r}$ where:

$$\mathbf{T}_{\mathrm{sr}}[p,q] = \frac{V(\mathbf{x},\mathbf{y}_0)}{\mathrm{R}} \times \begin{cases} \dfrac{1}{(1+\delta_p)\pi}\cos(p\theta_\mathrm{r})\cos(q\theta_\mathrm{s}) & \text{if } p \le P \text{ and } q \le Q \\ \dfrac{1}{\pi}\sin((p-P)\theta_\mathrm{r})\cos(q\theta_\mathrm{s}) & \text{if } p > P \text{ and } q \le Q \\ \dfrac{1}{(1+\delta_p)\pi}\cos(p\theta_\mathrm{r})\sin((q-Q)\theta_\mathrm{s}) & \text{if } p \le P \text{ and } q > Q \\ \dfrac{1}{\pi}\sin((p-P)\theta_\mathrm{r})\sin((q-Q)\theta_\mathrm{s}) & \text{if } p > P \text{ and } q > Q \end{cases} \quad \textbf{3.69}$$

The delta function in eq. 3.25 has been exploited to remove the angular integral in eq. 3.49. This has sifted out the value of θ_r given by $\theta_\mathrm{r} = \mathrm{atan2}(-\widehat{\mathbf{R}}_y, -\widehat{\mathbf{R}}_x)$. We also have that $\theta_\mathrm{s} = \mathrm{atan2}(\widehat{\mathbf{R}}_y, \widehat{\mathbf{R}}_x)$. The function $V(\mathbf{x},\mathbf{y}_0)$ is a visibility function that is 1 if the ray path is un-occluded by boundaries and is 0 otherwise.

For the ray from a source to a receiver, the respective Fourier coefficients a_n are computed as:

$$a_n = \frac{1}{\pi}\int_0^{2\pi} \mathrm{I}_{inc}(\theta)\cos(\theta)\, d\theta \quad \textbf{3.70}$$

$$b_n = \frac{1}{\pi}\int_0^{2\pi} \mathrm{I}_{inc}(\theta)\,\sin(\theta)\,d\theta$$

Where $\mathrm{I}_{inc}(\theta)$ is the incident intensity at the receiver at angle θ. The angular distribution of incident rays at the receiver can be described as a delta function $\delta(\theta - \theta_r)$:

$$a_n = \frac{1}{\pi}\int_0^{2\pi} w(\theta_s)\,\delta(\theta-\theta_r)\cos(\theta)\,d\theta$$
$$b_n = \frac{1}{\pi}\int_0^{2\pi} w(\theta_s)\,\delta(\theta-\theta_r)\sin(\theta)\,d\theta \qquad \textbf{3.71}$$

Using the sifting property in angle, the coefficients are calculated for each ray from a source to the receiver in the enclosure:

$$a_n = \frac{1}{\pi}\,w\cos(\theta_r)$$
$$b_n = \frac{1}{\pi}\,w\sin(\theta_r) \qquad \textbf{3.72}$$

The Fourier series coefficients for source directivity with angle are now calculated are:

$$a_n = \sum_{Sources} \frac{W_s(\theta_s)\times\cos(n\theta_r)}{2\pi r}$$
$$b_n = \sum_{Sources} \frac{W_s(\theta_s)\times\sin(n\theta_r)}{2\pi r} \qquad \textbf{3.73}$$

For intensity received at a point, the Fourier series representation takes a similar form to the source directivity function:

$$W_r(\theta) = a_0 + \sum_{n=1}^{\infty}[a_n\cos(n\theta) + b_n\sin(n\theta)] \qquad \textbf{3.74}$$

3.10.2 Boundary to receiver mapping

This section explains how the propagation operation in eq. 3.32 from boundary to receiver is represented as a matrix multiplication. Eq. 3.32 is substituted into eq. 3.49 and eq. 3.39 is

substituted for the radiating directional power density $w^{+}(\mathbf{y}, \widehat{\mathbf{R}})$. Unpacking all combinations of n, p and q into a matrix $\mathbf{T}_{\mathrm{br}}$ gives:

$$\mathbf{T}_{\mathrm{br}}[p, nQ+q] = \frac{V(\mathbf{x},\mathbf{y})}{\mathrm{R}} \times \begin{cases} \dfrac{1}{(1+\delta_p)\pi} \times \displaystyle\int_{\Gamma} b_n(\mathbf{y}) a_q(\widehat{\mathbf{R}}) \widehat{\mathbf{n}}_{\mathbf{y}} \cdot \widehat{\mathbf{R}} \cos p\theta_{\mathrm{r}} \, d\Gamma_{\mathbf{y}} & \text{if } p \le P \\ \dfrac{1}{\pi} \times \displaystyle\int_{\Gamma} b_n(\mathbf{y}) a_q(\widehat{\mathbf{R}}) \widehat{\mathbf{n}}_{\mathbf{y}} \cdot \widehat{\mathbf{R}} \sin(p-P)\theta_{\mathrm{r}} \, d\Gamma_{\mathbf{y}} & \text{if } p > P \end{cases} \quad \textbf{3.75}$$

The delta function in eq. 3.32 has been exploited to remove the angular integral in eq. 3.49. This has sifted out the value of θ_{r} given by $\theta_{\mathrm{r}} = \mathrm{atan2}(-\widehat{\mathbf{R}}_y, -\widehat{\mathbf{R}}_x)$. $\cos\theta_{\mathbf{y}} = \widehat{\mathbf{n}}_{\mathbf{y}} \cdot \widehat{\mathbf{R}}$ has also been substituted. $V(\mathbf{x},\mathbf{y})$ is the visibility function, which again can only be non-zero if the ray path is un-occluded. But now it also requires that $\widehat{\mathbf{n}}_{\mathbf{y}} \cdot \widehat{\mathbf{R}} > 0$ and $\widehat{\mathbf{n}}_{\mathbf{x}} \cdot \widehat{\mathbf{R}} < 0$.

3.11 SUMMARY

The overall framework of the EBEM algorithm is summarised in Figure 3.17. The Galerkin BEM framework utilized for EBEM allows comparison of different basis and testing functions. EBEM is formulated with a ‘Bubnov-Galerkin’ scheme for simplicity and symmetry in basis, and synergy with high-frequency BEM . A novel aspect of EBEM is that it discretises incoming and outgoing energy separately. This is again similar to high frequency BEM. Directional point sources and receivers have also been described with Fourier series in angle.

Figure 3.17 Framework of the EBEM algorithm

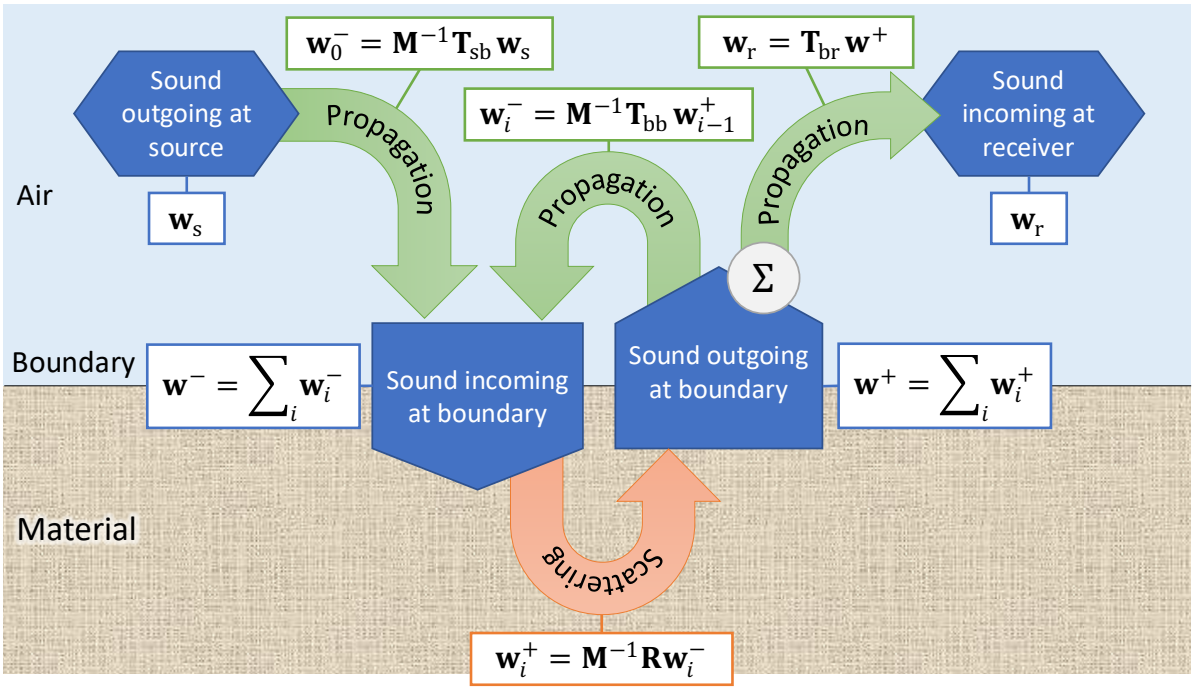

4 METHODOLOGY

This chapter is divided into three sections: selection and description of the validation model, numerical integration, and numerical implementation of EBEM. First, a brief discussion of the possible validation models is presented followed by the justification of the final choice and an overview of its specifications. This is followed by a description of the Gauss-Legendre quadrature rule used for solving the EBEM integrals. The final section in this chapter documents the process of numerically implementing EBEM.

4.1 VALIDATION MODEL

Selection of a suitable algorithm to validate EBEM against is of utmost importance. The first pre-requisite of this validation model is the capability to model high frequencies in an energy-based manner similar to EBEM. The second requirement is the capability to include directional point sources and receivers like the ones in EBEM. Finally, it is desirable to be able to make comparisons between the boundary data obtained from the two models to scrutinise the approximation in EBEM independent of source and receiver properties.

One obvious choice for the validation model would be classical Raytracing, which bears strong similarity with EBEM. But as already discussed, Raytracing requires volumetric or surface receivers, making it unsuitable to validate point receiver responses, which is the intention here. It will also be difficult to compute boundary direction maps with Raytracing.

ISM was chosen as a validation model. The IS construct can utilise the $\mathbf{T_{SR}}$ mapping function which will ease implementation and comparison with EBEM. Although ISM only models ideally specular reflections and is most accurate for modelling early reflections, it would be suitable as a validation model as the effect of the discretisation scheme in the EBEM model can be verified and compared against a solution mapping exact specular reflection paths. ISM's simplicity and flexibility in implementation allows easy inclusion of directional source and receivers as well. The ISM specification with modifications from the standard approach is presented in the next section.

4.1.1 Modified Image Source Model

A 2D ISM is used for validation. As discussed in the previous section, one of the pre-requisites for the validation algorithm is its ability to model point sources and receivers which have directionalities defined by Fourier series in angle. This would mirror the source and receiver descriptions in EBEM. To model source directivity utilising a Fourier series in angle in ISM, we first need to compute source angles for the original source in the room as well as each IS. These source and receiver angles defined in the 2D Cartesian co-ordinate system are measured with respect to the horizontal x-axis as shown in Figure 4.1. $\hat{\mathbf{x}}$ and $\hat{\mathbf{y}}$ denote the orientations of the x- and y- local coordinates at each point. **R** denotes the ray from the source to the receiver.

Figure 4.1 Computing source and receiver angles

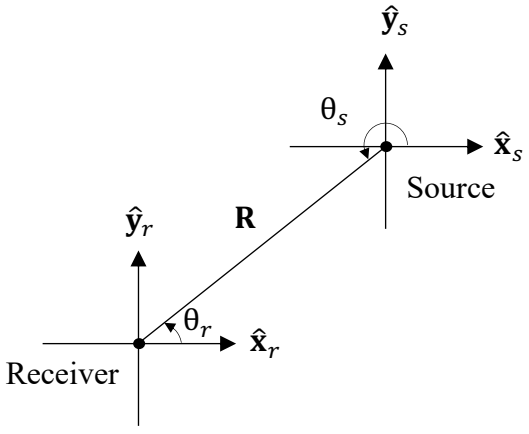

When the source in the room is mirrored against a boundary, the orientation of one of these co-ordinates is 'flipped' dependent on the coordinate direction along which the source is mirrored. This is shown in Figure 4.2.

Figure 4.2 Illustration of source co-ordinate flipping when a source is mirrored by an edge of the room

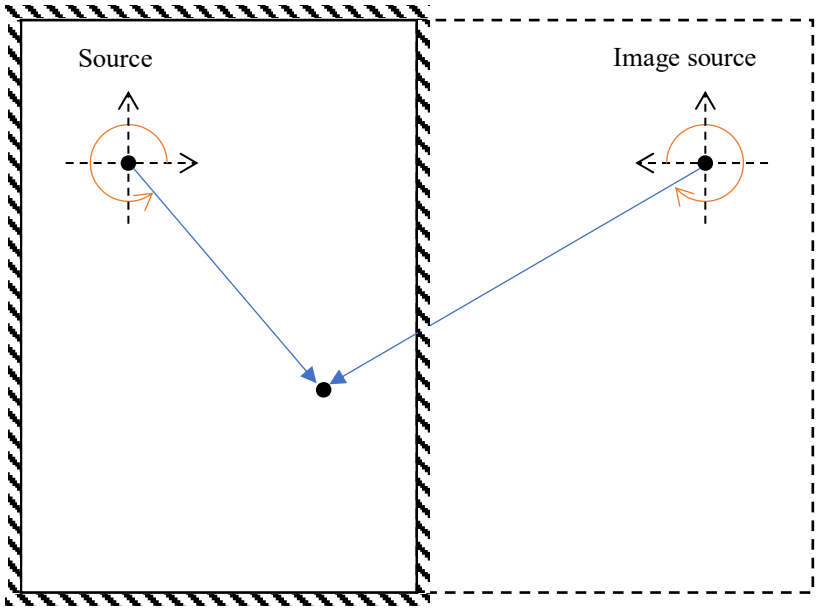

This affects the computation of source and receiver angles and must be addressed. The effect of this over two reflection orders in both x- and y- directions is shown in Figure 4.3.

Figure 4.3 Source co-ordinate angle 'flipping' with reflection order. Room shown with a solid line

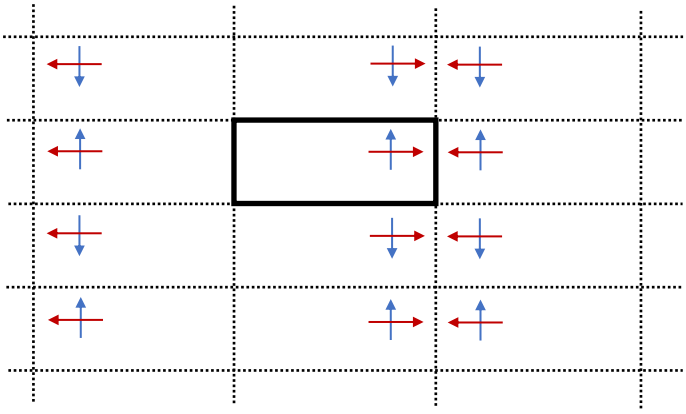

The first step in implementing an ISM is computing IS locations for a specific maximum reflection order, as a function of the room dimensions and the source location. To simplify the modelling and solution process for a rectangular room, the origin of the co-ordinate system was modelled at the centre of the room. For a rectangular room of dimensions $L_x \times L_y$ (in metres)

with the source located at $\mathbf{x}_{s,}$ the IS locations for reflection orders $\mathrm{N_x}$ and $\mathrm{N_y}$ along the defined x- and y- directions are:

$$[x_{\mathrm{IS}}\,, y_{\mathrm{IS}}] = \left[L_x\,, L_y\right] \times \left[\mathrm{N_x}\,, \mathrm{N_y}\right] + \mathbf{x}_s \times -1^{[\mathrm{N_x}\,, \mathrm{N_y}]} \qquad \textbf{4.1}$$

Due to its structure and the need for similarity between the two models, the $\mathbf{T_{SR}}$ source-to - boundary propagation process defined in the previous chapter is used to compute the power propagated from the original source and ISs to the receiver. This would also simplify application of Fourier series representation for the source and receiver directivities implemented in the EBEM algorithm.

The coordinate orientation flipping at each IS position based on reflection order is implemented by inverting the sign of the respective coordinate at the image source position. In each coordinate direction, it is observed that the respective co-ordinate orientation is 'flipped' for odd reflection orders and flips back to its original orientation (that of the source in the room) at even reflections orders. This can be achieved with a term $(-1)^{\mathrm{N}}$, which alternates between values 1 and -1 based on the value of reflection order N.

The desired coordinate flipped is this achieved by calculating the source angle with the following equation:

$$\theta_s = \mathrm{atan2}\left((-1)^{\mathrm{N_y}}\,\widehat{\mathbf{R}}\,.\,\hat{\mathbf{y}}_s, (-1)^{\mathrm{N_x}}\,\widehat{\mathbf{R}}\,.\,\hat{\mathbf{x}}_s\right) \qquad \textbf{4.2}$$

And $\theta_r = \theta_s - \pi$. Here, $(-1)^{\mathrm{N_x}}$ and $(-1)^{\mathrm{N_y}}$ implement the coordinate flipping in the x- and y- directions respectively.

Similar to EBEM, ISM assumes locally reacting boundary conditions and angle dependent absorption can be implemented. Reflection angles for a second order IS is presented in Figure 4.4. Pseudocode for the ISM algorithm is given in Figure 4.5.

Figure 4.4 Image source reflection angles

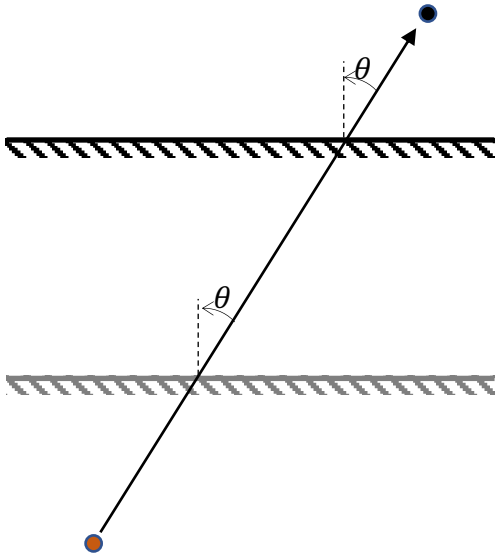

Figure 4.5 Image Source validation model pseudocode

```
for N_x in (−N,N)
 for N_y in (−N, N)
   Compute IS locations for [N_x, N_y]
   Compute ray vector R and ray length R
   Compute reflection angle θ
   Compute and square the angle-dependent Reflection coefficient R
   Compute receiver coefficients with cylindrical spreading using the T_SR process
   Total power at receiver is computed from the coefficients
```

Where:

N is the maximum reflection order to be computed up to (entered by the user)

N_x is the reflection order along the x-axis

N_y is the reflection order along the y-axis

For N_x, the negative values mean a reflection off the left wall and positive values mean a reflection off the right wall as the origin of the co-ordinate system is modelled at the centre of the room. Similarly, for N_y, negative values mean a reflection off the bottom wall and positive values mean a reflection off the top wall.

4.2 NUMERICAL INTEGRATION

An important part of numerically implementing EBEM is solving the integrals defined in the previous chapter. In numerical computing and analysis, quadrature refers to the process of computation of definite integrals. The most common approach to numerically evaluating integrals is to assume the integrand follows some family of interpolating polynomials, and then from this information find a set of evaluation 'abscissae' and corresponding scaling weights that compute the integral optimally. If these integration points (or 'abscissae') are equally spaced, it is termed as Newton-Coates quadrature, otherwise it is Gaussian Quadrature (GQ).

Commonly used numerical integration formulae, such as one based on a Taylor series with N points will exactly integrate a polynomial of degree N. It generates N number of weights for such an integration rule, and it can be chosen to satisfy N linear equations. A greater degree of accuracy for a specific amount of numerical computation can be achieved if the need to model equally spaced abscissae is ignored. This is where GQ rules excel. In general, the accuracy of integration improves with N. GQ is able to approximate the interpolation polynomial better with the same number of abscissae. Now we can represent a function with a polynomial of degree $2N-1$ as we have $2N$ equations, N for the abscissae and N for the weights.

The ray propagation processes involving the boundary, i.e., source-to-boundary, boundary-to-boundary and boundary-to-receiver processes are described with boundary integrals, so are the mass and reflectance matrices. The solution requires the integrals to be evaluated over the entire boundary. The integration quantities to construct the solution matrices typically depend on $\hat{\mathbf{t}}$ and/or $\hat{\mathbf{n}}$. As these quantities are discontinuous at the mesh nodes where μ is an integer, the boundary integrals are evaluated over each mesh element and the results are summed to obtain the boundary solution. This is described below:

$$\oint_{\Gamma} f(\mathbf{x})dl = \int_0^N f\big(\mathbf{x}(\mu)\big)\frac{dl}{d\mu}d\mu = \sum_{n=0}^{N} l_n \int_0^1 f\big(\mathbf{x}(n,\xi)\big)d\xi \qquad \textbf{4.3}$$

The latter integrals are suitable for evaluation with a GQ rule. In GQ a set of integration points and corresponding weights are determined first, and these values can be reused for numerous integration calculations, which is not possible with other quadrature rules. The sum of values of the function at the abscissae are multiplied by a corresponding weight to approximate the integral of the function in the given interval:

$$\int_{-1}^{1} f(\xi)d\xi \approx \sum_{i=0}^{I} w_i f(a_i) \qquad \textbf{4.4}$$

Where a_i are the abscissae, w_i are the weights and I is the order of the GQ rule.

These abscissae a_i are the roots of the interpolation polynomial and the weighting is used to emphasise a particular part of the integration interval than another. Orthogonal polynomials of degree N defined in an interval $[a, b]$ have N distinct zeros in the open interval (a, b). The weights are derived using the following equation:

$$w_i = \frac{2}{(1 - a_i^2)(P_n{}'(a_i))} \qquad \textbf{4.5}$$

Where $P_n{}'$ is the derivative of the interpolation Polynomial of order. To transform the computed abscissae in the range $-1 \leq \xi \leq 1$ to analogous values in an interval $a \leq \xi \leq b$, the following change of variable process can be used:

$$-1 \leq \tilde{x} \leq 1 \leftrightarrow a \leq x \leq b$$

$$\text{if} \quad \frac{\tilde{x} - (-1)}{1 - (-1)} = \frac{x - a}{b - a} \qquad \textbf{4.6}$$

$$\text{so that,} \quad x = \frac{b - a}{2}\tilde{x} + \frac{a + b}{2}$$

Therefore, eq. 4.4 can be rewritten as:

$$\begin{aligned} \int_a^b f(x)dx &= \int_{-1}^{1} f\left(\frac{b - a}{2}\tilde{x} + \frac{a + b}{2}\right)\frac{dx}{d\tilde{x}}d\tilde{x} \\ &= \int_{-1}^{1} f\left(\frac{b - a}{2}\tilde{x} + \frac{a + b}{2}\right)\frac{b - a}{2}dx \\ &= \frac{b - a}{2}\int_{-1}^{1} f\left(\frac{b - a}{2}\tilde{x} + \frac{a + b}{2}\right)d\tilde{x} \\ &\approx \frac{b - a}{2}\sum_{\mathrm{n=1}}^{\mathrm{N}} \mathrm{w_n f}\left(\frac{b - a}{2}\tilde{x}_i + \frac{\mathrm{a + b}}{2}\right) \end{aligned} \qquad \textbf{4.7}$$

This would result in the following equation for the interval $0 \leq \xi \leq 1$ which can be used to evaluate the integrals over position in EBEM:

$$\int_0^1 f(\xi)d\xi \approx \sum_{i=0}^{I} \frac{w_i}{2} f\left(\frac{1}{2} + \frac{a_i}{2}\right) \quad \textbf{4.8}$$

The theory behind choosing the abscissae is rooted in Legendre polynomials, and forms a subset of GQ called Gauss-Legendre Quadrature (GLQ). Roots of Legendre polynomials are real and distinct in the open interval $(-1, 1)$. For the integration rule described in the previous section, the associated polynomials are Legendre Polynomials in this case, $P_n(x)$, with the n-th polynomial normalised to give $P_n(1) = 1$. The n-th Gauss-Legendre quadrature abscissae is the n-th root of $P_n(x)$ and the weights are calculated as:

$$w_n = \frac{2}{1 - x_n^2[P_n'(x_n)]^2} \quad \textbf{4.9}$$

Legendre Polynomials form an orthogonal system over the interval $[-1,1]$ with a weighting function of $w(x) = 1$. For two Legendre Polynomials with degrees n and m:

$$\int_{-1}^{1} P_n(x)\, P_m(x)\, dx = \frac{2}{2n+1}\delta_{mn} \quad \textbf{4.10}$$

Where δ_{mn} is the Kronecker delta. Because of the stated properties of Legendre polynomials, the GQ estimation of the integral of $P(x)$ is exact as long as the order of $P(x)$ is up to $2N + 1$.

4.3 Numerical Implementation

This section documents the process of numerically implementing the EBEM algorithm.

4.3.1 Geometry and Boundary Element mesh

The geometry and boundary element mesh are implemented in the codebase as classes. As we are working in 2D, boundary elements will be 1D line elements. Only straight-line elements are considered for this study. A solution domain represented by a surface is bounded by a set of linear elements with these elements bounded by a set of end vertices. The boundary mesh is defined by an ordered set of element nodes, with position along the boundary defined with the

dimensionless parameter μ locally and their Cartesian coordinates defined globally. The mesh element length and number of degrees of freedom for each element are specified when creating the mesh object and are stored as internal parameters to streamline DOF handling.

Figure 4.6 Schematic of a line segment and line loop objects and methods of parametrising local position on both

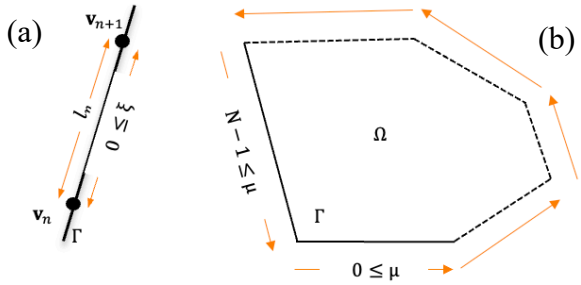

4.3.2 Solution matrices

Once the boundary mesh is built, the $\mathbf{T_{sb}}$, $\mathbf{T_{bb}}$, $\mathbf{T_{br}}$, $\mathbf{T_{sr}}$, $\mathbf{M}$ and $\mathbf{R}$ matrices are built in a pre-computation stage before the solver section of the algorithm numerically implements the discretised form of EBEM following the algorithm structure in Section 3.3. The boundary integrals implementing the various acoustic propagation process are evaluated in the form of functions which evaluate their discretised form.

The Gauss-Legendre quadrature scheme is used as default when using Legendre, Chebyshev or Lobatto but a uniform quadrature rule more suitable for PWC is also implemented. Suitable abscissae are also provided for PWL basis in angle. The spatial quadrature order is by default set to 5 and were integrated over the interval [0,1]. All of the EBEM boundary integrals are over position on the boundary, but $\mathbf{M}$ and $\mathbf{R}$ involve angular integrals over $[-1,1]$.

The spatial basis implemented in the codebase is PWC. The codebase has been developed so the angular basis function type can be provided as an argument to the function calls. This can be:

1. Legendre polynomials
2. Chebyshev polynomials
3. Lobatto polynomials
4. Discontinuous PWC functions
5. Continuous PWL functions

4.3.3 Implementation stages

The EBEM numerical implementation is performed in three stages:

4.3.3.1 Pre-computation stage

1. Compute source-to boundary mapping matrix $\mathbf{T_{br}}$ using eq. 3.63
2. Compute mass matrix **M** using eq. 3.60
3. Compute Reflectance matrix **R** using eq. 3.65
4. Compute Boundary to boundary mapping matrix $\mathbf{T_{bb}}$ using eq. 3.67
5. Compute source to receiver mapping matrix $\mathbf{T_{sr}}$ using eq. 3.69
6. Compute boundary to receiver mapping matrix $\mathbf{T_{br}}$ **using** eq. 3.75

4.3.3.2 Solution stage

1. The coefficients for direct source to receiver propagation is computed as $\mathbf{T_{sr}w_s}$. This is the zeroth order reflection.
2. The incoming boundary projections for first order reflection are computed as $\mathbf{T_{sb}w_s}$
3. The corresponding incoming boundary weights are computed as $\mathbf{w_1^- = M^{-1}T_{sb}w_s}$
4. The outgoing boundary weights are computed as $\mathbf{w_1^+ = M^{-1}Rw_1^-}$
5. The incoming boundary projections for second order reflection are computed as $\mathbf{T_{bb}w_1^+}$
6. The corresponding second order incoming boundary weights are computed as $\mathbf{w_2^- = M^{-1}T_{bb}w_1^+}$
7. The corresponding outgoing boundary weights are computed as $\mathbf{M^{-1}Rw_2^-}$
8. Reflections can be advanced by matrix multiplications by repeating steps 5 and 6.

4.3.3.3 Receiver response

1. Once the boundary solution is computed for a required number of reflection orders i, receiver coefficients $\mathbf{w_r}$ are computed by multiplying the outgoing weights at the final reflection order with the boundary to receiver mapping matrix $\mathbf{T_{br}}$.
2. Source to receiver direct propagation coefficients for direct sound are computed with $\mathbf{T_{sr}}$.
3. Omnidirectional power at receiver in W/m can now be computed by $2\pi\mathbf{w_r}[0]$, where $\mathbf{w_r}[0]$ is the omnidirectional term (at index zero) in the vector of receiver coefficients $\mathbf{w_r}$.

5 RESULTS

This chapter presents the results originating from the numerical implementation of the model discussed in the previous chapter. The main aim of this chapter is to compare EBEM results against their ISM equivalent and validate the codebase, and the formulation itself.

First, validation was done for direct sound from the source to the receiver, which verifies the point source and receiver models and directivities. To verify the solution matrices that map incident and reflected power to and from the boundary, receiver directivity for early reflections is presented. To study the effect of the boundary mesh on the solution accuracy, a mesh convergence study was performed.

An important feature of the developed EBEM algorithm is the ability of the codebase to readily change the angular basis functions, so their effect on accuracy and convergence can be studied. The effect of these is studied by examining boundary power distributions for different choices in angular basis functions. Finally, the power decay in the room was studied with reflection order and the steady state solution is obtained and verified. Together, this set of verification procedures validate the proposed EBEM formulation rigorously and provide valuable insight into its approximation and limitations.

5.1 TEST GEOMETRY AND SPECIFICATIONS

Because this version of the EBEM does not implement diffraction, the validation case was limited to a rectangular room. This also meant that the visibility function discussed in the previous chapter has the value 1 in all cases, with all non-coplanar points on the boundary visible to each other. A rectangular room of dimensions $4m \times 5m$ was simulated for verification. The centre of the room was modelled to be at the origin of the 2D Cartesian co-ordinate system to simplify coding of the Image Source Method. The source was located at $[-1, -0.5]$ and the receiver at $[1, 1]$. The room geometry, source and receiver locations and direct ray from the source to the receiver is shown in the Figure 5.1.

Figure 5.1 Test room geometry with source and receiver locations

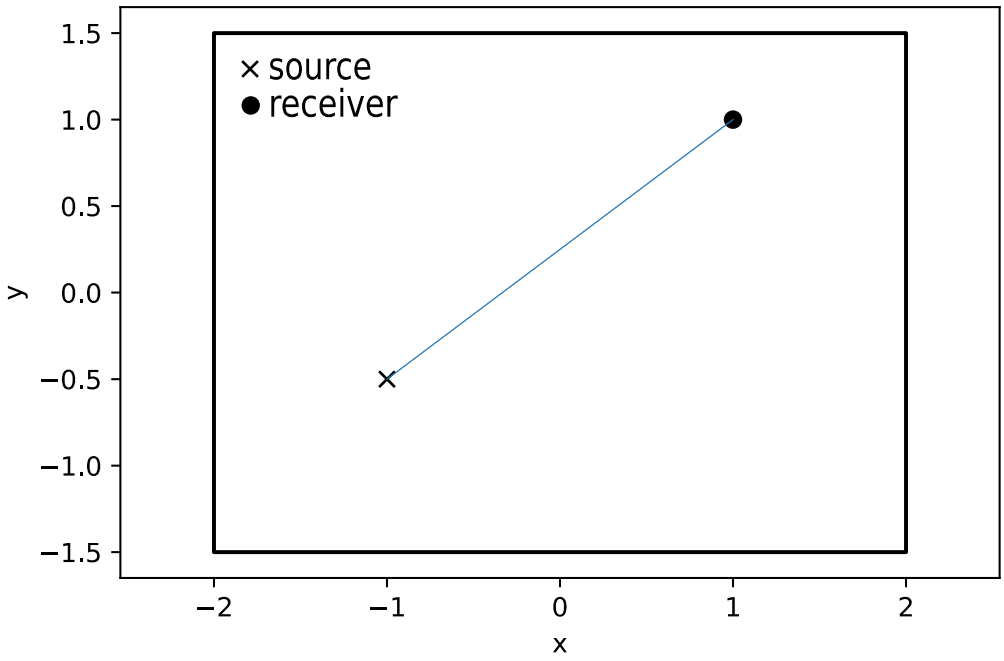

Source and receiver directives of arbitrary order were defined. A source of order 3 was defined with $a_0 = a_1 = a_2 = 1, a_3 = 1/2,$ and all $b_q = 0$, and a receiver of order 5 was defined for results presented in this section, unless stated otherwise. A polar plot of the source directivity pattern defined is presented in Figure 5.2.

Figure 5.2 Source directivity polar plot

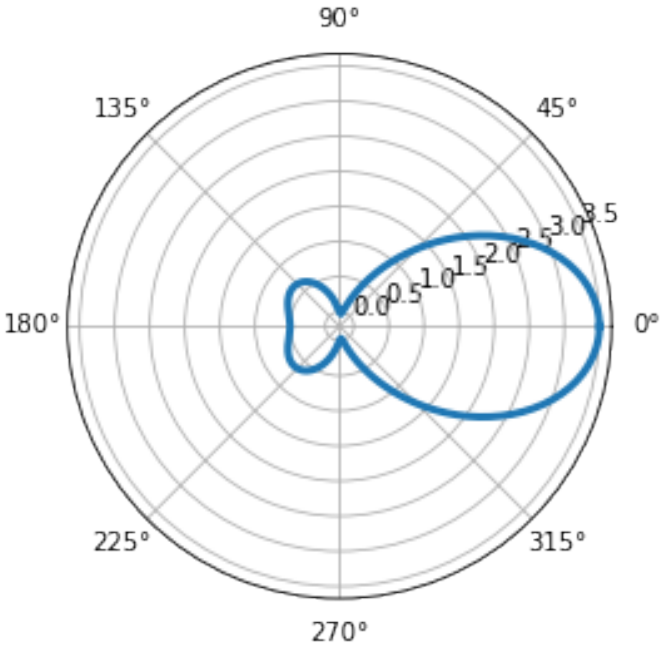

To implement and study the discretised version of the EBEM model, a 2D Boundary Element mesh was constructed with a maximum element size of $0.25\ m$ and $Q = 17$, the latter dictating the order of angular discretisation. This leads to a system with $N = 56$ elements and a total of 952 DOF. The meshed test room is shown in Figure 5.3.

Figure 5.3 Meshed test room

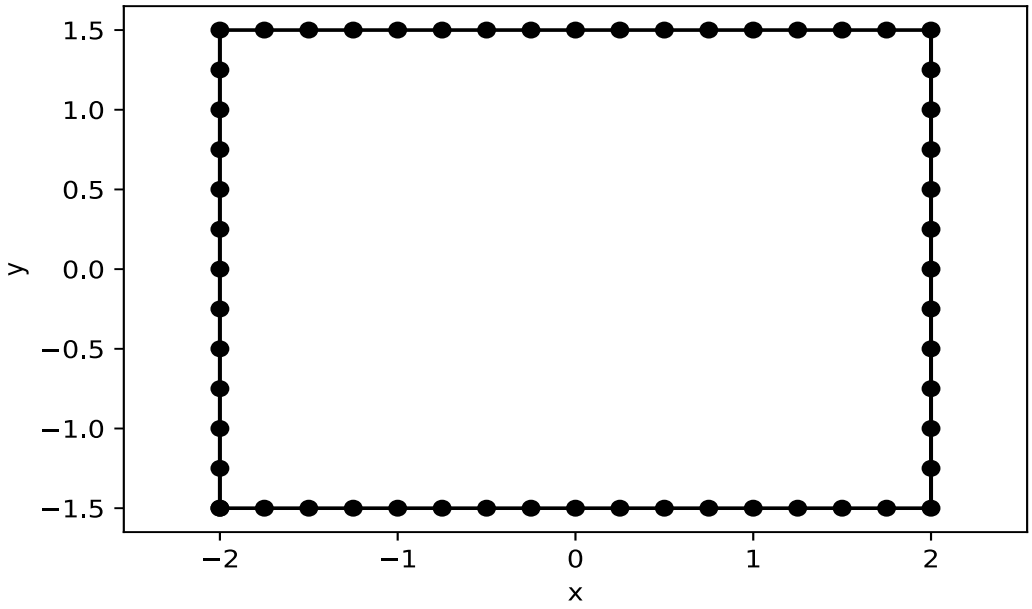

5.2 DIRECT SOUND

The zeroth order reflection, i.e., the direct sound from the source to the receiver, is presented in Figure 5.4. This sheds light on both source and receiver directivity models and verifies accurate mapping of incident power at the point receiver with arrival angle, independent of the mesh. The direct power propagated to the receiver (of order 5) is presented in Figure 5.4. It is evident that the main lobe in the polar plot points towards the source as expected. The direct power received from the source was $0.762\ W/m$. This is the expected value accounting for cylindrical spreading from the source to receiver, over a distance of $2.5\ m$.

Figure 5.4 Zeroth order response (direct sound) at receiver

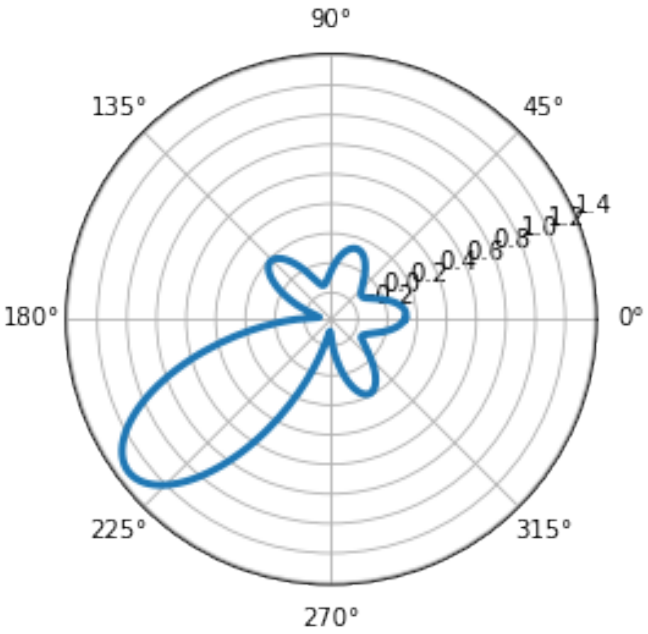

The polar directivity pattern for direct sound for receiver orders 0, 1, 3 and 8 are shown in Figure 5.5. The width of the main lobe decreases with order as expected, with the direct power received being mapped accurately with the direct ray from the source to the receiver.

Figure 5.5 Zeroth order receiver polar plots for order (a) 0, (b) 1, (c) 3 and (d) 8

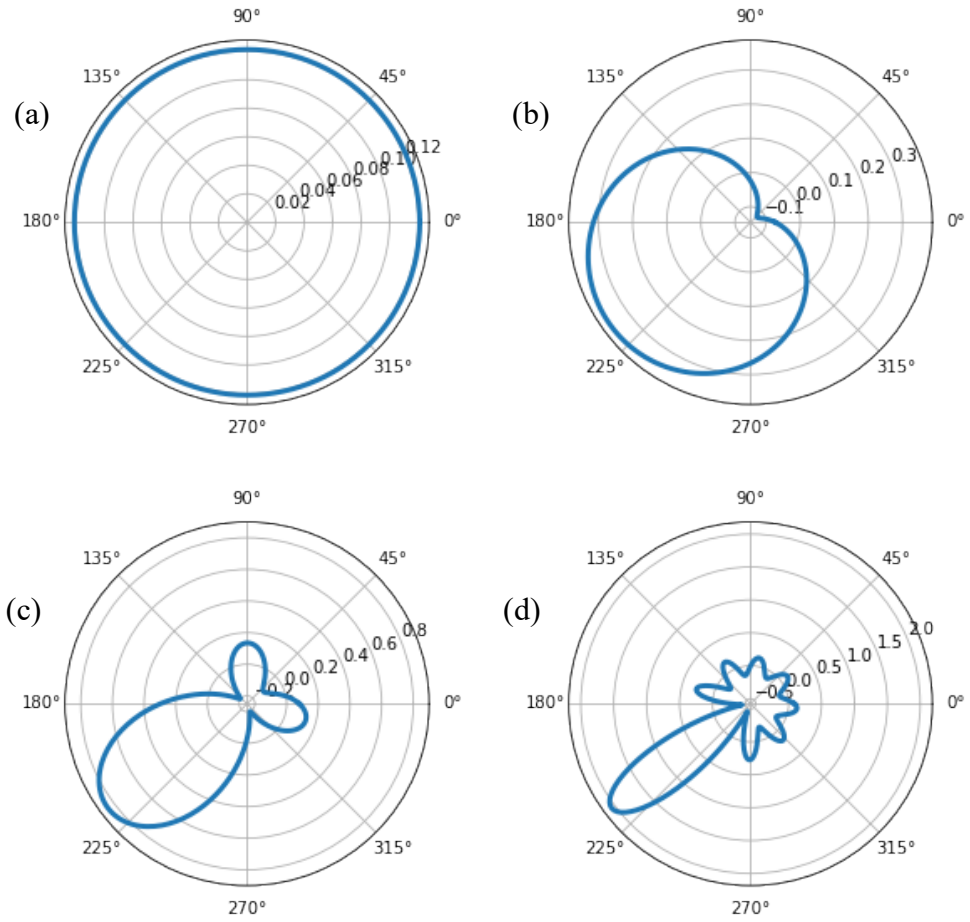

5.3 RECEIVED POWER DIRECTIVITY

This section presents the receiver directivity patterns for first and second order reflections. In Figure 5.6 these are presented for the different angular basis schemes and compared to ISM results. Although the EBEM was aimed at modelling the late-time diffuse part of room impulse responses – contrary to early reflections, which tend to be highly directional – analysing early reflections will validate the source-to-boundary, boundary-to-receiver and boundary-to-boundary propagation processes. These results are produced for rigid boundary conditions, i.e., no absorption or scattering is included. They also show how well EBEM performs when modelling early reflections with high degrees of angular discretisation.

Figure 5.6 Received power directivity for: (a) first order reflection, (b) second order reflection

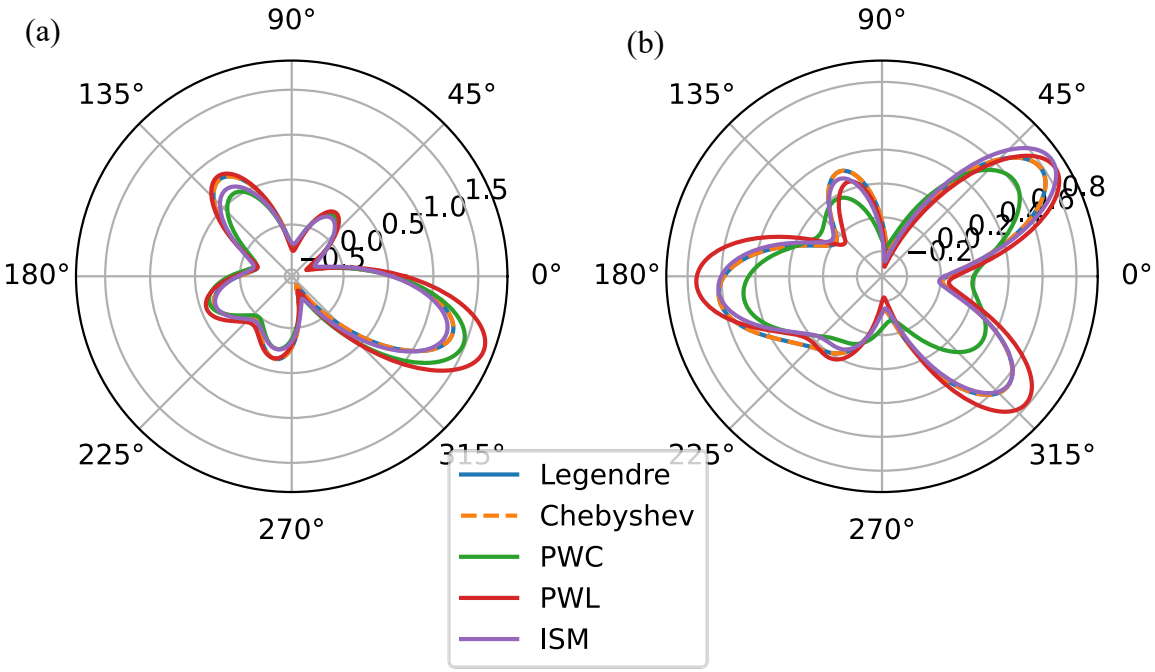

All the discretisation schemes show correlation with the ISM results. The Legendre and Chebyshev schemes show identical directivity patterns to reported precision for both first and second order reflections and closely match the ISM results. Even with their discontinuous nature, PWC functions show good correlation with first and second order ISM results. On close observation, closer correlation can be seen for the first order than the second. This is expected, since more approximation is introduced with each reflection order. With continuous polynomials such as Legendre or Chebyshev as angular basis functions, error in total power (zeroth order directivity/omnidirectional) was 0.1% for first order reflections and 4.4% for second order reflection. For the PWL scheme, the errors were 0.6% and 4.7%.The error for the PWC scheme was found to be the highest at 4.5% and 18.8% respectively.

5.4 Power Distribution on the Boundary

To provide insight into the boundary data structure caused by the reflection angle mapping and interpolation, the boundary power distribution is studied. This takes the form $w(\mu, \chi)$. But

it is important to first describe the reflection angle mapping process and resulting plots to completely understand the effect of differing choices in basis functions contributing to the boundary distribution. This is explained for both EBEM and ISM before the plots are presented.

Consider the rectangular room in Figure 5.8. Three different rays originating from the source and being reflected at the lower edge of the room are shown.

Figure 5.8 Reflection of a source from a boundary: layout of source, receiver and connecting rays in a room

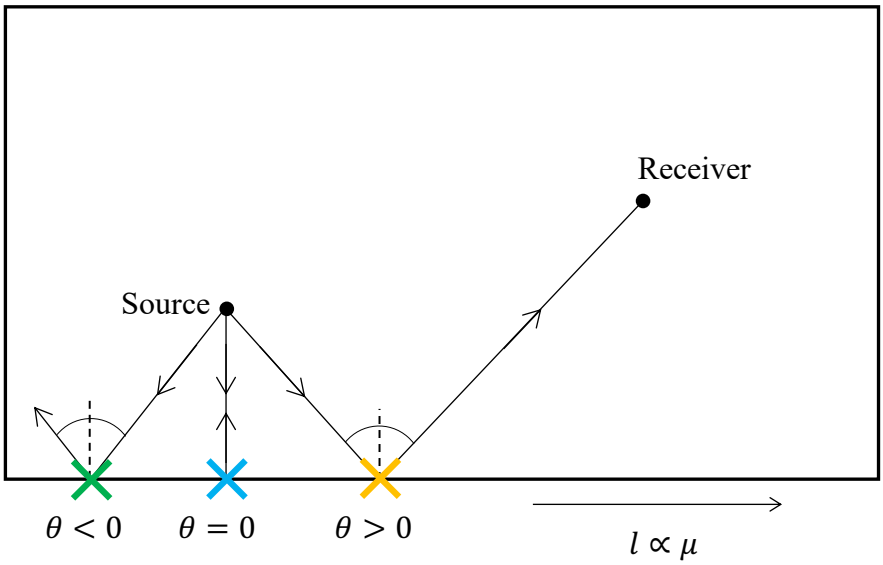

The ray incident at the green cross is reflected at a negative angle θ relative to the boundary normal vector. The ray incident at the blue cross is incident normal to the boundary, making a zero-degree reflection angle. Finally, the ray reflected at the yellow cross to the receiver makes a positive angle with the boundary.

The boundary distribution plot easiest to explain the reflection angle mapping process is with a plot utilizing PWC functions as basis functions in both space and angle. Now the boundary power distribution will be discontinuous in both space and angle. This is shown in Figure 5.9. The x-axis here represents position along the lower edge of the room. With a maximum element length of $0.25m$, the lower edge of the test room with a length of $4m$ will have 16 elements, shown by the x-axis tick values. The y-axis depicts the boundary tangential co-ordinate χ parametrising reflection angle. The reflection angle can be in the range $-\pi/2 \leq \theta \leq \pi/2$ on the boundary, so χ on the boundary will be in the range $-1 \leq \chi \leq 1$.

Figure 5.9 Projection of the angles in Figure 5.8 onto boundary space with PWC spatial and angular basis

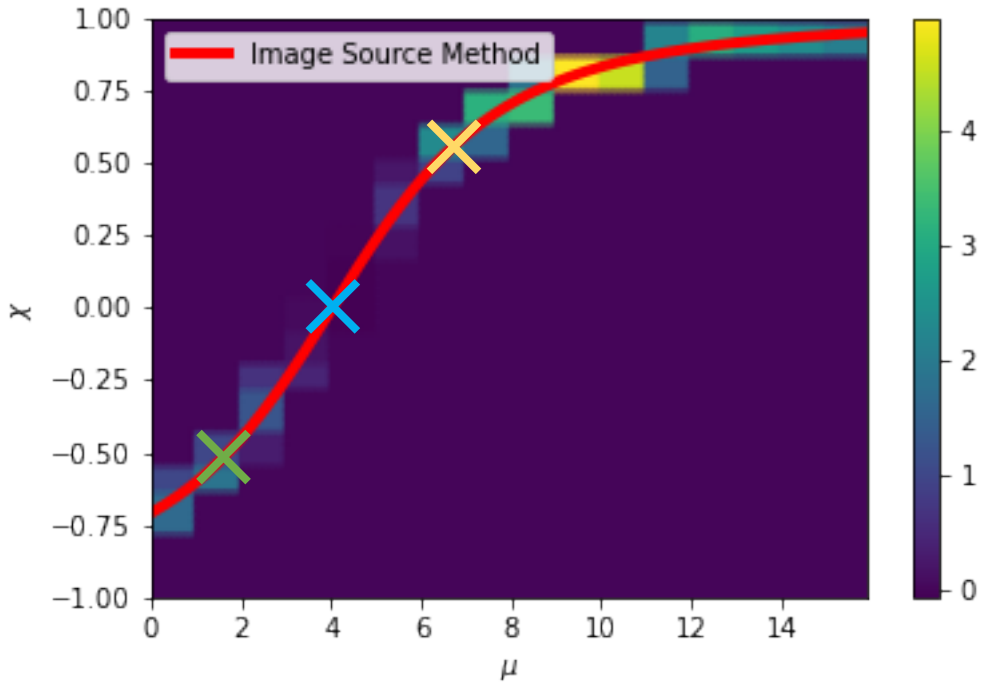

In addition to the rays shown in Figure 5.8, the source radiates rays in every direction, arriving at the all the points on the boundary. Evaluating the reflection for each point on the lower edge of the room yields the red line in Figure 5.9 from ISM. This is the loci of the ray arrival direction from the source. It can be noted that the yellow, blue, and green crosses for the three reflection angles shown in Figure 5.8 fall on this red line. The EBEM power distribution follows this trend too, the only anomaly being the fading out around $\chi \approx 0$, which is due to the source directivity chosen – this position lines up with the null of the directivity pattern shown in Figure 5.2. In the plots the that follow, this effect can be seen on the lower and upper edges of the room, but is missing from the left and right edges, as there is no null facing those edges. Power is being radiated towards these edges.

Figure 5.10, Figure 5.11, and Figure 5.12 present the boundary power distribution plots for all four edges of the room using PWC, PWL and Legendre polynomials respectively as angular basis functions. This is starting from the lower edge in anti-clockwise direction. Each of these plots are generated with PWC basis in space.

Figure 5.10 Boundary power distribution plots for all four edges of the room with PWC basis in space and angle

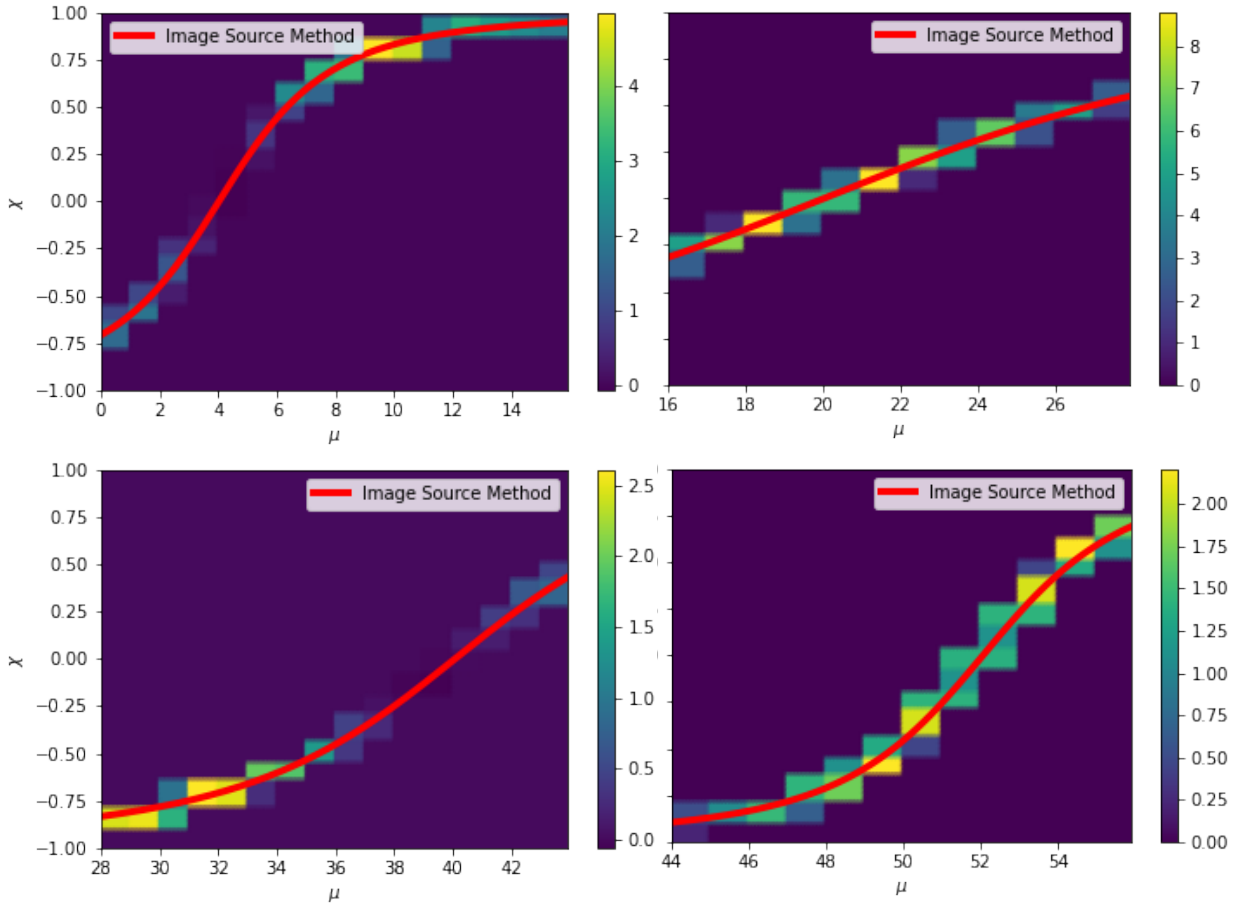

Using PWC functions for interpolating space and angle makes the boundary solution completely discontinuous in both as observed in Figure 5.10. This leads to a 2D 'faceting' of the boundary data into rectangular blocks as observed in Figure 5.9 in (μ, χ) space. It is seen the reflection angles, and hence the power on the boundary on the boundary is smudged across these rectangles. This shows approximation in both position and direction.

Figure 5.11 Boundary power distribution plots for all four edges of the room with PWL as angular basis and PWC basis in space

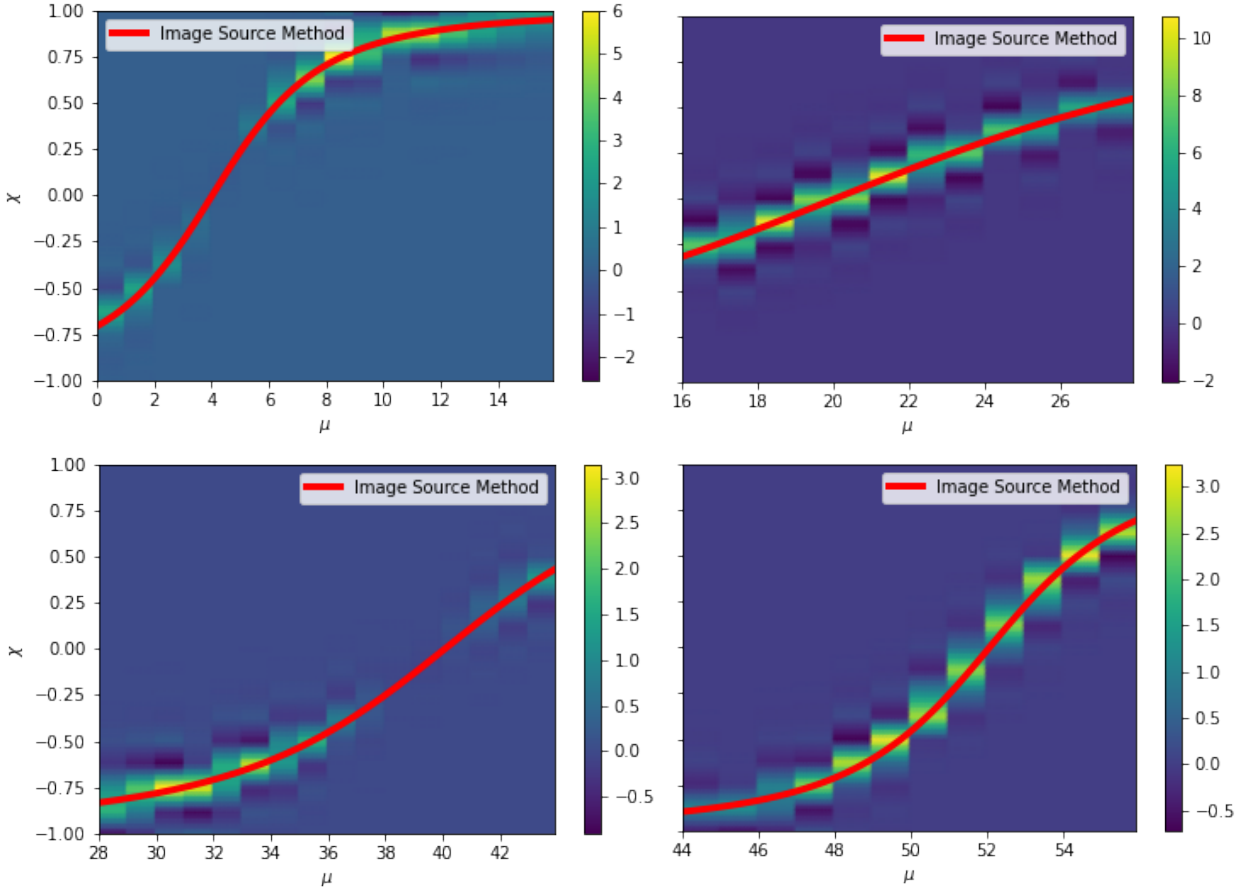

PWL basis in angle results in continuous non-smooth stripes over the angular range. The peaks of the polynomials are observed to line up with the ISM results as you can see in Figure 5.11.

Figure 5.12 Boundary power distribution plots for all four edges of the room with Legendre polynomials as angular basis and PWC basis in space

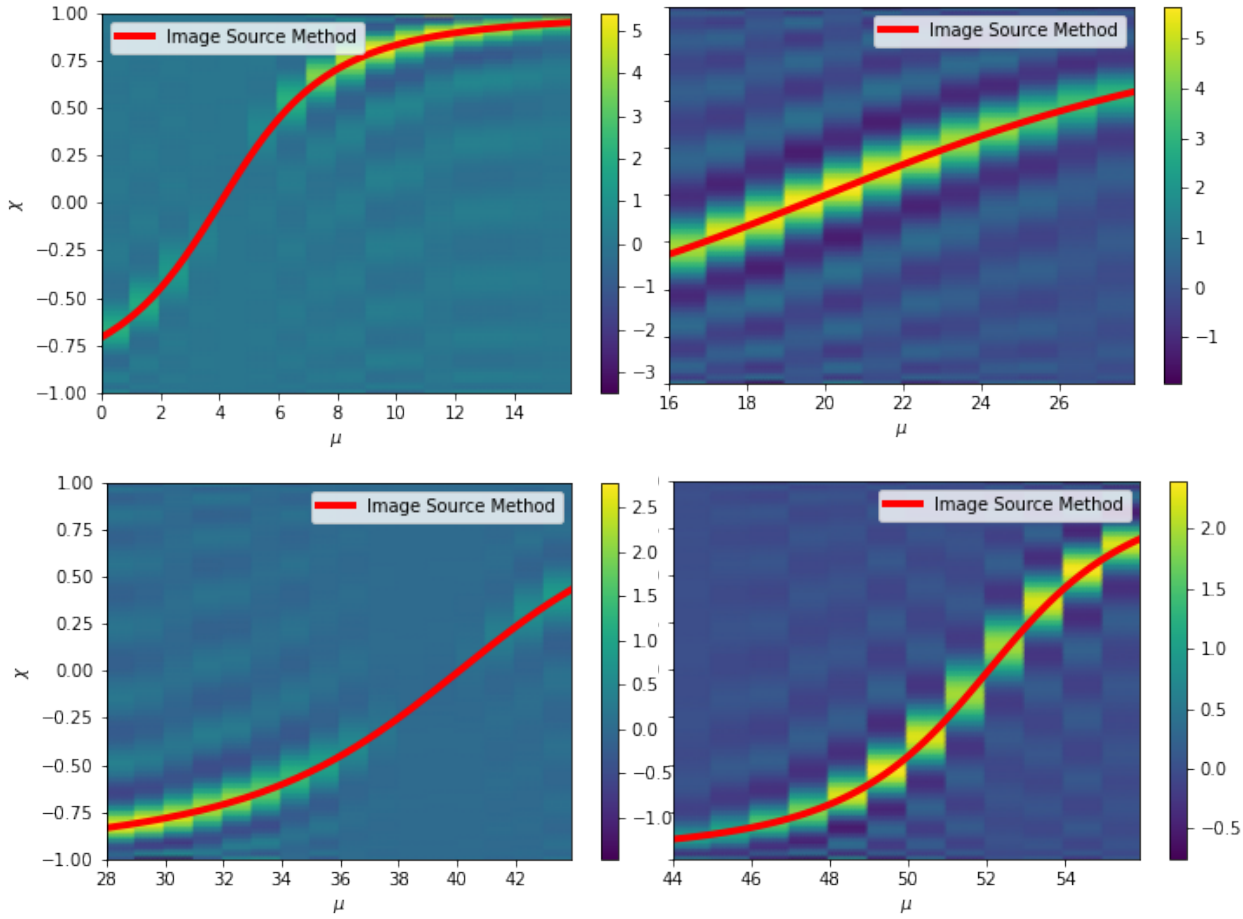

As Legendre, Chebyshev and Lobatto are continuous orthogonal polynomials, they result in smooth stripes over each DOF. Side lobing in χ is also observed for Legendre, Chebyshev and Lobatto which is typical of orthogonal polynomials. This is absent for PWL (Figure 5.11) as expected as these functions are continuous over the range of χ, but they are not smooth. But the peak of the distribution originating from these angular interpolation functions are observed to be aligned with the red line in each case, showing these peak power distributions are at the expected angular range with position on the boundary. Different peak values observed for different schemes are attributed to the differing 'smudging' present in the different schemes.

5.5 Mesh convergence study

To investigate the effect of the Boundary Element mesh on the solution accuracy, a mesh convergence study was performed. The spatial resolution was increased by decreasing the maximum element size allowed, while the angular basis order was varied by changing Q (the

number of DOFs per mesh element). Together, these illustrate if and how the EBEM and ISM solutions converge and the dependence of this on the angular basis function used. Following the study of power directivities at the receiver earlier in this chapter, the convergence study was performed for first and second order reflections. Convergence was quantified based on two error metrics:

1. **Normalised Power Error**: The error in total received power versus ISM. This is the metric used for the error values presented in Section 5.3. It presents the error in power arriving at the receiver independent of arrival angle.
2. **Normalised Root Mean Squared (RMS) Error**: The RMS error calculated over all receiver coefficients (order ≥ 0), versus those computed with ISM.

The normalised power error is for a zeroth order receiver response, i.e. irrespective of arrival direction (omnidirectional), and normalised Root Mean Squared error is computed over all the receiver coefficients. This would be the directional error when sense with a receiver of order 5. In both cases, normalisation was performed using the ISM value.

5.5.1 Convergence with increasing Degrees of Freedom

Figure 5.13 shows the error plots for first and second order reflections when the maximum mesh element size was fixed at $0.2m$ and Q was increased from 1 to 20 (or 2 to 20 for PWL).

Figure 5.13 Mesh convergence plots: (a) Normalised power error and (b) RMS error for varying Q from 1 to 20 and fixed element size of 0.2m

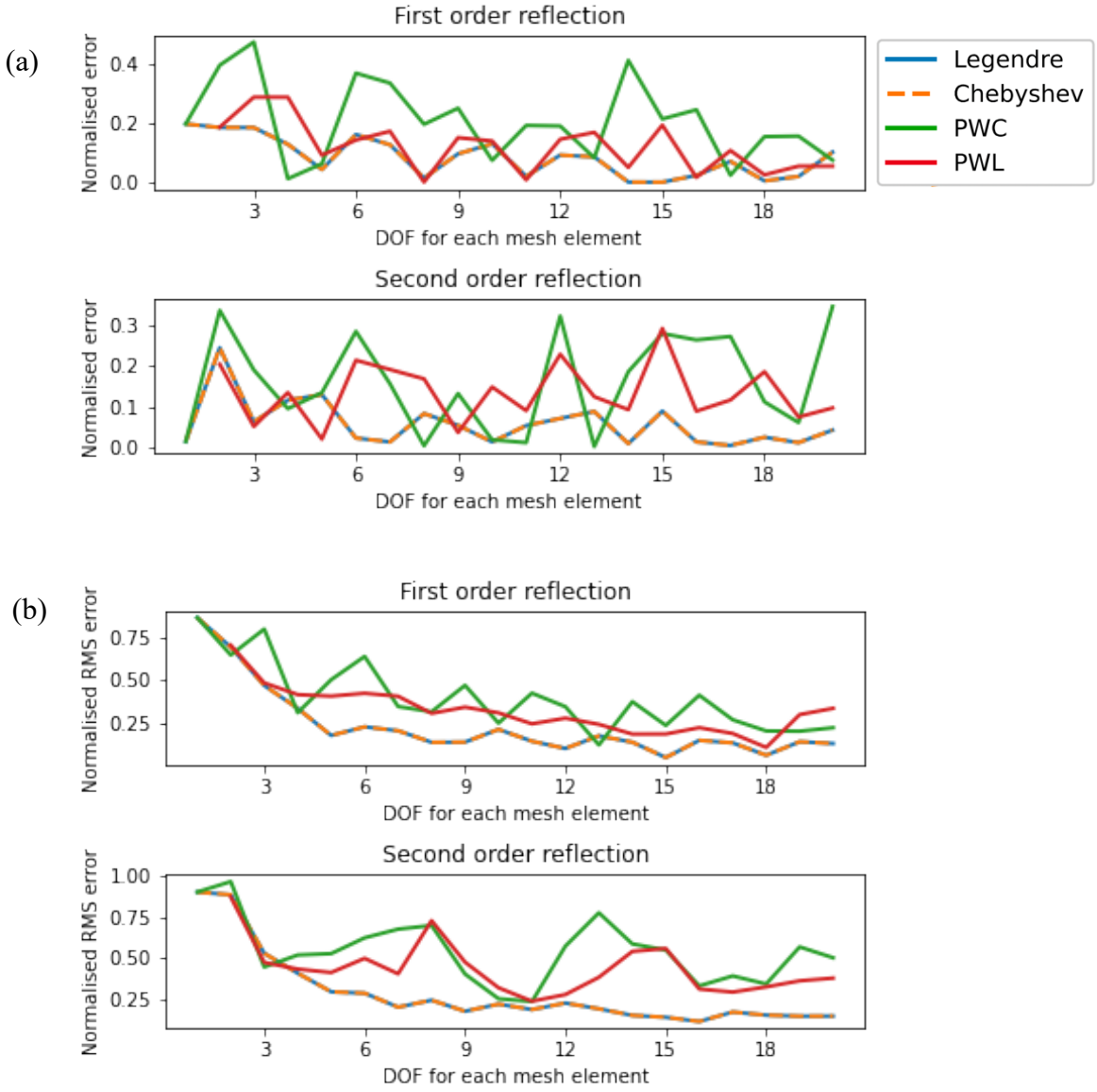

The order of the angular basis functions is dictated by Q, the number of DOFs for the mesh element. Higher values for Q will result in higher polynomial orders in angle, resulting in better accuracy. When the convergence study was performed for the varying DOFs for each element, we see expected trends. The Legendre and Chebyshev (and Lobatto, which is not shown on the plot) results are again identical and shows a clear convergence trend with increasing Q for both first and second order reflections.

From Figure 5.13 it is clear that both omnidirectional and directional error values decrease with increase in number of DOFs and decreasing mesh element sizes. We see alternating areas of higher and lower error values in both plots with increasing DOF per element. Higher error values are observed in both cases at low Q values. This is particularly evident in the directional

(RMS) results. 'Bands' of high error values are observed in the directional results at low values of Q from 1 to 5 irrespective of the maximum mesh element length.

5.5.2 Convergence with decreasing mesh element size

Figure 5.14 presents similar error plots when Q was fixed at 20 and the maximum mesh element size was varied from $0.1m$ to $1m$.

Figure 5.14 Mesh convergence plots: (a) Normalised power error and (b) RMS error for varying element size from 0.1m to 1m and fixed Q=20

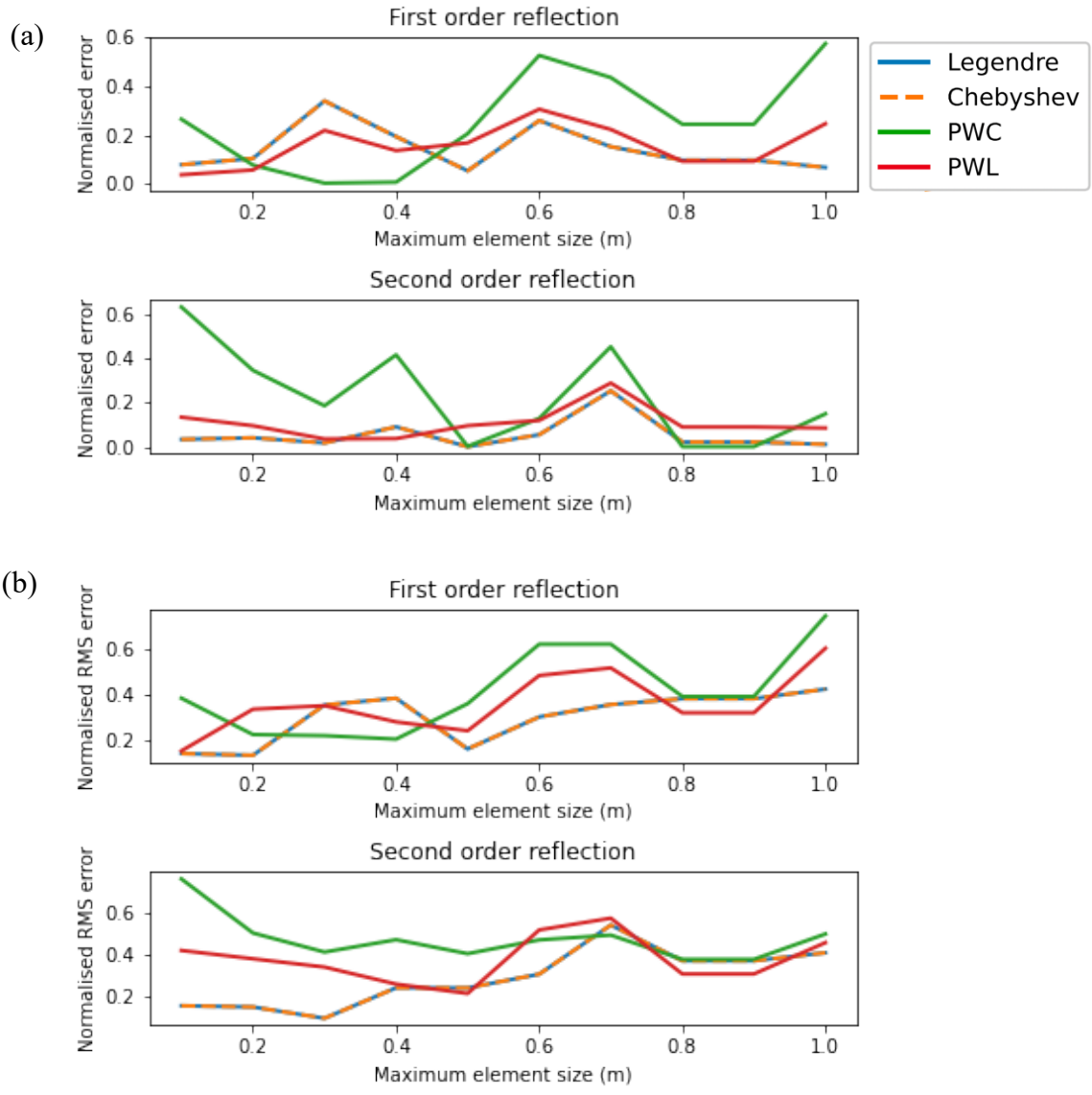

Smaller element sizes lead to more elements in the mesh and smaller beams of power being reflected from the boundary, reducing the extent of approximation present. The first and second order error plots show clear convergence with the directional results (normalised RMS error) with decreasing element sizes. The element sizes although are seen to have a fairly weak effect

on the solution accuracy. This is more evident with the directional results in Figure 5.13. This is the normalised RMS error over the receiver coefficients. A similar trend is observed for the normalised error in total omni-dictional received power, but a weaker trend nonetheless. In contrast, PWC and PWL functions exhibit significant error values in all the cases presented here

5.6 POWER DECAY IN THE ROOM

Perhaps the single most subjectively important metric in Room Acoustics is Reverberation Time. In EBEM, that amounts to studying the power decay in the room with increasing reflection order. Results are presented for three different values of normalised boundary admittance Y_n. The power decay curves are as expected. Higher values of normalised boundary admittance results in faster decay of sound in the room. The EBEM results presented in this section were computed with Legendre polynomials as angular basis.

Figure 5.15 Comparison of EBEM and ISM decay curves for different values of normalised boundary admittance, in (a) linear scale, (b) logarithmic scale

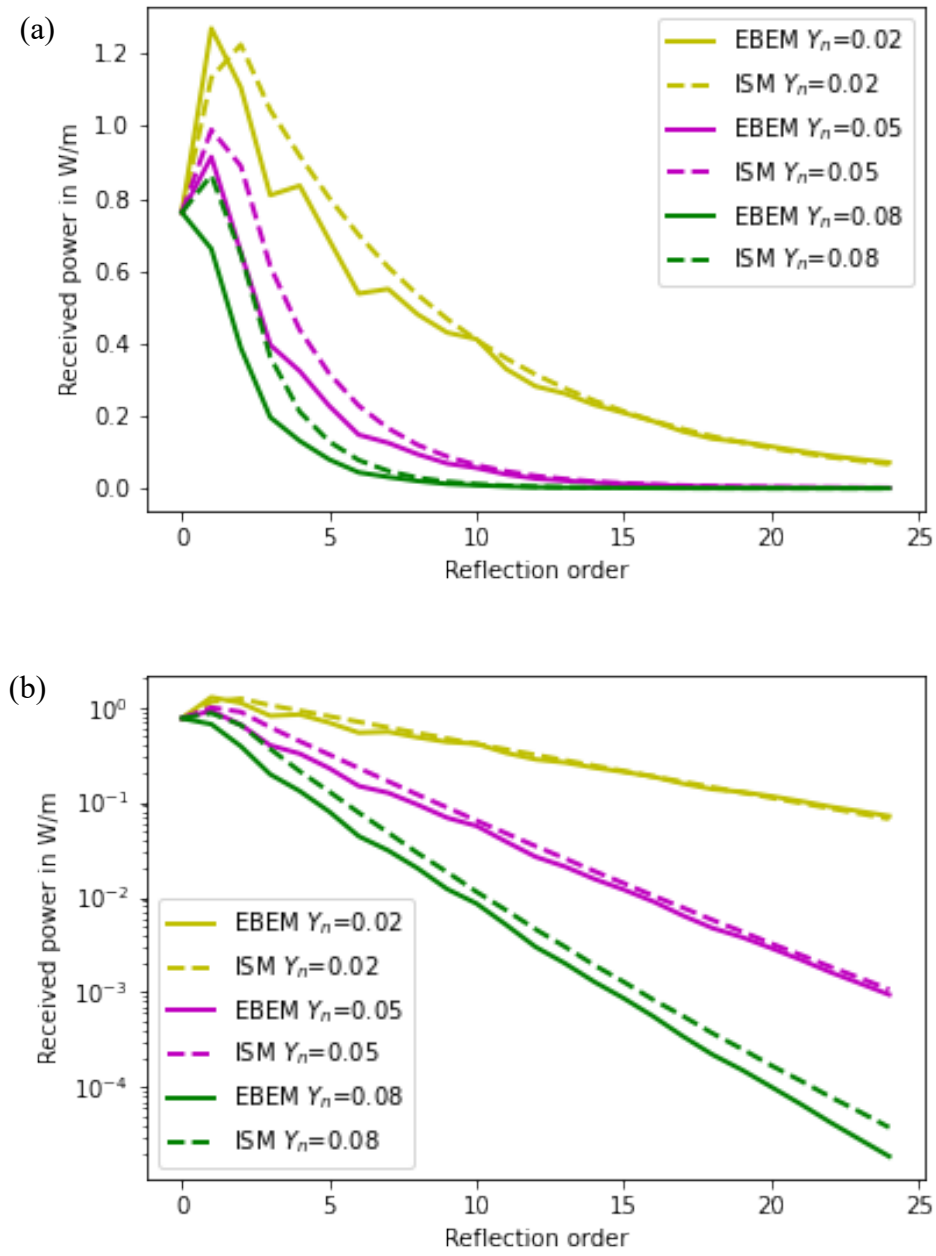

5.7 STEADY STATE SOLUTION

The steady state power distribution for EBEM can be computed in one step via a Neumann series. The EBEM results presented in this section were computed with Legendre polynomials

as angular basis. The incoming boundary weights for power mapped direct from the source are given by:

$$\mathbf{w_0^-} = \mathbf{M^{-1}T_{sb}w_s} \tag{5.1}$$

And the corresponding outgoing weights are:

$$\mathbf{w_0^+} = \mathbf{M^{-1}Rw_0^-} = \mathbf{M^{-1}RM^{-1}T_{sb}w_s} \tag{5.2}$$

For the next reflection order, the incoming weights are:

$$\mathbf{w_1^-} = \mathbf{M^{-1}T_{bb}w_0^+} = \mathbf{M^{-1}T_{bb}M^{-1}RM^{-1}T_{sb}w_s} \tag{5.3}$$

And the corresponding outgoing weights being:

$$\mathbf{w_1^+} = \mathbf{M^{-1}Rw_1^-} = \mathbf{M^{-1}RM^{-1}T_{bb}M^{-1}RM^{-1}T_{bb}w_s} \tag{5.4}$$

The steady state is the sum of these boundary weights over reflection order. This can be recognised as a Neuman series with the form:

$$\mathbf{w_\infty^+} = \sum_{r=0}^{\infty} [\mathbf{M^{-1}RM^{-1}T_{bb}}]^r \, \mathbf{M^{-1}RM^{-1}T_{sb}w_s} \tag{5.5}$$

The solution to this can be found by:

$$\mathbf{w_\infty^+} = [\mathbf{I} - \mathbf{M^{-1}RM^{-1}T_{BB}}]^{-1} \, \mathbf{M^{-1}RM^{-1}T_{SB}w_s} \tag{5.6}$$

For validating this steady state power distribution solution, EBEM and ISM results were obtained by marching on in reflection order, with power received at each reflection order added to the response. These results are shown in Figure 5.16, and the steady state power computed using eq. 5.6 is overlaid. The EBEM results are seen to converge very well with the steady state-solution while ISM is seen to produce results with are $0.3\,W/m$ more than the EBEM solution.

Figure 5.16 Comparison of steady state solution for EBEM computed via a Neumann series compared against the incremental response at the receiver with reflection order for EBEM and ISM

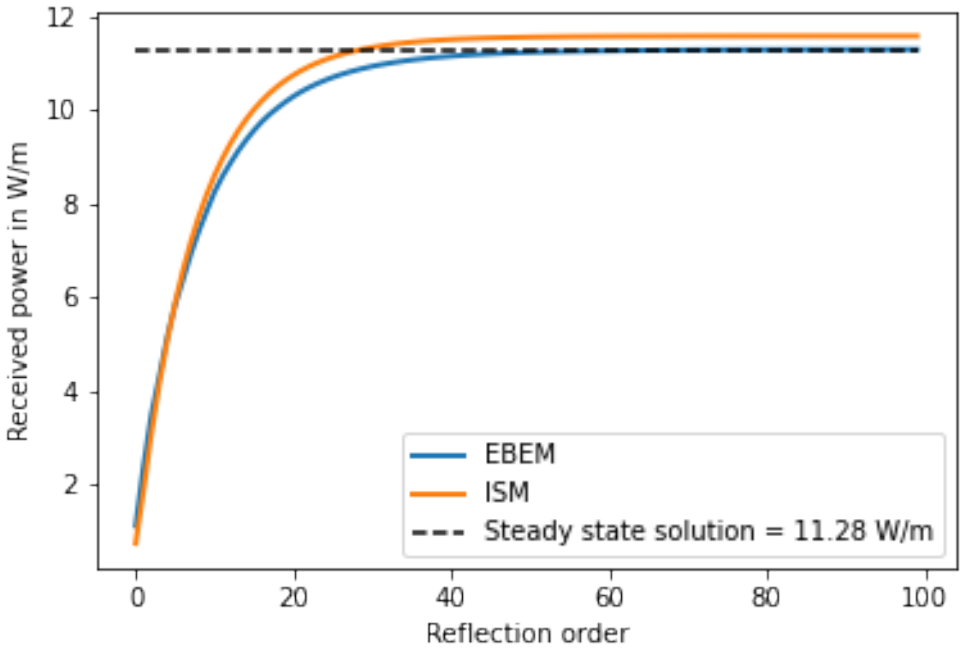

5.8 VALIDATING ANGLE DEPENDENT ABSORPTION

Although the results in sections 5.6 and 5.7 validate boundary absorption implemented with the Reflection matrix **R**, validation of directional absorption requires further studies. To validate angle-based absorption, the first order reflection from a source to receiver via a single edge of the room is studied. Source and receiver directivities are modelled to be omni-directional and their locations were arranged in a semi-circular manner as shown. The first order reflected power received is studied for 50 different pairs of source and receiver locations as shown.

Figure 5.17 Test room geometry, mesh nodes, source, and receiver locations for validating angular absorption

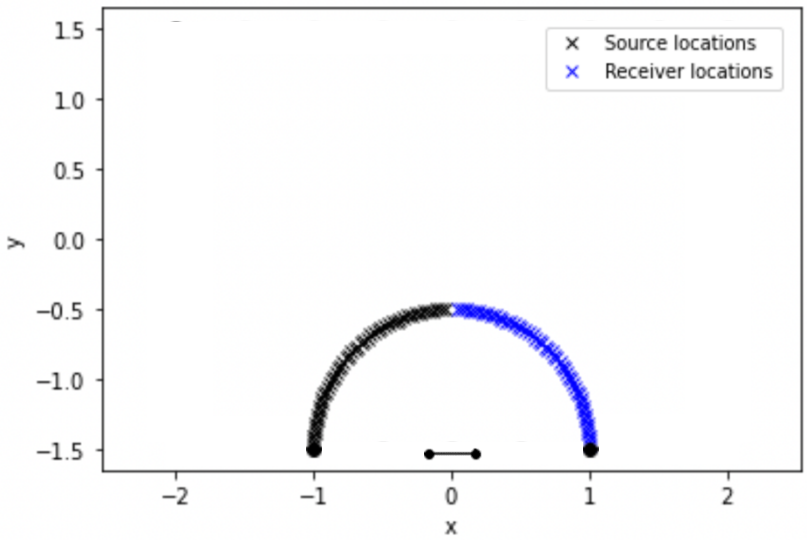

The angle of reflection for each source-receiver combination is also noted. The same procedure was repeated with ISM and the results of received power vs angle of reflection is presented in this section shows the variation in power received vs reflection angle for different maximum element sizes in the mesh. The DOF for each element Q was kept constant at 17 for the results in Figure 5.18 for Legendre polynomials. This is again compared to the ISM result depicted by the dashed line. The variation in the received power is seen to be at it most for larger element sizes. Although effect of element sizes is seen to be weaker as the reflection angle approaches 90°.

Figure 5.18 Variation of angular absorption with varying maximum element size (solid lines) for Legendre polynomials compared to ISM results (dashed line)

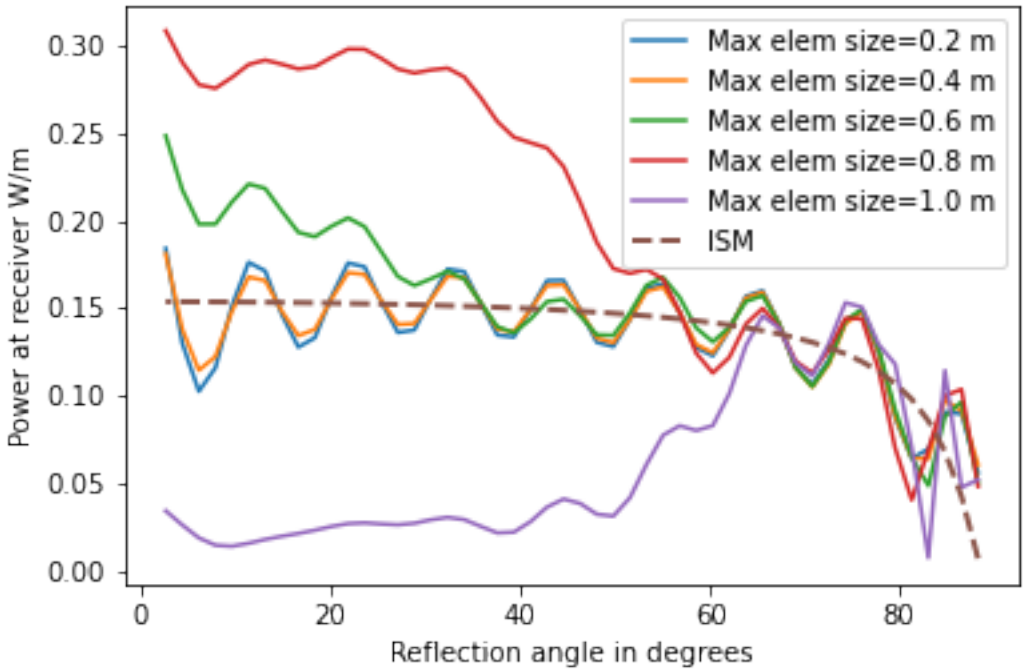

Figure 5.19 shows the variation in received power for different values of Q for Legendre polynomials. As Q dictates the order of the interpolation polynomial used, it is observed that the angular dependency modelled increases with Q. The results agree more closely with ISM at higher values of Q.

Figure 5.19 Variation of angular absorption with varying DOF for each element, Q (solid lines) for Legendre polynomials compared to ISM results (dashed line)

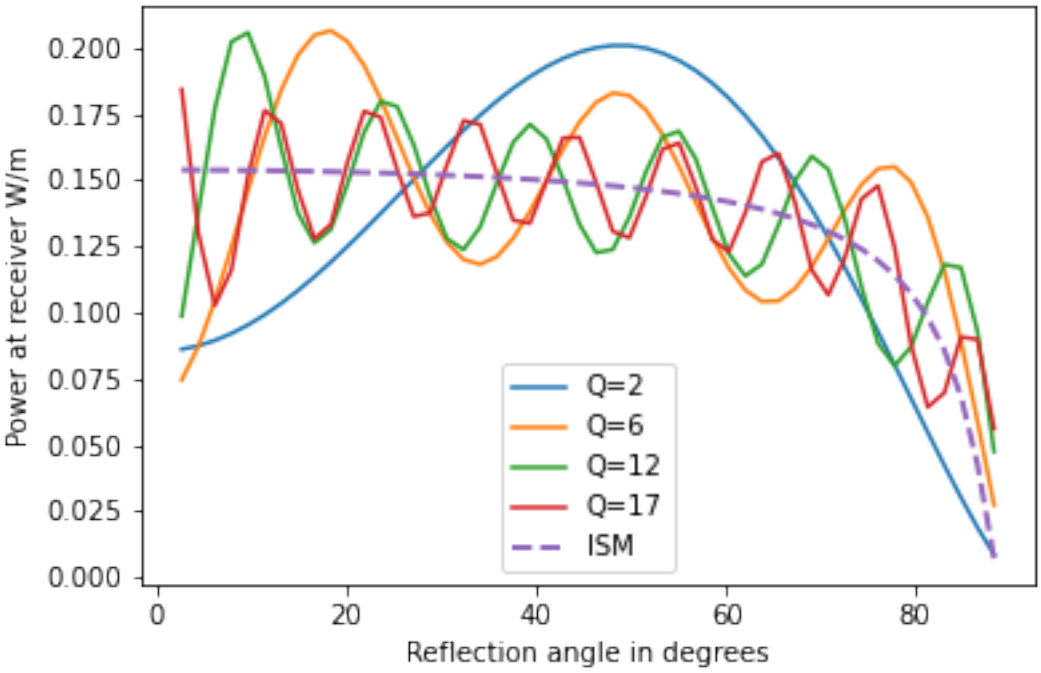

It is also important to study the polynomial fit achieved by the angular basis functions in interpolating the values of the angle dependent reflection coefficient. Figure 5.20 presents this for locally reacting boundaries that EBEM models. The residual in interpolation was found to be 1.9×10^{-14} for Local reaction with Legendre as interpolation polynomials.

Figure 5.20 Polynomial fits achieved for Local reaction Reflection coefficients with Legendre polynomials

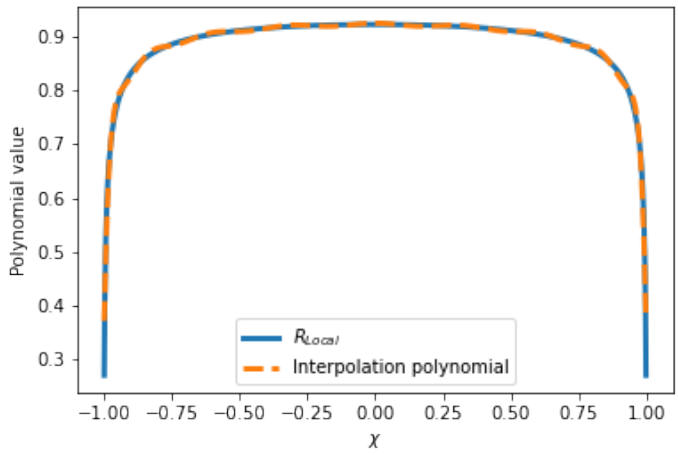

The RMS error in polynomial fit for increasing Q from 2 to 20 is shown for different angular basis functions in Figure 5.21. The RMS error decreases for all choices of angular basis functions with increasing Q. Legendre and Chebyshev provide the best fit and exhibit the smallest error as Q increases.

Figure 5.21 RMS error in polynomial fits achieved for Local and Extended reaction Reflection coefficients with increasing Q for different angular basis functions

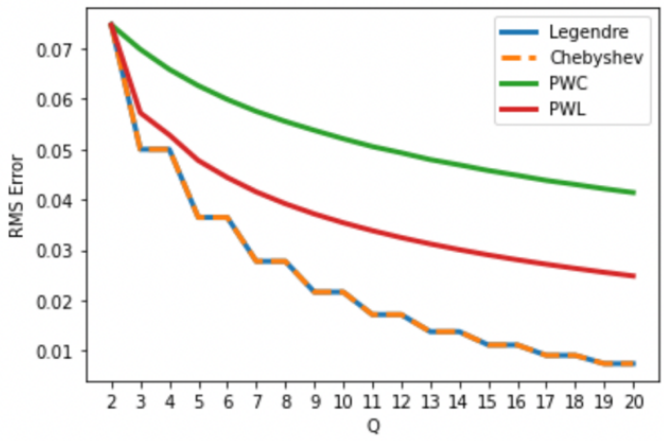

6 DISCUSSION & ANALYSIS

This chapter discusses the results from the validation study presented in the previous chapter. Important aspects of the EBEM formulation such as the extent of approximation, integration accuracy and effect of different angular basis functions are studied and discussed.

6.1 EFFECT OF DIFFERENT ANGULAR BASIS SCHEMES

The effect of different angular interpolation functions on the results presented in the previous chapter is discussed in this section.

6.1.1 On the boundary power distribution

Boundary power distribution on the lower edge of the test room is compared for PWC, PWL and Legendre polynomials as angular basis are shown in Section 5.4. The effect of discontinuous vs continuous basis in angle can be clearly observed

These results show sound diffusion at the boundary. Although we lose the high resolution of specular reflection paths that reflection-path-based GA models (the red line), these diffuse reflections are appropriate for modelling the late-time sound field when individual reflections are no longer perceptually distinguishable. Different polynomials exhibit varying degrees of energy smudging on the boundary as observed.

The orders of angular basis functions are dictated by Q, the number of DOFs per mesh element. This directly influences the accuracy of the solution along with mesh element sizes. A higher value of Q and smaller element sizes result in lesser degrees of approximation in the boundary power distributions, with smaller 'pixels' in (μ, χ) space, agreeing more with the ISM results. Figure 6.1 show examples of boundary power distributions for PWC scheme with increasing Q and N values.

Figure 6.1 Power distribution with PWC angular basis with (a) Q=10, N=22 (b) Q=17, N=56 (c) Q=30, N=140

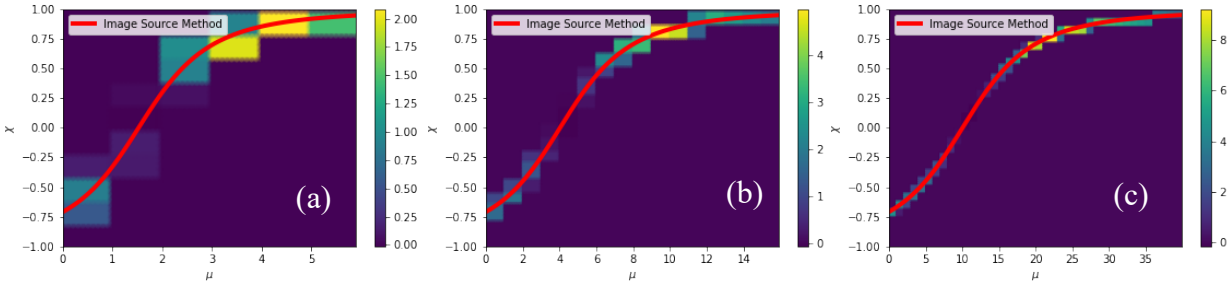

6.1.2 On convergence

The mesh convergence study examines how the EBEM solution is affected by the size of the boundary mesh elements and the DOF for each of these elements.

Contour RMS and power error plots for PWC and Legendre scheme are shown below. Although we observe fluctuation in accuracy, the error values for a specific basis polynomial order or maximum mesh element size are observed to be higher for PWC when compared to the Legendre scheme. These plots agree the observations in the previous section, with no clear evidence of convergence observed with PWC, even at very small element sizes and higher order families of PWC functions used for discretising angle.

Figure 6.2 (a) RMS error and (b) Power error contour plots for PWC basis in angle

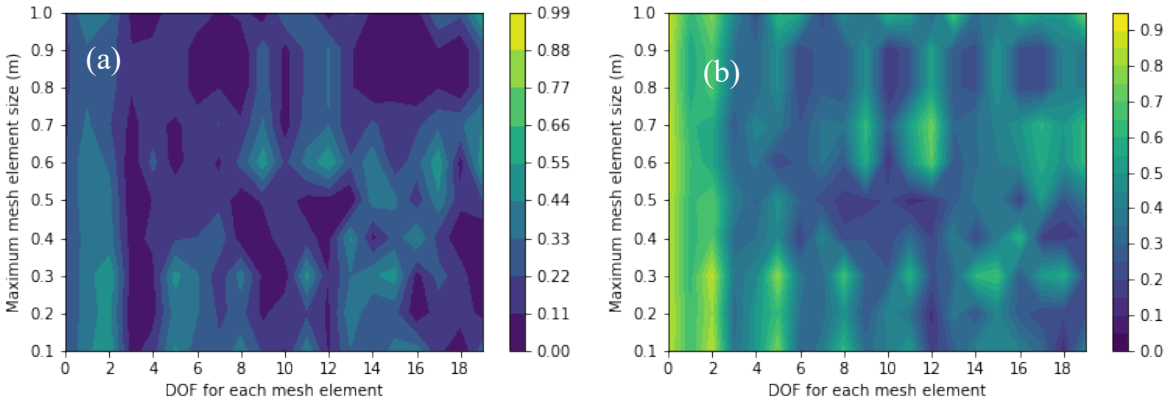

Figure 6.3 (a) RMS error and (b) Power error contour plots for Legendre basis in angle

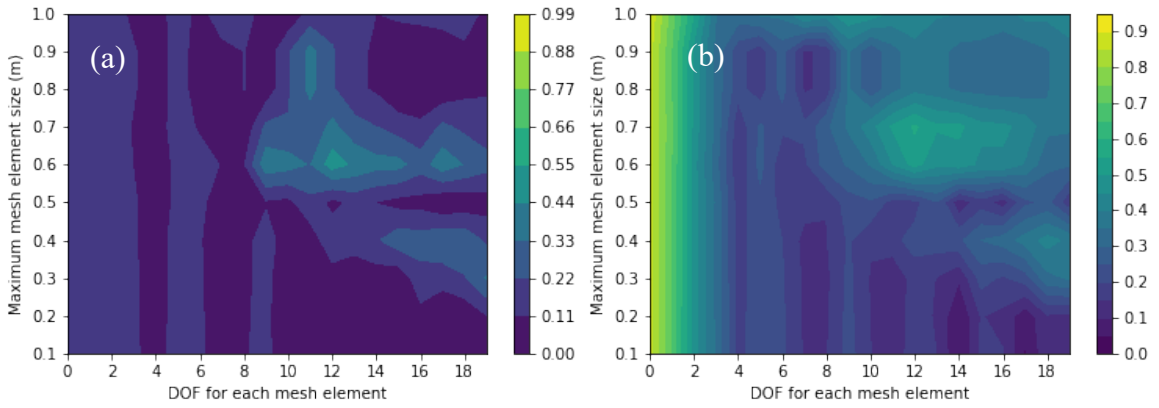

6.2 EARLY REFLECTIONS

Examining the received power directivities for early reflections not only illustrates how the EBEM formulation performs for early reflections and the effect each angular basis scheme, but also validates all the acoustic propagation processes. The first order reflection results would validate the source-to-boundary mapping matrix $\mathbf{T_{sb}}$ and the boundary-to-receiver mapping matrix $\mathbf{T_{br}}$. The second order reflection would also validate the boundary-to-boundary interaction matrix $\mathbf{T_{bb}}$.

PWC scheme shows very good accuracy for first order reflections with a zeroth order total power error of 4.5% but exhibits a greater degree of approximation for the second order reflection with a corresponding error of 18.8% which is significant. Similar errors for first and

second order reflections for Legendre and Chebyshev schemes were 0.1% and 4.4% respectively.

It is immediately obvious from the polar plots in Section 5.3 that the EBEM solution for Legendre and Chebyshev schemes are (and also Lobatto which is not shown here) in very good agreement with the ISM results for both first and second order reflections. More importantly, these continuous orthogonal polynomials exhibit identical results for both first and second order reflections to the reported precision. This aligns with the findings of the Nottingham group in 2018 [53] where "tests conducted with Chebyshev polynomials did not lead to any qualitative differences in the numerical results", but differs from their discussion in 2013 where they reported that low-order approximations with Chebyshev polynomials were very poor [15]. It is to be noted that these papers treat different models, which explain their different findings – [53] includes an additional diffusive term making the boundary integral operators compact, which is missing from [15].

The DOFs per mesh element (Q) is seen to have relatively little effect on total power at the receiver, which is consistent with success of the Radiosity model for this purpose. But Q has a strong effect on the directivity at the receiver. This is an aspect that high fidelity methods such as ISM captures well, and the EBEM formulation does too, at high angular resolution. A gradual transition between these two cases is seen as Q is increased. This demonstrates the Nottingham group's claim that DEA interpolates between low fidelity methods, which is SEA in their work and Radiosity for boundary to boundary scheme such as EBEM and high fidelity methods, like Raytracing or ISM.

As all choices of continuous orthogonal polynomials as angular basis yield identical results here. The mass matrix structure overcomes superficial differences in interpolation and allows all these continuous orthogonal schemes to perform identically. The mass matrices for all three continuous orthogonal polynomials as angular basis is shown below:

Figure 6.4 Mass matrices for (a) Legendre (b) Chebyshev and (c) Lobatto polynomial as angular basis

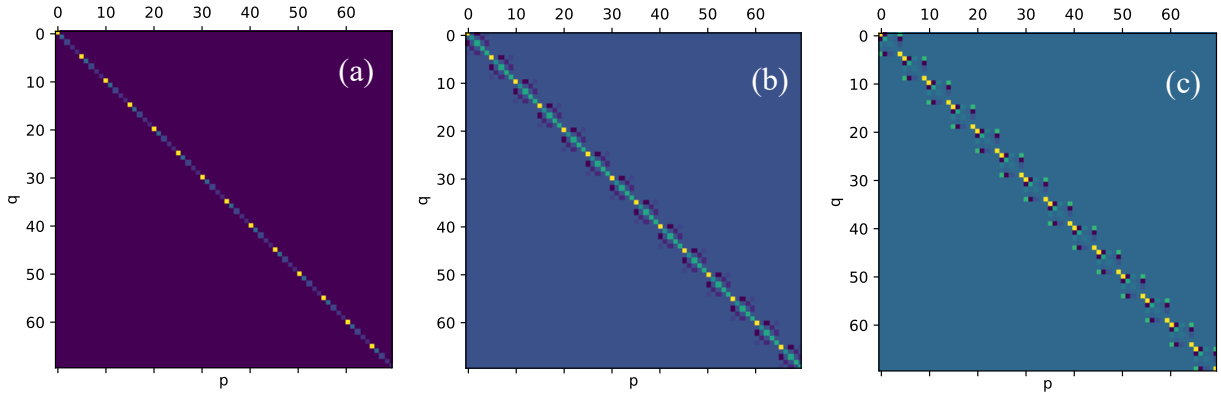

It is evident from these plots that all three continuous polynomials construct different mass matrices and will produce independent solutions, with the Legendre scheme resulting in a diagonal matrix with Chebyshev and Lobatto schemes including non-diagonal schemes arising from how the discretisation scheme is set up.

The conditioning numbers of the mass matrices used in this study is shown below for all possible choices of angular basis function. The conditioning numbers are seen to be 40 or below. All mass matrices are hence seen to be highly sparse and readily invertible.

Figure 6.5 Conditioning numbers for mass matrices with different basis schemes

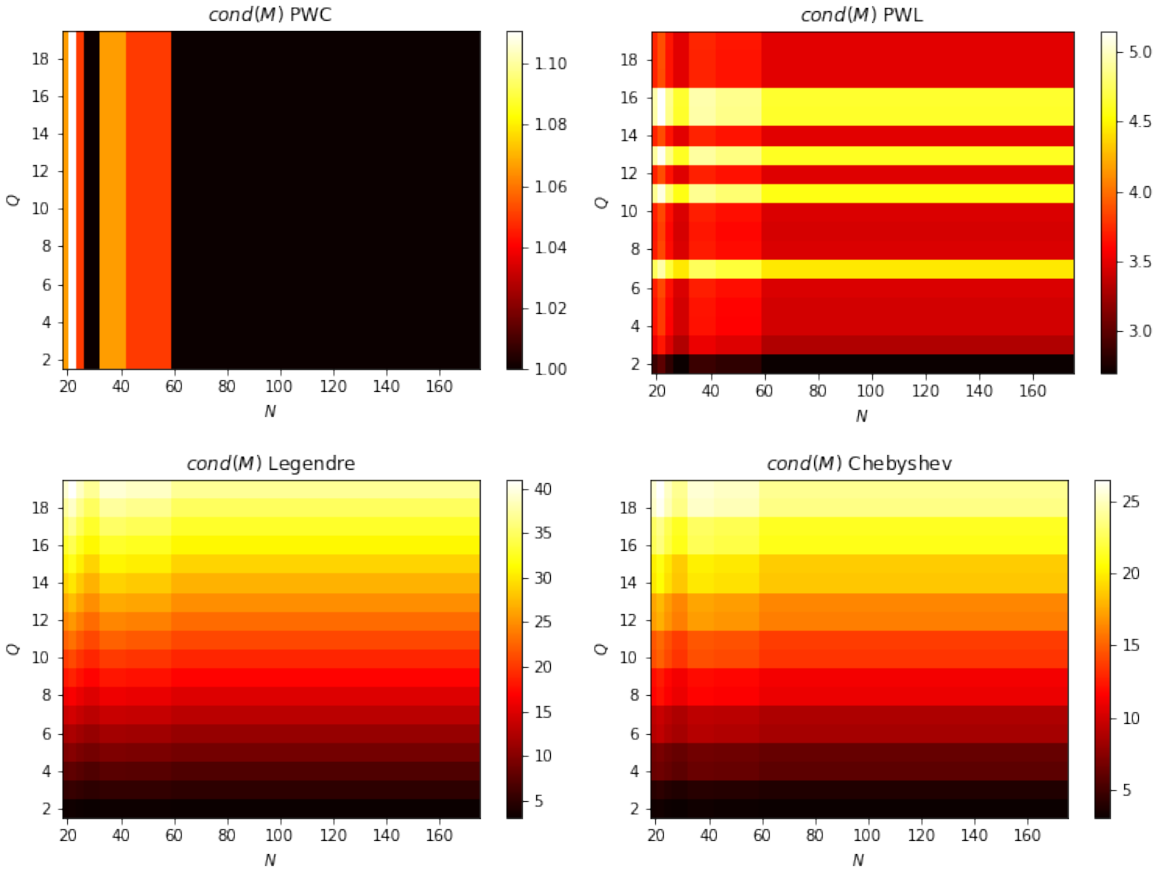

6.3 INTEGRATION ACCURACY

As seen in the previous chapter, the degree of approximation in the solution when using PWC as angular basis is significant when compared to other options. The discontinuous nature of PWC can be thought of a possible cause for this scheme not converging with ISM. The basis functions are smooth over each element on the boundary but the angular kernel is not. This is investigated further in this section. The integrands produced by boundary-to-boundary mapping matrices for PWC and Legendre basis in angle are studied to observe their distribution. We investigate integrands for boundary-to-boundary interaction matrices for two pairs of elements as shown.

Figure 6.6 Pairs of elements for which the boundary-to-boundary mapping integrands are studied

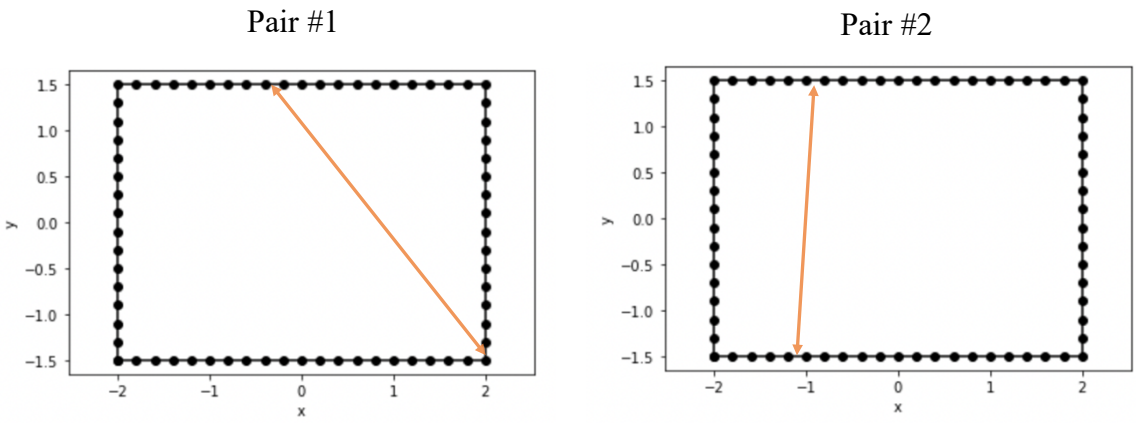

The DOF combinations in which power was mapped between the radiating and receiving elements were obtained and plotted below. These results are produced for $Q = 17$ and a maximum element size of $0.2m$.

Figure 6.7 Boundary to boundary mapping integrands for the first pair of elements in Figure 6.6 with PWC (left column) and Legendre (right column) as angular basis functions

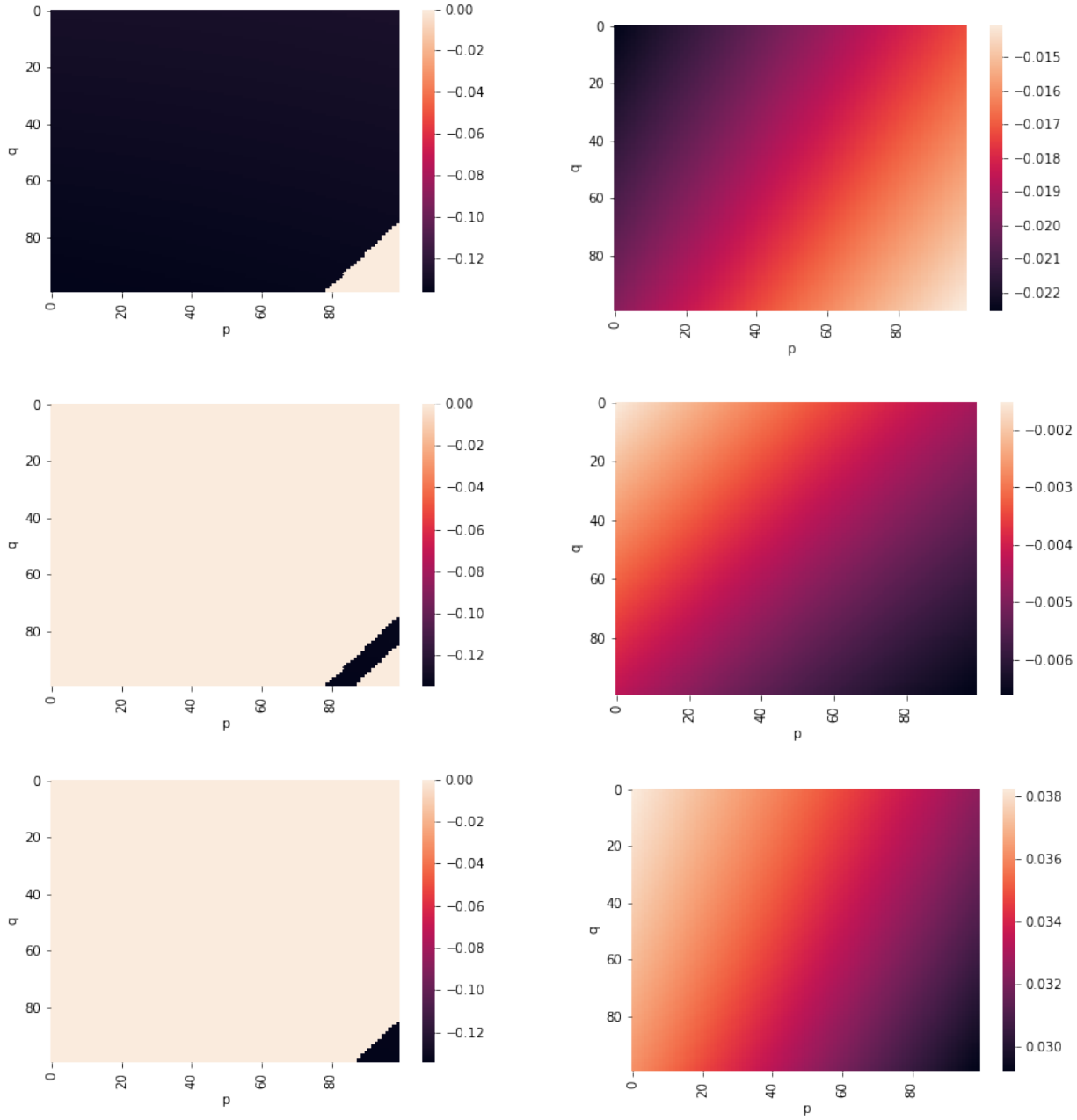

Figure 6.8 Boundary to boundary mapping integrands for the second pair of elements in Figure 6.6 with PWC (top row) and Legendre (bottom row) as angular basis functions

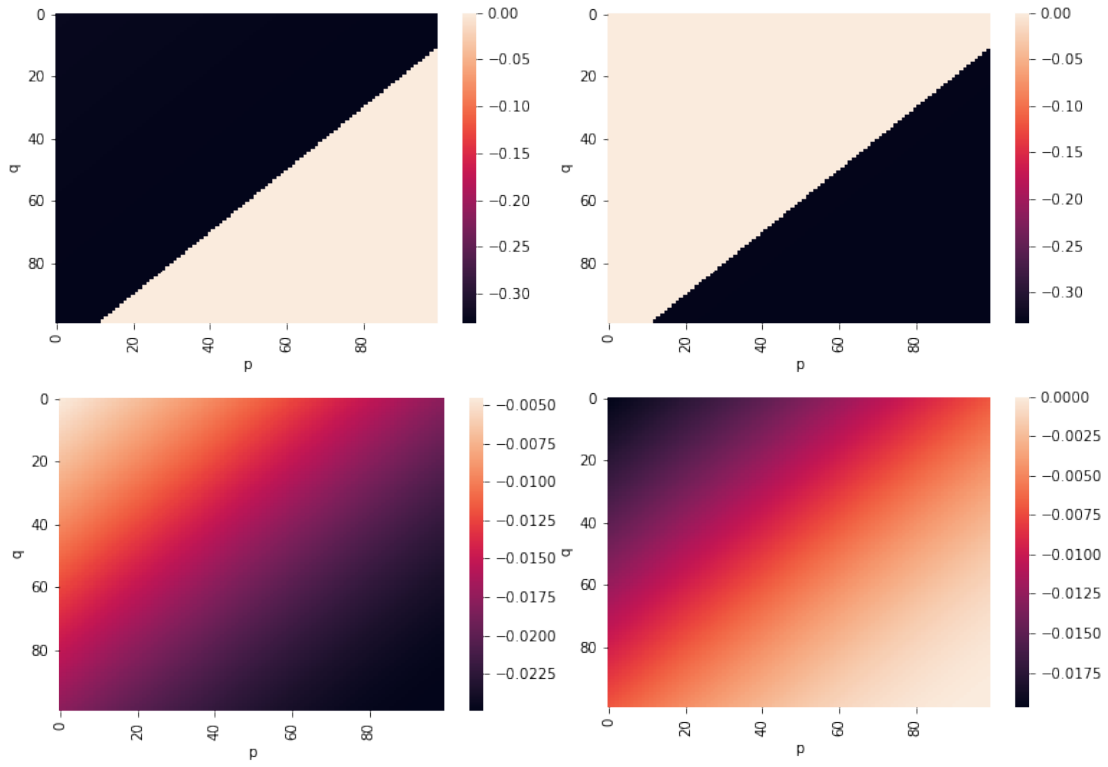

It is evident that the integrands to be evaluated are discontinuous for PWC while the transition is smooth for Legendre. These discontinuities in PWC are difficult to be integrated by Gaussian methods and can attribute to its lack of accuracy. GQ rules can also be affected by the location of the discontinuities in relation to the integration abscissae.

Figure 6.9 Mapping of power in discontinuous bins when using PWC basis in angle for two pairs of elements

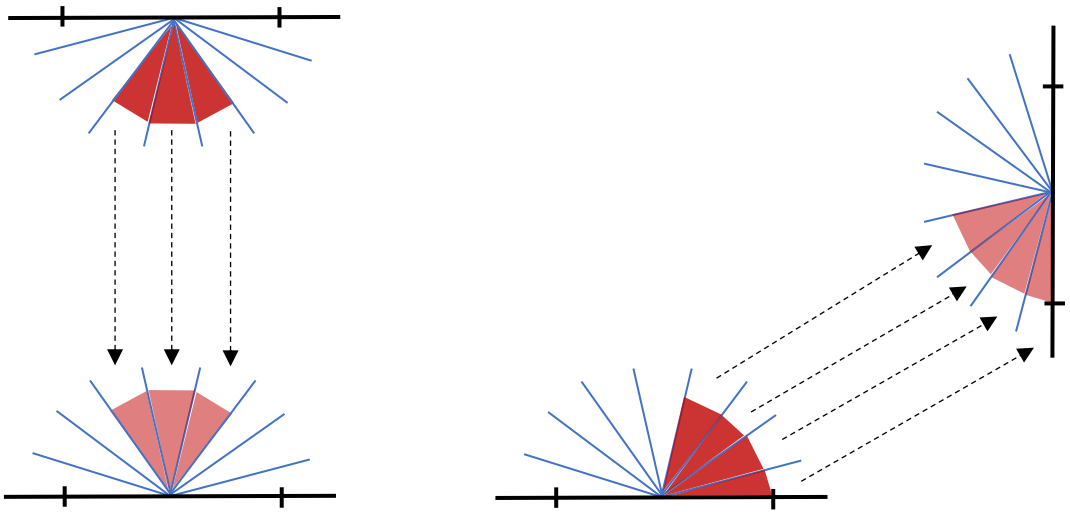

To investigate the integration accuracy further, the normalised error between Monte Carlo and GLQ integration for both pairs of elements in Figure 6.6 is plotted in Figure 6.10. GLQ methods are optimised for a given polynomial of a given order, and Monte Carlo integration will converge for any integrand at sufficiently large number of integration points. Although inefficient for the number of integration points used, the Monte Carlo estimates are guaranteed to converge to the true integral with the general trend of error being inversely proportional to the number of integration points. There is precedent for using this method to evaluate integration accuracy in [54]. A total of 10^6 integration points were used and the results are shown in Figure 6.10. The error plots for PWC and Legendre are seen to reduce with at a large number of integration points used for the Monte Carlo study and show convergence with the GLQ integration results.

Figure 6.10 Normalised RMS error between Monte Carlo and GLQ integration results for (a) first pair and (b) second pair of elements in Figure 6.6.

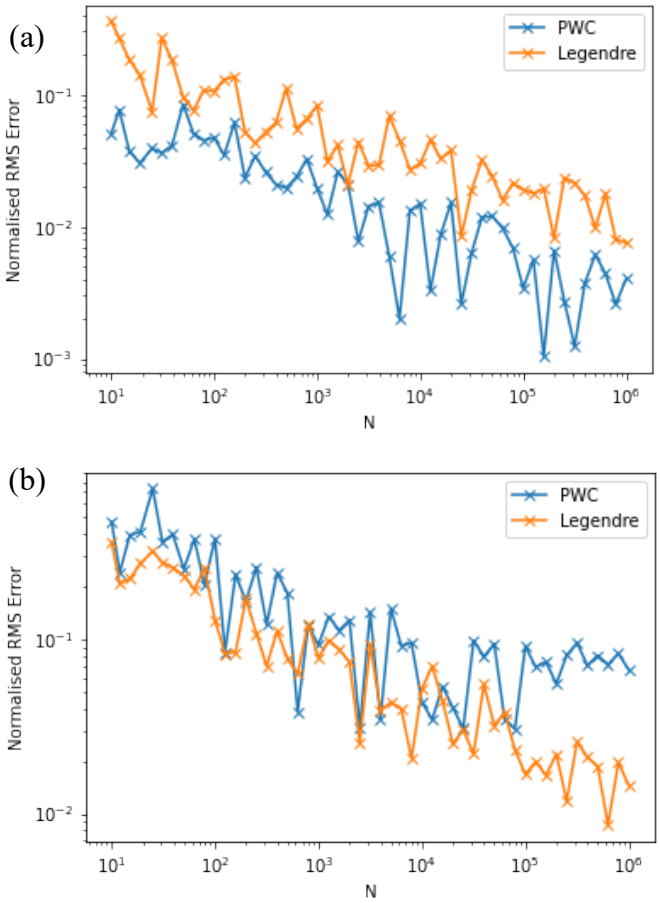

6.4 ALGORITHMIC EFFICIENCY

The computational efficiency of the EBEM algorithm was studied. A crucial part of the algorithm is the mass matrix which is used in all boundary mapping operations. Sparsity of this matrix will affect the computational load and memory requirements. For orthogonal basis in angle such as pairs of PWC or Legendre, the mass matrix is diagonal with NQ non zeros. For PWC discretisation in space and angle, the number of non-zero entries are $l_m \times 2/Q$ where l_m is the length of the m^{th} element. For PWC basis in space and Legendre basis in angle, the number of non-zero entries are $l_m \times 2/(2p+1)$. Higher number of non-zero entries were observed for PWL. Chebyshev polynomials are not orthogonal for the weighing in the discretisation scheme, which yields block diagonal mass matrices with NQ^2 non zero entries.

Another important operator in the algorithm is the boundary-to-boundary mapping matrix which is involved in each reflection. The number of non-zero entries in $\mathbf{T_{bb}}$ for different basis schemes are shown in Figure 6.11:

Figure 6.11 Number of non-zero entries in the boundary-to-boundary mapping matrix for PWC, PWL and Legendre basis

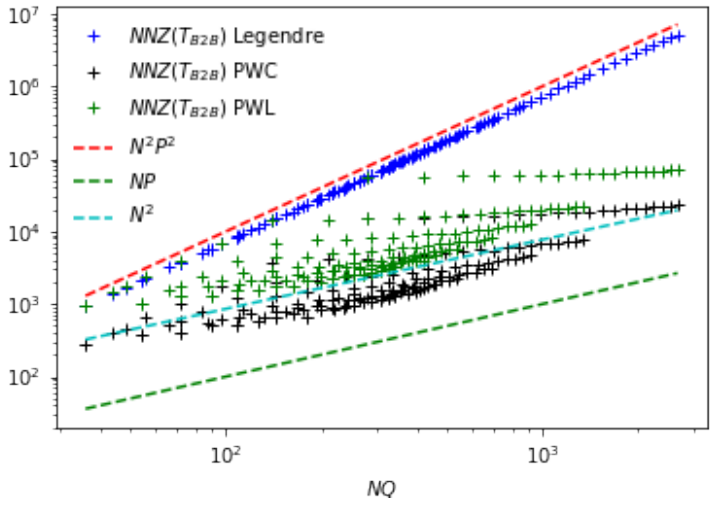

Variation in logarithmic scale of the number of non-zero entries in the boundary to boundary interaction matrix with PWC and PWL basis functions are shown in Figure 6.12:

Figure 6.12 Number of non-zero entries for PWC and PWL boundary to boundary interaction matrices in log scale

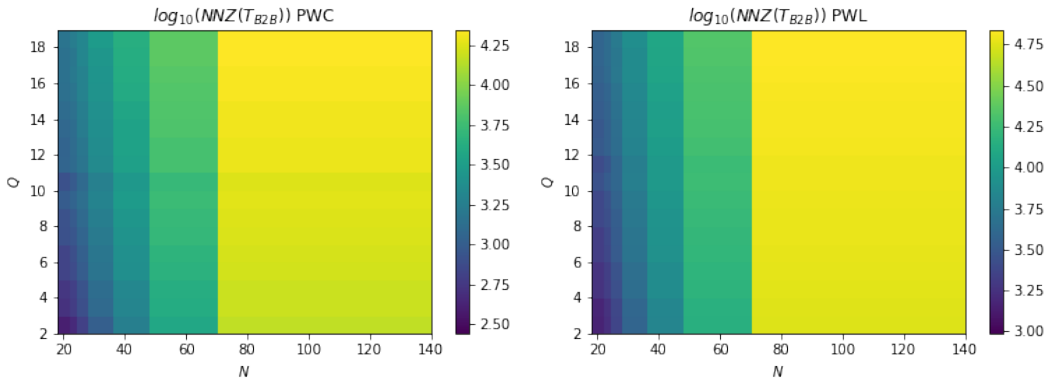

Although the PWC scheme provides advantages for computational efficiency, producing highly sparse solution matrices, its discontinuous nature produces boundary integrals which are discontinuous, and are not very amenable to integration with Gaussian schemes. Although

we have observed that PWC scheme results if highly sparse boundary to boundary interaction matrices and better conditioned mass matrix in comparison to other schemes, it discontinuous nature results in issues as discussed earlier in this chapter, and is not considered an ideal basis choice for such a formulation. Also, the simplicity of PWC functions often allows integrals to be computed analytically, which makes the code more efficient and avoids issues encountered with discontinuities.

7 CONCLUSIONS

A “Surface-based” GA model within a Galerkin BEM framework is presented. The Galerkin BEM framework, notably with the inclusion of the mass matrix expediates comparison between different basis and testing functions. The mathematical form and notation used for EBEM also emphasises synergy with high-frequency BEM, targeted as a step towards a unified mesh-based full-audible-bandwidth algorithm. The formulation also discretises incoming and outgoing energy separately, similar to high frequency BEM. It also implements directional point sources and receivers utilising Fourier series in angle.

The EBEM formulation was validated against ISM for a rectangular room. The results show a high level of agreement with ISM for early reflections when the angular interpolation orders are sufficiently high. The EBEM model was found to converge with the ISM solution at small element sizes and high number of DOFs per element. Identical convergence trends and directional received power were observed for continuous orthogonal polynomials such as Legendre or Chebyshev or Lobatto as angular basis. Other options such as PWL or PWC exhibit a greater degree of approximation, even at high interpolation polynomial orders. Although PWC is beneficial from a computational standpoint with sparse and well conditioned solution matrices, it results in discontinuities in boundary integrands which cannot be accurately evaluated using GQ methods. This is found to be a factor contributing to its poor performance.

From the power distributions on the boundary, it is observed that PWC basis in both space and angle blocks the boundary data into rectangular blocks due its discontinuous nature, while Legendre or Chebyshev or Lobatto as angular basis result in smooth stripes with side lobing in angle. PWL on the other hand are continuous but not smooth over the angular range. Importantly, these polynomials are seen to approximate the peak values accurately. The approximation is seen to be controllable. Smudging of power over a range of reflection angles on the boundary is appropriate for modeling late-time sound fields in room acoustics as individual reflections at this stage are now perceptually distinguishable.

The results demonstrate the Nottingham group's claim that DEA interpolates between low fidelity methods, which is SEA in their work and Radiosity for algorithms such as EBEM and high fidelity methods, like Raytracing or ISM.

7.1 FUTURE WORK

The next steps in development of the EBEM formulation would be to add support for non-convex and 3D geometry with visibility and validity checks. This extension would lead to the need to include corner diffraction to efficiently model sound fields in non-convex geometries. Other spatial basis functions could be utilised, like continuous PWL which would make the solution continuous on the boundary. High-frequency BEM creates radiation that is more 'beam-like' when such smooth spatial basis functions are used. We postulate that this choice will allow the EBEM formulation to model low frequencies as well.

8 REFERENCES

[1] M. Vorländer, Auralization: Fundamentals of Acoustics: Modelling, Simulation, Algorithms and Acoustic Virtual Reality, 2nd ed., Cham, Swizerland: Springer, 2020.

[2] J. A. Hargreaves, “Synergies between the high-frequency Boundary Element Method and Geometric Acoustics,” in *Proceedings of e-Forum Acusticum*, 2020.

[3] S. Siltanen, T. Lokki and L. Savioja, “Rays or waves? Understanding the strengths and weaknesses of computational room acoustics modeling techniques,” in *Proceedings of the International Symposium on Room Acoustics, ISRA*, 2010.

[4] H. Kuttruff, Room acoustics, Crc Press, 2016.

[5] P. T. Calamia, B. E. Markham and U. P. Svensson, “Diffraction culling for virtual-acoustic simulations,” *Acta Acustica united with Acustica,* vol. 94, no. 6, pp. 907-920, 2--8.

[6] T. Cox and P. d'Antonio, Acoustic absorbers and diffusers: theory, design and application, Crc Press, 2016.

[7] L. Savioja and U. P. Svensson, “Overview of geometrical room acoustic modeling techniques,” *The Journal of the Acoustical Society of America,* vol. 138, pp. 708-730, 2015.

[8] H. Kuttruff, “A simple iteration scheme for the computation of decay constants in enclosures with diffusely reflecting boundaries,” *The Journal of the Acoustical Society of America,* vol. 98, no. 1, pp. 288-293, 1995.

[9] E.-M. Nosal, M. Hodgson and I. Ashdown, “Improved algorithms and methods for room sound-field prediction by acoustical radiosity in arbitrary polyhedral rooms,” *The Journal of the Acoustical Society of America,* vol. 116, no. 2, pp. 970-980, 2004.

[10] L. P. Franzoni, D. B. Bliss and J. W. Rouse, “An acoustic boundary element method based on energy and intensity variables for prediction of high-frequency broadband sound fields,” *The Journal of the Acoustical Society of America,* vol. 110, no. 6, pp. 3071-3080, 2001.

[11] J. W. Rouse and L. P. Franzoni, “Improvement of a high-frequency broadband energy-intensity boundary element method to include high resolution specular reflection,” *Journal of Computational Acoustics,* vol. 13, no. 01, pp. 99-125, 2005.

[12] S. Siltanen, T. Lokki, S. Kiminki and L. Savioja, “The room acoustic rendering equation,” *The Journal of the Acoustical Society of America,* vol. 122, no. 3, pp. 1624-1635, 2007.

[13] S. Siltanen, T. Lokki and L. Savioja, “Room acoustics modeling with acoustic radiance transfer,” in *ISRA*, Melbourne, 2010.

[14] G. Tanner, “Dynamical energy analysis—Determining wave energy distributions in vibro-acoustical structures in the high-frequency regime,” *Journal of Sound and Vibration,* vol. 320, no. 4-5, pp. 1023-1038, 2009.

[15] D. J. Chappell and G. Tanner, “Solving the stationary Liouville equation via a boundary element method,” *Journal of Computational Physics,* vol. 234, pp. 487-498, 2013.

[16] D. J. Chappell, Tanner, Gregor and S. Giani, “Boundary element dynamical energy analysis: A versatile method for solving two or three dimensional wave problems in the high frequency limit,” *Journal of Computational Physics,* vol. 231, no. 18, pp. 6181-6191, 2012.

[17] D. J. Chappell, J. J. Crofts, M. Richter and G. Tanner, “A direction preserving discretization for computing phase-space densities,” *SIAM Journal on Scientific Computing,* vol. 43, no. 4, pp. B884-906, 2021.

[18] R. S. Langley, “A wave intensity technique for the analysis of high frequency vibrations,” *Journal of Sound and vibration,* vol. 159, no. 3, pp. 483-502, 1992.

[19] J. A. Hargreaves and Y. W. Lam, “The Wave-Matching Boundary Integral Equation—An energy approach to Galerkin BEM for acoustic wave propagation problems,” *Wave Motion,* vol. 87, pp. 4-36, 2019.

[20] J. A. Hargreaves, L. R. Rendell and Y. W. Lam, “A framework for auralization of boundary element method simulations including source and receiver directivity,” *The Journal of the Acoustical Society of America,* vol. 145, no. 4, pp. 2625-2637, 2019.

[21] J. A. Hargreaves, “A comparison between the high-frequency Boundary Element Method and Surface-Based Geometrical Acoustics,” in *Internosie*, Galsgow, 2022.

[22] J. C. Allred and A. Newhouse, “Applications of the Monte Carlo method to architectural acoustics,” *The Journal of the Acoustical Society of America,* vol. 30, no. 1, pp. 1-3, 1958.

[23] B. S. Atal and M. R. Schroeder, “Study of Sound Decay Using Ray-Tracing Techniques on a Digital Computer,” *The Journal of the Acoustical Society of America,* vol. 41, no. 6, pp. 1598-1598, 1967.

[24] A. Appel, “Some techniques for shading machine renderings of solids,” *Proceedings of the April 30--May 2, 1968, spring joint computer conference,* pp. 37-45, 1968.

[25] A. Krokstad, S. Strom and S. Sørsdal, “Calculating the acoustical room response by the use of a ray tracing technique,” *Journal of Sound and Vibration,* vol. 8, no. 1, pp. 118-125, 1968.

[26] M. Kleiner and B. I. Dalenbäck, “Auralization-an overview,” *Journal of the Audio Engineering Society,* vol. 41, no. 11, pp. 861-875, 1993.

[27] M. R. Schroeder, “Computer models for concert hall acoustics,” *American Journal of Physics,* vol. 41, no. 4, pp. 461-471, 1973.

[28] L. Cremer and A. Müller, “Die wissenschaftlichen grundlagen der raumakustik,” in *Stuttgart: Hirzel*, 1978.

[29] D. Mintzer, “Transient sounds in rooms,” *The Journal of the Acoustical Society of America,* vol. 22, no. 3, pp. 341-352, 1950.

[30] B. M. Gibbs and D. K. Jones, “A simple image method for calculating the distribution of sound pressure levels within an enclosure,” *Acta Acustica united with Acustica,* vol. 26, no. 1, pp. 24-32, 1972.

[31] A. Erraji, J. Stienen and M. Vorländer, “The image edge model,” *Acta Acustica,* no. 5, p. 17, 2021.

[32] R. Heinz, “Entwicklung und Beurteilung von computergestützten Methoden zur binauralen Raumsimulation,” in *Shaker*, 1994.

[33] I. Bork, “A comparison of room simulation software-the 2nd round robin on room acoustical computer simulation,” *Acta Acustica united with Acustica,* vol. 86, no. 6, pp. 943-956, 2000.

[34] C. Schissler, G. Mückl and P. T. Calamia, “Fast diffraction pathfinding for dynamic sound propagation,” *ACM Transactions on Graphics (TOG),* vol. 40, no. 4, pp. 1-13, 2021.

[35] A. Pohl and U. M. Stephenson, “A combination of the sound particle simulation method and the radiosity method,” *Building Acoustics,* vol. 18, no. 1-2, pp. 97-122, 2011.

[36] D. Raudales, D. B. Bliss , J. W. Rouse and L. P. Franzoni, “Benchmark analytical solutions for steady state high frequency broadband sound fields in three rectangular enclosures,” *The Journal of the Acoustical Society of America,* vol. 145, no. 4, pp. 2601-2612, 2019.

[37] B. M. Gibbs and D. K. Jones, “A Simple Image Method for Calculating the Distribution of Sound Pressure Levels within an Enclosure,” *Acta Acustica united with Acustica,* vol. 26, no. 1, pp. 24-32, 1972.

[38] D. Howard and J. Angus, Acoustics and psychoacoustics, Routledge, 2013.

[39] S. Siltanen and T. Lokki, “Diffraction modeling in acoustic radiance transfer method,” *Journal of the Acoustical Society of America,* vol. 123, no. 5, p. 3759, 2008.

[40] S. Siltanen, T. Lokki and L. Savioja, “Frequency domain acoustic radiance transfer for real-time auralization,” *Acta Acustica united with Acustica,* vol. 95, no. 1, pp. 106-117, 2009.

[41] A. Pohl, *Simulation of Diffraction Based on the Uncertainty Relation,* PhD Thesis: Hamburg University, 2013.

[42] J. Bajars, D. J. Chappell, N. Søndergaard and G. Tanner, “Transport of phase space densities through tetrahedral meshes using discrete flow mapping,” *Journal of Computational Physics,* vol. 328, pp. 95-108, 2017.

[43] L. Savioja, “Modeling Techniques for Virtual Acoustics,” in *Ph. D. thesis*, 1999.

[44] T. J. Cox, B. I. Dalenback, P. D'Antonio, J. J. Embrechts, J. Y. Jeon, E. Mommertz and M. Vorländer, “A tutorial on scattering and diffusion coefficients for room acoustic surfaces,” *Acta Acustica united with ACUSTICA,* vol. 92, no. 1, pp. 1-15, 2006.

[45] J. Bajars, D. J. Chappell, N. Søndergaard and G. Tanner, “Computing high-frequency wave energy distributions in two and three dimensions using discrete flow mapping,” in *Proceedings of the 22nd International Congress on Sound and Vibration ICSV22*, Florence, Italy, 2015.

[46] J. A. Hargreaves and T. J. Cox, “A transient boundary element method model of Schroeder diffuser scattering using well mouth impedance,” *The Journal of the Acoustical Society of America,* vol. 124, no. 5, pp. 2942-2951, 2008.

[47] [Online]. Available: https://dlmf.nist.gov/18.3.

[48] A. Lieu, G. Gabard and H. Bériot, “A comparison of high-order polynomial and wave-based methods for Helmholtz problems,” *Journal of Computational Physics,* vol. 321, pp. 105-125, 2016.

[49] J. Rowbottom and D. J. Chappell, “On hybrid convolution quadrature approaches for modeling time-domain wave problems with broadband frequency content.,” *International Journal for Numerical Methods in Engineering,* vol. 122, no. 24, pp. 7581-7608, 2021.

[50] J. A. Hargreaves and Y. W. Lam, “Acoustic cross-energy measures and their applications,” *Proceedings of the international institute of acoustics and vibration,* pp. 1-8, 2015.

[51] T. Betcke, E. van 't Wout and P. Gélat, “Computationally Efficient Boundary Element Methods for High-Frequency Helmholtz Problems in Unbounded Domains,” in *Modern Solvers for Helmholtz Problems*, Birkhäuser, 2017, pp. 215-243.

[52] M. Sato, S. Yoshiyoka, K. Tsukui and R. Yuuki, “Accurate numerical integration of singular kernels in the two-dimensional boundary element method,” in *Boundary elements X*, Berlin, Springer, 1988, pp. 279-296.

[53] J. Bajars and D. J. Chappell, “A boundary integral method for modelling vibroacoustic energy distributions in uncertain built up structures,” *Journal of Computational Physics,* vol. 373, pp. 130-147, 2018.

[54] J. A. Hargreaves, “Time Domain Boundary Element Method for Room Acoustics,” in *PhD Thesis*, University of Salford, 2007.